

# Measurement report: Fourteen months of real-time characterisation of the submicronic aerosol and its atmospheric dynamic at the Marseille-Longchamp supersite

5 Benjamin Chazeau<sup>1,2</sup>, Brice Temime-Roussel<sup>1</sup>, Grégory Gille<sup>2</sup>, Boualem Mesbah<sup>2</sup>, Barbara D'Anna<sup>1</sup>, Henri Wortham<sup>1</sup>, Nicolas Marchand<sup>1</sup>

<sup>1</sup>Aix Marseille Univ, CNRS, LCE, Marseille, France

<sup>2</sup>AtmoSud, Regional Network for Air Quality Monitoring of Provence-Alpes-Côte-d'Azur, Marseille, France

10 *Correspondence to:* Benjamin Chazeau ([benjamin.chazeau@univ-amu.fr](mailto:benjamin.chazeau@univ-amu.fr)) and Nicolas Marchand ([nicolas.marchand@univ-amu.fr](mailto:nicolas.marchand@univ-amu.fr))

**Abstract.** ~~A supersite was recently implemented in Marseille to conduct intensive and advanced measurement studies for ambient aerosols.~~ This study reports results of PM<sub>1</sub> chemical composition determined using a Time-of-Flight Aerosol Chemical Speciation Monitor (ToF-ACSM) over a 14-month period (1 February 2017 - 13 April 2018) at the Marseille-Longchamp supersite (MRS-LCP) in France. Parallel measurements were performed with an Aethalometer, an ultrafine particle monitor and a suite of instruments to monitor regulated pollutants (PM<sub>2.5</sub>, PM<sub>10</sub>, NO<sub>x</sub>, O<sub>3</sub> and SO<sub>2</sub>). The average PM<sub>1</sub> chemical composition over the period was dominated by organic aerosol (OA; 49.7%) and black carbon (BC; 17.1%) while sulfate accounted for 14.6%, nitrate for 10.2%, ammonium for 7.9% and chloride for 0.5% only. Wintertime was found to be the season contributing the most to the annual PM<sub>1</sub> mass concentration (30%), followed by autumn (26%), summer (24%) and spring (20%). During this season, OA and BC concentrations were found to contribute to 32% and 31% of their annual concentrations, respectively, as a combined result of heavy urban traffic, high emissions from residential heating and low planetary boundary layer (PBL) height. Most (75%) of the fifteen days exceeding the target daily PM<sub>2.5</sub> concentration value recommended by the World Health Organization (WHO) occurred during this season. These episodes contribute to an increase of 6.5% of the annual PM<sub>1</sub> concentration. Local and long-range pollution episodes with contrasting chemical composition could be distinguished, accounting for 40 and 60% of the exceedance days, respectively. Enhanced OA and BC concentrations, mostly originating from domestic wood burning under nocturnal land breeze conditions were observed during local pollution episodes, while high level of oxygenated OA and inorganic nitrate were associated to medium/long-range transported particles.

25  
30 In summertime, substantially higher concentrations of sulfate were found with an average and a maximum contribution to the PM<sub>1</sub> mass of 24% and 66% respectively. Results from k-means clustering analysis of daily profiles of sulfate

concentrations clearly reveal the significant influence of local harbour/industrial activities on air quality, in addition to the more regional contribution of shipping traffic that originates from the Mediterranean basin.

35 In summer, sulfate contribution to  $PM_{10}$  increased with an average and a maximum contribution to the  $PM_{10}$  of 24% and 66%. This is partly due to local photochemical production from its precursor  $SO_2$ , locally emitted by shipping and industrial activities and advected to the city under sea breeze conditions. Results from backtrajectory cluster analysis suggest that, besides local anthropogenic activities, Mediterranean long range transport contributes the most to the enrichment of the sulfate fraction. Another important feature of the summer season is that half of the most intense  $SO_2$  peaks happen at that time of the year and are associated to higher UFPs ultrafine particles (UFPs; diameter  $<100nm$ ) number.

40 The fifteen days exceeding the target daily  $PM_{2.5}$  concentration value recommended by the World Health Organization (WHO) occurred during the coldest period (late autumn early spring). These episodes contribute to an increase of 6.5% of the annual  $PM_{10}$  concentration. Local and long range pollution episodes could be distinguished, accounting for 40 and 60% of the exceedance days, respectively. Enhanced OA and BC concentrations, mostly originating from domestic wood burning under nocturnal land breeze conditions were observed during local pollution episodes, while high level of oxygenated OA and inorganic nitrate were associated to medium/long range transported particles.

45 In conclusion this supersite showed a high potential for the study of seasonality and pollution episodes phenomenology in Marseille over multiple geographic scales. The present paper highlights the significant contribution of regional transport of pollutants to the local air pollution that must be considered by local authorities in deploying effective PM abatement strategies.

## 1 Introduction

50 A major societal concern in [European Union \(EU\)](#) countries is related to air quality as it is nowadays recognized as the first sanitary risk from environmental origin. The exposure to fine particles causes premature mortality in European cities according to the report from Environmental European Agency (EEA, 2019). Recent models predict that premature deaths would reach 380000 per year and could even increase up to 500000 by 2050 (Lelieveld et al., 2015). In France, according to a recent study, 48000 premature deaths per year are linked to fine particles, representing the third cause of mortality behind alcohol and tobacco (Pascal et al., 2016). Regarding annual safety threshold recommendations for both  $PM_{10}$  ( $20 \mu g m^{-3}$ ) and  $PM_{2.5}$  ( $10 \mu g m^{-3}$ ) addressed by the World Health Organization (WHO, 2006), most of European countries still exceed the limit values (48 and 68% of air quality monitoring stations, respectively). In Southern France, 85% of the population live in areas exceeding the WHO recommendations for particle matter (Rouaud and Channac, 2019). Even though it is well recognized that smaller particles may cause more damage to human health than  $PM_{10}$  (Kreyling et al., 2006), Air Quality Standard for  $PM_{10}$  has still not been set up in France. Therefore, it appears important to focus on this specific size fraction and extensive studies on high polluted episodes are needed. They are directly linked to several features as chemical composition, physical properties of fine particles, proximity of anthropogenic activities and meteorological conditions. Moreover Pandolfi

et al. (2020) described that long-range sources could affect local urban pollution as more than 60% of PM in five European urban sites were from regional and continental origins.

65 In the last 15 years aerosol mass spectrometer (AMS) technology dedicated to the real-time analysis of the submicron aerosol chemical composition (Canagaratna et al., 2007; Jayne et al., 2000) has been widely used to investigate the emissions and transformation processes of aerosol chemical species. Unfortunately, most of the studies are limited to short-term campaign measurements, hindering our understanding of aerosol chemical composition over long temporal scales. The recently developed Aerodyne aerosol chemical speciation monitor (ACSM) is more robust and easily deployed for long-term  
70 monitoring of submicron aerosol chemical composition (Fröhlich et al., 2013; Ng et al., 2011), even if the ability of measuring particle size distribution is no longer available and the poor resolution of ACSM mass spectra does not allow high-resolution peak fitting (Timonen et al., 2016).

Studies of several month duration using AMS were previously conducted in Europe: Melpitz (3 months; Poulain et al., 2011), Puy-de-Dôme (5 months; Freney et al., 2011) and London (1 year; Young et al., 2015). In recent years ACSM studies  
75 were performed for [yearly trend](#) in remote/regional sites such as Jungfraujoch (14 months; Fröhlich et al., 2015), Montseny (1 year; Minguillón et al., 2015), Ispra (1 year; Bressi et al., 2016) or Aukstaitija in Lithuania (9 months; Pauraite et al., 2019). Similarly [yearly and seasonal](#) investigations were also carried out in large European cities at urban background scale in Paris (2 years; Petit et al., 2015), Zurich (1 year; Canonaco et al., 2015), Helsinki (4 months; Aurela et al., 2015), London (10 months; Reyes-Villegas et al., 2016) and Athens (1 year ; Stavroulas et al., 2019).

80 The Mediterranean city of Marseille, as a highly urbanised area, exposed to a variety of anthropic (traffic, residential heating, shipping, industries) and biogenic (terrestrial vegetation, marine aerosols) sources is a challenging area for fine particle studies. The ESCOMPTE experiment (2001) demonstrated that the topography and the air mass circulation, characterized by local and mesoscale winds, drives the pollution levels in the city (Cachier et al., 2005; Drobinski et al., 2007; Mestayer et al., 2005; Puygrenier et al., 2005). High level of atmospheric pollutants such as fine particles have often been observed in  
85 Marseille, where mortality rate and cardiovascular hospital admissions are significantly elevated, even higher than in Paris whose population is 6 times higher (Pascal et al., 2013).

Fine particles have been previously characterized in Marseille during an intensive field campaign (3 weeks in summer 2008), (El Haddad et al., 2011a, 2011b, 2013). The seasonal variations and sources of aerosol have been well documented through the offline analysis of daily filter samples collected over 1 year (Bozzetti et al., 2017; Salameh et al., 2015, 2018) but this  
90 methodology only gives poor temporal resolution compared to online instruments and therefore cannot capture the fast changes in concentration and chemical composition.

In this context a new atmospheric urban background supersite dedicated to the long-term and real time chemical and physical characterization of submicron aerosol was recently implemented in Marseille. This supersite gathers state of art instruments for the measurement of aerosols (chemical composition and size distribution) and a suite of instruments for the monitoring of  
95 regulated pollutants ( $PM_{2.5}$ ,  $PM_{10}$ ,  $NO_x$ ,  $O_3$  and  $SO_2$ ). The goal of the present paper is to characterize the [fourteen-month](#) phenomenology of submicron aerosol in a coastal city. The seasonal variations, diurnal profiles, and geographical origins of

PM<sub>1</sub> are presented with a focus on local and long-range pollution episodes when PM exceedance days occur. Also, the chemical characteristics of shipping/industrial emissions in summer are explored through backtrajectories analysis.

## 2 Instrumentation and Methodology

### 100 2.1 Marseille Supersite

Marseille-Longchamp supersite (MRS-LCP) is in the downtown park “Longchamp” (43°18'18.84"N; 5°23'40.89"E; 71 m a.s.l.) of Marseille. This site, run by a joint effort between the [Laboratory of Environmental Chemistry \(LCE\)](#) and the French regional air quality network (AtmoSud, <https://www.atmosud.org>), gathers a complete set of instruments for the measurement of both regulated and non-regulated pollutants (see section 2.2). This infrastructure is intended to become a  
105 high-level research platform for monitoring air pollution and contributing to collaborative research programs. It is classified as urban background site based on the criteria used by the European Environment Agency (Larssen et al., 1999). Marseille is the second most populated city in France with more than 1.8 million of inhabitants. [The city also encounters the second most traffic congestion in France \(TOMTOM, 2020\). The number of vehicle kilometres travelled was 2.4 billion within a 5 km radius around the supersite in 2017 \(AtmoSud traffic database\). Considering the relative road network size it was 2.3 times](#)  
110 [higher than the largest city in EU, London \(Department for Transport, 2020\).](#) The city hosts the second largest harbour of the Mediterranean Sea and the [largest](#) French harbour, with almost 4000 ship berthing in the several basins of Marseille for the year 2017 ([based on port calls statistics registered at “Grand Port Maritime de Marseille”](#)). At 40 km North-West of the city is located the large industrial complex of Fos-sur-mer with petroleum refining, shipbuilding, steel facilities, and coke production plants (El Haddad et al., 2011b; Salameh et al., 2018). The region is well-known for active photochemistry  
115 inducing high ozone concentrations (Flaounas et al., 2009) during summer periods, and frequent secondary organic aerosol formation events (El Haddad et al., 2013). Air mass circulation is complex in Marseille area (Drobinski et al., 2007; El Haddad et al., 2013; Flaounas et al., 2009) and is [driven](#) by the surrounding topography. The city is bordered by Mediterranean Sea from the southwest and enclosed from the north, east and south by mountain ranges up to 700 m a.s.l. The synoptic air masses come from the Rhone valley, the Atlantic and Mediterranean Sea (Drobinski et al., 2007).  
120 [Moreover, Marseille air quality is often affected by two regional winds \(Mistral and South-Easterly Mediterranean wind\) and local sea/land breeze cycles. The Mistral is a strong wind blowing from the North-West \(300°-360°\) along the lower Rhône River valley toward the Mediterranean Sea. South-Easterly Mediterranean wind \(105°-135°\) blows at similar intensity from the sea toward the lands. The South-Westerly sea breeze \(210°-270°\) and North-Easterly land breeze \(5°-90°\) are local winds prevailing during weak Mistral wind \(Figure S1\).](#) Land breeze circulation is often associated with high pollution levels  
125 over Marseille due to the low pollutants dispersion ([El Haddad et al., 2013](#)). In the early morning of summer days, Marseille is directly downwind of the industrial area and the harbour basins. As the temperature of the land surface rises, sea breeze sets in and the polluted air masses from the industrial area are transported over the Mediterranean Sea before reaching the city.

Figure 1 shows annual average concentrations for several pollutants ( $\text{NO}_x$ ,  $\text{O}_3$ ,  $\text{SO}_2$ ,  $\text{PM}_{10}$ ,  $\text{PM}_{2.5}$ , BC) measured over the last 11 years at MRS LCP station. The right graphs display the sorted daily concentrations and exceedance days according to WHO recommendations for the years 2017 and 2018. For most of these pollutants the annual concentrations have slowly decreased through the time except for  $\text{O}_3$  in a similar way as observed in Europe (European Environment Agency, 2019). Around 144 days above the 8h average threshold of  $100 \mu\text{g m}^{-3}$  (WHO) were recorded in 2017 and 2018, mostly during summertime. Averaged  $\text{SO}_2$  concentrations display a decreasing trend thanks to EU legislation on emission control and lower fuel sulphur content (limited to 50 ppm in 2005 and then to 10 ppm since 2009). Another explanation could be the decline of maritime transport during several years since the 2009 financial crisis. But from 2013, however,  $\text{SO}_2$  concentrations seem to increase again and could be linked to the enhancement of maritime activity at Marseille harbour. Indeed the French goods maritime transport rose again between 2012 and 2017 (+5.9%), together with the passenger maritime transport that has continuously been enhanced for the past 10 years (+31.7%) (French Commissioner General for Sustainable Development, 2019). For particulate matter ( $\text{PM}_{10}$ ,  $\text{PM}_{2.5}$ ), annual concentrations show very slight decreases in the last 11 years but remain above the WHO recommendations. This is consistent with the global decrease in the EU 28 since 2000 (27 and 28% reduction for  $\text{PM}_{10}$  and  $\text{PM}_{2.5}$ , respectively) and the  $\text{PM}_{2.5}$  target value was exceeded in 21 countries (European Environment Agency, 2019). In the last 2 years about 12 and 28 days with exceedance concentrations were recorded respectively for  $\text{PM}_{10}$  and  $\text{PM}_{2.5}$ , mainly in winter periods.

145

## 2.2 Instrumentation and data analysis

### 2.2.1 ACSM sampling and data corrections

Ambient submicron particles ( $\text{NR-PM}_1$ ) were measured continuously from 1 February 2017 to 13 April 2018 using a time-of-flight aerosol chemical speciation monitor (ToF-ACSM, Aerodyne Research Inc., USA). The instrument provides quantitative assessment of non-refractory species as organics, nitrate, sulfate, ammonium and chloride in the size range 40-1000 nm. The aerosol is sampled at the main inlet at a flow rate of  $3 \text{ L min}^{-1}$  and dried using a Nafion dryer system (Perma Pure, New Jersey, USA) to keep the relative humidity (RH) below 40%. A subsample flow of  $0.085 \text{ L min}^{-1}$  passes through a critical orifice and enters an aerodynamic lens that focuses the particles into a narrow beam, these are then flash-vaporized upon impaction on a heated tungsten plate at  $600^\circ\text{C}$ . The resulting vapours are ionized using 70 eV electron impact (EI) ionization. The time-of-flight mass spectrometer (ETOF, TOFWERK, Thun, Switzerland) provides mass spectra at a mass-to-charge resolution of  $M/\Delta M=600$ . The data were acquired at a time resolution of 15 min using Igor-DAQ v.2.1.4 software and by Tofware v.2.5.13 written in Igor Pro (Wavemetrics inc., Lake Oswego, Oregon, USA). Further description and detail of the instrument are presented by Fröhlich et al. (2013, 2015) and Timonen et al. (2016). Calibrations of ionization efficiency (IE) of nitrate and relative ionization efficiency (RIE) of ammonium and sulfate were repeated 3 times over the 14-month measurement period. The calculated values are summarized in Table S1. Table S2 lists the detection limits,

160

calculated as three times the noise level, for the 5 quantified species. The collection efficiencies values (CE) were corrected using algorithms described by Middlebrook et al. (2012), the composition-dependant CE is shown in Figure S2. On average over the entire period, a composition dependant CE of  $0.47 \pm 0.05$  is obtained, which is comparable to values typically found for ambient aerosol ( $\approx 0.5$ , Middlebrook et al., 2012). An overall uncertainty of  $\pm 30\%$  is associated to the total mass concentrations. It includes the uncertainties on the IE, RIE and CE values (Bahreini et al., 2009).

The organic aerosol (OA) mass was corrected to account for measurement interferences. According to Pieber et al. (2016) ammonium nitrate induces an overestimation of OA at  $m/z$  44. A correction is introduced in the fragmentation table by measuring the relationship between measured  $\text{CO}_2^+$  and the  $\text{NH}_4\text{NO}_3$  mass measured during ToF-ACSM calibrations (see equation S1). Our dataset showed very little contribution of  $\text{NH}_4\text{NO}_3$  on the organic  $m/z$  44 with value ranging from 0.1-0.5% (Table S3).

The ion fragments at  $m/z$  30 and  $m/z$  46 assigned to nitrate ( $\text{NO}^+$  and  $\text{NO}_2^+$ ) may contain interferences from organic species like  $\text{CH}_2\text{O}^+$  at  $m/z$  30 and  $\text{CH}_2\text{O}_2^+$  at  $m/z$  46. These interferences lead to an overestimation of UMR nitrate and can falsely suggest the presence of organic nitrate in high  $\text{OA}/\text{NO}_3^-$  environments. Here the  $m/z$  30 and  $m/z$  46 signals have been corrected for these interferences by using correlated organic signals respectively at  $m/z$  29 from  $\text{CHO}^+$  and  $m/z$  45 from  $\text{CHO}_2^+$  (equation S2), as recommended by Fry et al. (2018). These peaks were the closest organic signals to the nitrate peaks with organic interferences.

### 2.2.2 Collocated instruments

ACSM measurements were combined with several on-line collocated instruments. A dual spot 7-wavelength AE33 Aethalometer (Magee Scientific) (Drinovec et al., 2015) equipped with a  $\text{PM}_{2.5}$  cut-off inlet and a Nafion dryer operating at  $5 \text{ L min}^{-1}$  was used to measure equivalent black carbon (BC) concentrations at a 1 min time resolution. Equivalent black carbon concentrations were calculated from the absorption coefficient at 880 nm with the default mass absorption cross section (MAC) implemented in the AE33 ( $7.77 \text{ m}^2 \text{ g}^{-1}$ ). The submicron aerosol number size distribution was investigated with the model 3031 ultrafine particle monitor (TSI Inc., Minnesota, USA) equipped with a  $\text{PM}_{10}$  cut-off inlet and a Nafion dryer and running at  $16.7 \text{ L min}^{-1}$  for the whole study period. This instrument provides measurements from 20 to 1000 nm, with six channels of size resolution. The aerosol number size distribution in the range 10.25-1084 nm was further explored over 45 channels using a Scanning Mobility Particle Sizer system (SMPS, L-DMA, CPC5403, GRIMM) for two periods: from 23 June to 12 August 2017 (summer period) and from 6 November 2017 to 11 January 2018 (winter period). The SMPS was connected to the ACSM sampling line under the dryer system with a bypass flow rate of  $0.3 \text{ L min}^{-1}$ .

Off-line measurements were carried out to collect particles (24h  $\text{PM}_{10}$ ) onto pre-fired (during 24h at  $500^\circ\text{C}$ ) 150 mm-diameter quartz filters (Pall Gellman, TISSUQUARTZ) (08h00 to 08h00 UTC) using a high volume sampler (Digitel DA-80) operating at a flowrate of  $30 \text{ m}^3 \cdot \text{h}^{-1}$ . 45 filters were discontinuously sampled from 1 March to 1 May 2017 (22 filters) and from 1 July to 23 September 2017 (23 filters). Major anions and cations ( $\text{SO}_4^{2-}$ ,  $\text{NO}_3^-$ , and  $\text{NH}_4^+$ ) were analysed using ion chromatography (Sciare et al., 2008) after extraction of filter punches in ultra-pure water and following recommendations

195 from the EN 16913 European standard. Elemental/organic content was analysed using Sunset OC/EC analyser (EUSAAR2 thermal protocol) according to Cavalli et al. (2010).

Continuous measurements of SO<sub>2</sub>, NO<sub>x</sub> and O<sub>3</sub>, and PM<sub>x</sub> were carried out by the air quality monitoring station. A M100E UV fluorescence analyser, a M200E chemiluminescence analyser (Teledyne API, California, USA) and a Serinus 10 ozone analyser (Ecotech, Australia) were deployed for the SO<sub>2</sub>, NO<sub>x</sub> and O<sub>3</sub> measurements, respectively. A Continuous Beta-attenuation continuous particulate monitor (BAM 1020, Met One Instruments Inc., Oregon, USA) was used to measure the mass concentrations of PM<sub>2.5</sub> and PM<sub>10</sub> and an optical particle counter (FIDAS 200, PALAS, Germany) was used for the measurement of PM<sub>1</sub>, PM<sub>2.5</sub> and PM<sub>10</sub> since February 2018. Each sampler operated with a dedicated sampling line at a flow rate of 16.7 L min<sup>-1</sup> for the BAM 1020 and 5 L min<sup>-1</sup> for the FIDAS. Both instruments were equipped with a drying set-up (smart heater system for the BAM 1020, Intelligent Aerosol Drying System for the FIDAS).

205 The sampling inlets of all the instruments of the station were located at approximately 3 meters above the ground. All the time resolutions of this instrumental panel were synchronized to 15 min and time was UTC based.

### 2.3 Meteorological data and backtrajectories analysis

The site is equipped with a three-dimensional sonic anemometer to provide temperature and wind measurements (directions and speeds). Precipitations and relative humidity parameters were taken from the Vaudrans meteorological station located 6 km away for the MRS-LC site (43°18'26"N; 5°28'28"E). Non-parametric wind regression (NWR; Henry et al., 2009) and sustained wind incidence method-2 (SWIM-2; Olson et al., 2012) algorithms were used to examine the geographical origin of pollutants. NWR and SWIM-2 analyses were performed using the ZeFir toolkit (Petit et al., 2017a). SWIM-2 analysis can be preferred over standard NWR analysis in specific cases when rapid changes of wind direction occur, as it includes a down-weighting function related to the standard deviation of the wind direction (Petit et al., 2017a). To investigate air mass origin during specific pollution episodes, 72h-backtrajectories were calculated every hour from the PC-based version of HYSPLIT (Draxler et al., 1999) with weekly 1° Global Data Assimilation System (GDAS) meteorological field data. Backtrajectories were set to end at MRS-LCP coordinates (43°18'18.84"N; 5°23'40.89"E ; 64 m a.g.l.). Planetary Boundary Layer (PBL) height data were directly extracted from the GDAS files with HYSPLIT. ~~Cluster analyses were then applied on the calculated backtrajectories for the summer 2017 period.~~ Finally, Concentration Weighted Trajectory (CWT) was performed with ZeFir to investigate the locations most frequently associated with elevated concentrations. CWT approach relates pollutant concentrations measured at a receptor site (MRS-LCP) with backtrajectories, and displays the localisation of air masses associated with high concentrations at the site (Ashbaugh et al., 1985; Petit et al., 2017b). For this study, the CWT domain was set in the range of (40-46° N; -5-10° E) with the grid cell size of 0.05°×0.05°.

### 3 Results and discussion

#### 3.1 Air quality overview

225 Figure 1 shows the annual average concentrations of regulated pollutants ( $\text{NO}_2$ ,  $\text{O}_3$ ,  $\text{SO}_2$ ,  $\text{PM}_{10}$ ,  $\text{PM}_{2.5}$ ) measured over 11  
years (2008-2018) at MRS-LCP station and the corresponding number of days exceeding the daily WHO guidelines during  
the period of the present study (2017-2018). Based on the Theil-Sen approach, the annual concentrations of  $\text{NO}_2$ ,  $\text{PM}_{10}$  and  
 $\text{PM}_{2.5}$  have decreased at a yearly rate of -0.58, -0.40, and -0.57  $\mu\text{g m}^{-3}$ , since 2010, in a comparable way as observed in urban  
sites within Europe (EEA, 2020). These trends can be related to the parallel reduction in air pollutant emissions resulting  
230 from the EU policies that have been continuously implemented.

Despite these significant progresses towards better air quality, the city is still experiencing days with exceedance  
concentrations for  $\text{PM}_{10}$  and  $\text{PM}_{2.5}$ , mainly in winter periods (Figure 1). In the period 2017 to 2018, about 28 and 12  
exceedance days were recorded for  $\text{PM}_{2.5}$  and  $\text{PM}_{10}$  respectively.

Moreover, as a coastal city in the Mediterranean basin, Marseille exhibits high ozone concentrations, especially during  
235 summertime. The annual mean concentration of ozone measured at MRS-LCP station has reached 60  $\mu\text{g m}^{-3}$  in 2018, and  
144 days above the 8h-average threshold of 100  $\mu\text{g m}^{-3}$  (WHO) were recorded in 2017 and 2018, mostly during summertime  
when temperature are the highest. The annual mean increases at a yearly rate of + 0.84  $\mu\text{g m}^{-3} \text{ year}^{-1}$ , which is consistent  
with the general trend observed in cities in Europe. Part of this increase is believed to reflect the reduction of the NO emitted  
locally and its resulting lower NO titration effect in urban environment (Escudero et al., 2014).

240 Another feature of the city shown in Figure 1 is that the decreasing trend observed from most primary pollutants does not  
apply to  $\text{SO}_2$ , as the annual average concentrations have increased again since 2014. It is believed that the trend toward lower  
concentration expected from the use of low fuel sulphur content has been hindered by the increasing influence of in-port ship  
emissions and the spreading of cruise tourism in the city (+31% of cruise passengers in the period 2014-2018 ; MedCruise,  
2018). As a result,  $\text{SO}_2$  constitutes a potential source of secondary particulate matter produced locally.

245

#### 3.2 Cross-validation of $\text{PM}_{10}$ chemical species concentrations

The  $\text{PM}_{10}$  mass concentrations measured by the ToF-ACSM were compared with 24h- $\text{PM}_{10}$  filter measurements and  
displayed in the Figure S3. The concentrations of chemical species were daily averaged and compared with respective offline  
measurements from 1 March to 23 September 2017 (n= 45). Orthogonal distance regressions were performed for the analysis  
250 and the term “a” and “b” referred to the intercept and the slope, respectively. A good agreement is found for ammonium and  
sulfate ( $R^2=0.71$  and slope of 1.0, and  $R^2=0.76$  and slope of 1.03, respectively). For nitrate the results are less consistent  
( $R^2=0.69$  and slope of 1.59). This higher slope can be attributed to the volatilization of nitrate from the filters during hot  
periods (Ripoll et al., 2015; Schaap et al., 2004a). The  $\text{NH}_4 \text{ measured} / \text{NH}_4 \text{ predicted}$  ratio was also investigated from 1 February  
2017 to 13 April 2018 (Figure S4) as an indirect proxy for particle acidity (Zhang et al., 2007) and/or presence of high

255 organic nitrate concentrations (Petit et al., 2017b). The  $\text{NH}_4$  predicted represents the theoretical ammonium concentration  
needed to neutralize the inorganic species concentrations ( $\text{NO}_3^-$ ,  $\text{SO}_4^{2-}$ ,  $\text{Cl}^-$ ). For most of the cities inorganic species tend to  
be fully neutralized and a limited amount of acidic particles can only be observed when the site is located close to an  
emission source (e.g. industries, harbour, fire event...). Here the slope value close to 1 (0.95) reflects a full neutralization for  
all anions and suggests that there is enough ammonia in the gas phase to neutralize these species despite the nearby harbour  
260 and industrial complex. In addition to agricultural activity, ammonia can be emitted by sources closed to urban areas, such as  
vehicular exhausts, sewage, industrial emissions or residential biomass burning (Meng et al., 2017; Sun et al., 2017; Sutton  
et al., 2013).

The organics to OC comparison (ACSM concentrations vs filters) showed a good correlation with  $R^2=0.79$  whereas the  
intercept value was low (-1.23) and the slope was high (2.37) (Figure S3). The slope, interpreted as the OM to OC ratio, is  
265 higher than the recommended values for urban areas ( $1.6\pm 0.2$ , Petit et al., 2015; Stavroulas et al., 2019; Turpin and Lim,  
2001). It is possible that the chosen sampling periods for the comparison (spring and summer 2017) bias high the OM-to-OC  
value as the photochemical activity and thus atmospheric aging are expected to increase. Ratio up to 2.2 have been observed  
when a significant fraction of particulate matter is made of aged aerosol (Aiken et al., 2008; Minguillón et al., 2011).  
Minguillón et al. (2015) and (Via et al., 2020) also suggest a possible overestimation of OA due to the underestimation of the  
270 RIE applied to organics with the ACSM. RIE for organic varies within a wide range which strongly depends on the carbon  
oxidation state (Xu et al., 2018) and thus would need further investigations. A theoretical OM to OC ratio can be calculated  
based on fractional contribution of m/z 44 (f44) mainly due to  $\text{CO}_2^+$  (Canagaratna et al., 2015). The determined ratio was  
1.94 over the offline measurements period, which is lower than the ratio obtained from OC filters comparison method but  
remains elevated for an urban site. From this method, a value of 1.91 was found for the entire study period.

275 BC measurements from AE33 are compared with EC offline filters and an excellent agreement is found with  $R^2=0.87$ . The  
slope of 1.68 relates the difference in measurements properties between EC (thermic) and BC (absorption). The difference  
between the measured BC and EC could be attributed to the variability of the mass absorption coefficient (MAC) value used  
to convert the absorbance to BC mass concentrations in the AE33 instrument. This value could be influenced by light-  
absorbing OC like brown carbon from biomass burning. Here the slope is in agreement with values from other studies: 1.14  
280 to 2.13 through one year at Fresno supersite (Park et al., 2006; 1.62 and 1.92 using EUSAAR2 and NIOSH870 protocols,  
respectively) and between January 2015 and July 2016 at the Environment-Climat Observatory of Lecce (Merico et al.,  
2019).

Finally the sum of ACSM species and BC mass concentrations were compared to the estimated mass using SMPS volume  
during the two deployment periods of this instrument (from 23 June to 12 August 2017 and from 6 November 2017 to 11  
285 January 2018). For the SMPS mass conversion, a density ( $d_{\text{calc}}$ ) was estimated taking into account the chemical composition  
of  $\text{PM}_{10}$  with respective densities of  $1.75 \text{ g cm}^{-3}$  for nitrate, sulfate and ammonium and  $1.52 \text{ g cm}^{-3}$  for chloride (Cross et al.,  
2007). The organic aerosol density can increase whether there are high contributions of carboxylic/dicarboxylic acids  
( $1.46\pm 0.23 \text{ g cm}^{-3}$ ) and/or polycyclic aromatic hydrocarbons ( $1.28\pm 0.12 \text{ g cm}^{-3}$ ). In contrast this density would decrease with

high contributions of n-alkanes ( $0.79 \pm 0.01 \text{ g cm}^{-3}$ ) and/or n-alkanoic acids ( $0.89 \pm 0.07 \text{ g cm}^{-3}$ ) (Turpin and Lim, 2001).  
290 Finally, a density of  $1.2 \text{ g cm}^{-3}$  was chosen for organic aerosol (Cross et al., 2007). A default density of  $1.77 \text{ g cm}^{-3}$  is applied  
for BC as recommended by Poulain et al. (2014). The calculated density is based on the following equation (Salcedo et al.,  
2006):

$$d_{calc} = \frac{[Total_{ACSM} + BC]}{\frac{[NO_3^-] + [SO_4^{2-}] + [NH_4^+]}{1.75} + \frac{[Cl^-]}{1.52} + \frac{[OM]}{1.2} + \frac{[BC]}{1.77}}, \quad (1)$$

295

where the time-dependant mass fractions are based on ACSM and AE33 measurements. The density was found to range  
between 1.24 and 1.77, with an average value of 1.43. The scatter plot of ACSM+BC concentrations vs.  $PM_{10}$  concentrations  
from SMPS in Figure 2a shows strong correlation ( $R^2=0.81$ ) and slope close to unity (slope=1.02 and intercept=0.46).  
Reconstituted mass (ACSM+AE33) was also compared to  $PM_{10}$  mass measurements from FIDAS for the last 3 months of the  
300 database (19 February to 13 April 2018) in Figure S3. Again satisfactory results are displayed with  $R^2=0.89$ , slope=0.9 and  
intercept=1.67 and show the consistency of the different measurements. The linear regression analysis of reconstituted  $PM_{10}$   
vs  $PM_{2.5}$  yielded a slope of 0.89 for a confidence interval of 99% and  $R^2=0.77$  (Figure 2b) so we can assume that  $PM_{2.5}$   
concentrations are mainly composed of submicron particles.

### 3.3 Submicron aerosol temporal variability

#### 305 3.3.1 PM average composition

Figure 3 shows the time series of the concentrations of ACSM components, Black Carbon, daily- $PM_{2.5}$  and ultrafine particles  
(UFPs; diameter <100nm) number along with the seasonal  $PM_{10}$  chemical composition. The average concentration over the  
period was  $9.9 \mu\text{g m}^{-3}$  and  $12.0 \mu\text{g m}^{-3}$  for  $PM_{10}$  (ACSM+BC) and  $PM_{2.5}$  (BAM), respectively. While these results comply  
with the EU  $PM_{2.5}$  annual mean standard of  $25 \mu\text{g m}^{-3}$ , the value does not meet the WHO guideline of  $10 \mu\text{g m}^{-3}$ , like most of  
310 the cities in Europe (EEA, 2019). The site experienced several episodes of elevated  $PM_{10}$  ( $> 30 \mu\text{g m}^{-3}$ ), most frequently  
during the coldest months in late autumn, winter and early spring, resulting occasionally in an exceedance of daily  $PM_{2.5}$   
limit WHO values.

The  $PM_{10}$  chemical composition is dominated by organics (49.7%) and BC (17.1%), while sulfate accounts for 14.6%, nitrate  
for 10.2%, ammonium for 7.9% and chloride for 0.5% only. The  $PM_{10}$  chemical composition is consistent with results from  
315  $PM_{2.5}$  filters in MRS-LCP reported over the August 2011 to July 2012 period (Bozzetti et al., 2017; Salameh et al., 2015).  
The results are also comparable to those found in other Mediterranean coastal cities, where a noticeable proportion of sulfate  
is generally observed (Mallet et al., 2019; Minguillón et al., 2015; Stavroulas et al., 2019), whereas most urban sites in  
northern/central Europe show higher nitrate contribution (Lianou et al., 2011; Petit et al., 2015; Young et al., 2015).

The UFP average concentration as determined by the UFP monitor was less than  $8000 \text{ cm}^{-3}$  in the range of 20-100 nm. These  
320 values are similar to those observed in Barcelona but are higher than those found in Madrid and Rome for the same size

range (Brines et al., 2015). In Marseille, UFPs represented at 85% of total submicron particle number, in agreement with previous observations in urban environment (Rodríguez and Cuevas, 2007; Wehner and Wiedensohler, 2003).

### 3.3.2 Seasonal variability

325 A summary of the seasonal statistics (average and standard deviation) relative to  $PM_{10}$  mass, chemical composition and number concentrations is reported in Table 1.  $PM_{10}$  concentrations estimated from the sum of all species measured by the ACSM + Black carbon vary between  $8.1 \mu\text{g m}^{-3}$  (spring) and  $11.9 \mu\text{g m}^{-3}$  in winter.

The concentrations of organic and black carbon follow this trend as the highest values are observed during winter and autumn with OA / BC concentrations of  $6.2 / 2.1 \mu\text{g m}^{-3}$  and  $5.1 / 1.9 \mu\text{g m}^{-3}$  respectively. The higher carbonaceous concentrations during the cold months are expected considering i) a reduction of the planetary boundary layer (PBL) height  
330 resulting in the accumulation of pollutants at ground level compared to other seasons and ii) increasing emissions from residential heating and open combustion of green wastes (Bozzetti et al., 2017).

The relative contribution of the biomass burning throughout the seasons can be estimated using the aethalometer model (Sandradewi et al., 2008) that allows to apportion black carbon into fossil fuel and wood burning (respectively  $BC_{FF}$  and  $BC_{WB}$ ). The methodology applied is further described in the Supplement. Seasonal estimations of  $BC_{WB}$  and  $BC_{FF}$   
335 contributions in MRS-LCP are shown in Figure 4.  $BC_{WB}$  shows a clear seasonal variability with a mean value of  $0.59 \mu\text{g m}^{-3}$  corresponding to the highest contribution to the total BC in winter (28%). By comparison, summer average value of  $0.11 \mu\text{g m}^{-3}$   $BC_{WB}$  represents the lowest contribution (7%). Overall, the magnitude of the seasonal variations are similar to those reported recently in Athens and Milan (Diapouli et al., 2017; Liakakou et al., 2020; Mousavi et al., 2019). Biomass burning also contributes to the seasonal variability of organic aerosol concentration as shown by the magnitude between winter and  
340 summer of f60 (the relative signal intensity of m/z 60, commonly attributed to  $C_2H_4O_2^+$ , a characteristic fragment ion of biomass-burning tracer anhydrosugars ; Alfarra et al., 2007) (Table 1). Despite the mild climate in South of France, wood heating is an important source of pollution. Almost 15% of housing use wood for heating in Aix-Marseille Metropolis (use of chimneys, wood stove or wood boiler) (ADEME, 2009) and around 50% of the identified equipment are still considered as non-efficient in France (ADEME, 2020). Additionally, several wood-fired heating plants located in Aubagne, Gardanne  
345 and Aix-en-Provence (15, 18 and 25 km from Marseille, respectively) might contribute to biomass burning emissions. Besides wood heating, the open burning is expected to contribute to the increasing concentration of carbonaceous aerosol, particularly in autumn. This includes the agricultural burning, since one third of the department surface area is dedicated to agricultural activities, but also the green waste burning. While this latter practice is prohibited, it is suspected to still be used nowadays. The close link between the temperature and the magnitude of the wood burning contribution suggests that the  
350 residential heating is the main source of biomass burning carbonaceous aerosol (Figure S7a).

The  $BC_{FF}$  is nevertheless the main contributor to ambient black carbon (72-93% of total BC) but has a much lower seasonal fluctuation than biomass burning, with values ranging from  $1.1 \mu\text{g m}^{-3}$  (spring) to  $1.7 \mu\text{g m}^{-3}$  (autumn). The elevated  $BC_{FF}$  contribution and lower seasonal variations are consistent with the high traffic emissions that remain constant in the city

throughout the year. A similar low seasonal amplitude is observed on f57, the fraction of the  $C_4H_9^+$  organic fragment, commonly considered as a proxy for primary organic aerosol and emitted mostly by traffic emissions (Zhang et al., 2005). Vehicular emissions highly contribute to carbonaceous aerosols in Marseille as demonstrated by El Haddad et al. (2011b) and can be a significant source for OA.

The secondary organic aerosol is known to substantially contribute to the OA in Marseille (Bozzetti et al., 2017; El Haddad et al., 2013). The contribution of this fraction to the total OA seems to remain relatively constant during the year, as suggested by the variation of  $f_{44}$  (the relative signal intensity of  $m/z$  44, commonly attributed to  $CO_2^+$ , a characteristic fragment ion of oxygenated organic aerosol) across the seasons (Table 1). It is worth noting the clear correlation between  $f_{44}$  and the temperature in summer, as shown in (Figure S7b). This observation supports the conclusion that biogenic precursors strongly contribute to the secondary organic aerosol formation at this season.

Sulfate concentrations exhibit opposite seasonal pattern to that observed for the total carbonaceous fraction, as the highest concentration is observed in summer ( $2.26 \mu\text{g m}^{-3}$ ). During this season, the average contribution of sulfate to the total mass of  $PM_{10}$  accounts for  $\approx 23$  % of the  $PM_{10}$ . Sulfate exhibits its lowest concentrations in spring and winter ( $1.06$  and  $1.12 \mu\text{g m}^{-3}$  respectively). The origin of sulfate aerosol is further examined in section 3.4.2.

Nitrate shows a distinct seasonal pattern as maximum concentrations occur in winter and early spring, with average values of  $1.58$  and  $1.13 \mu\text{g m}^{-3}$  respectively, making up  $\approx 14.0$  % of the particle mass, and minimum concentration in summer ( $0.24 \mu\text{g m}^{-3}$ ). This feature has been already observed in other European cities (Minguillón et al., 2015; Petit et al., 2015; Reyes-Villegas et al., 2016; Young et al., 2015) and is generally attributed to the lower temperature and higher relative humidity that shift the partitioning of semi-volatile ammonium nitrate toward the particulate phase (Huffman et al., 2009; Stelson and Seinfeld, 1982). This is supported by Figure S8 where lowest temperature and highest relative humidity values are found in winter and early spring. The episodes with high nitrate concentration reported in late winter/early spring (see section 3.3.1) are also expected to bias high the average for these seasons though. Nitrate was further categorised into inorganic and organic fraction using the method described by Farmer et al., (2010). The detailed methodology is presented in the Supplement. Inorganic nitrate makes up a large fraction (62-80%) of the total nitrate as shown in Figure 4 and explains most of its variability throughout the seasons.  $NO_{3,org}$  average concentration ranges from  $0.09 \mu\text{g m}^{-3}$  in summer to  $0.26 \mu\text{g m}^{-3}$  in winter. The resulting average  $NO_{3,org}$  fraction for the whole dataset is  $20 \pm 7\%$ . The error here is determined from error propagation calculations described by Farmer et al. (2010) and is detailed in SI. This fraction is in the range of reported values for European urban sites (28%, Mohr et al., 2012; 24%, Saarikoski et al., 2012). Assuming a molecular weight between  $200$  and  $300 \text{ g mol}^{-1}$  for particle organic nitrates, contribution of organic nitrates to total OA can be estimated (Xu et al., 2015). Results presented in Table S4 give a contribution to total OA of about 6–10% in summer, 11-17% in autumn, 14-20% in winter and 18–28% in spring. These results suggest that despite the low contribution of  $NO_{3,org}$  to total nitrate, organic nitrates can be an significant fraction of OA in Marseille.

As ammonium is closely connected to sulfate and inorganic nitrate and, the combination of both components with opposite trends induces a rather flat seasonal pattern.

Chloride maximum and minimum concentrations occur in winter and summer, respectively. This is consistent with the expected dominant form of chloride usually detected in PM<sub>1</sub> with ACSM, that is semi-volatile NH<sub>4</sub>Cl.

390

The seasonal variation of UFPs followed the general patterns observed for BC and OA concentrations over the year (Figure S8). UFPs average concentration were slightly higher in winter and autumn with average values of 8600 cm<sup>-3</sup> and 8100 cm<sup>-3</sup>, respectively, while an average value of 7500 cm<sup>-3</sup> was found in spring and summer.

395

To get insights into the sources and processes contributing to ultrafine particles in urban ambient air, number concentrations were investigated using the methodology developed by Rodríguez and Cuevas (2007). This methodology has been extensively applied in urban environment to apportion the number concentration of primary and secondary sources (del Águila et al., 2018; González et al., 2011; Hama et al., 2017a, 2017b; Reche et al., 2011; Rodríguez and Cuevas, 2007; Tobías et al., 2018). The total measured UFPs number concentration (N) can be split in two components:

400

$$N_1 = S_1 \cdot BC, \quad (2)$$

$$N_2 = N - N_1, \quad (3)$$

405

where N<sub>1</sub> accounts for fresh primary emissions of vehicle exhaust, directly emitted in the particle phase or nucleating immediately after emission (Arnold et al., 2006; Burtscher, 2005; Kittelson, 1998) and N<sub>2</sub> accounts mostly for secondary particles formed in the atmosphere during the dilution and cooling of the exhaust emissions (see Figure S11 for details). To refine the method, BC<sub>FF</sub> was used instead of total BC to better apportion primary traffic emissions.

410

The N<sub>1</sub> and N<sub>2</sub> fractions were derived from the TSI 3031 measurements and average number concentrations during each season are reported in Table 1 and Figure 4. It should be emphasized that results obtained from this analysis are sensitive to the sampling strategy (cut size of the particle counter, distance from the sources) and to the physicochemical properties of the primary particles (presence and size of the BC core) (Kerminen et al., 2018; Kulmala et al., 2016). In the present work, an underestimation of N<sub>2</sub> is expected, as particles smaller than 20 nm are not accounted for when the TSI 3031 is used.

415

The N<sub>2</sub> fraction was predominant with number concentrations 1.02 to 1.7 times higher than N<sub>1</sub>. The N<sub>2</sub> average particle numbers were higher in spring and summer as the concentrations reached their highest value (≈ 4300 cm<sup>-3</sup> and 4800 cm<sup>-3</sup>). In contrast, the N<sub>1</sub> emissions appear to be dominant in winter and autumn, with average concentrations of ≈ 4200 and 3800 cm<sup>-3</sup>. An explanation for these results could be either the higher traffic rate or the low temperature influencing the soot particle formation during combustion in these seasons. The N<sub>1</sub> seasonal trend slightly varied through the measurement period with a contribution between 37 and 50%.

420

While it appears that the highest UFPs mean number concentrations are observed in autumn and winter, a different picture is found when the frequency of occurrence of short term high concentration episodes is investigated as a function of the season. Figure 5 shows the box plots of 15-minute average UFPs number concentrations, binned into intervals of SO<sub>2</sub> concentrations

classes, a proxy industrial and shipping activity. It clearly shows that the most intense episodes occur preferentially in summer and are associated with high SO<sub>2</sub> concentrations. This season gathers more than 55% of the highest SO<sub>2</sub> concentrations (>20µg m<sup>-3</sup>) episodes. The higher occurrence of sharp and intense UFP peaks in summer is confirmed by the SMPS data as 10 events exceeding 50 000 cm<sup>-3</sup> were observed in summer against only 1 in winter (Figure 3).

### 3.3.3 Diurnal profiles

Figure 6 shows the average diurnal profiles of ACSM components (OA, NH<sub>4</sub><sup>+</sup>, NO<sub>3</sub><sup>-</sup>, SO<sub>4</sub><sup>2-</sup>) and specific organic markers (f<sub>44</sub>, f<sub>57</sub>, f<sub>60</sub>), BC<sub>FF</sub>, BC<sub>WB</sub> and particle number concentrations (N<sub>1</sub> and N<sub>2</sub>) across the different seasons.

Distinctive diurnal patterns are found for carbonaceous aerosols. First, a clear traffic-related diurnal profile was observed for BC<sub>FF</sub> with a morning peak and an evening peak starting at the typical rush hours (04:00 UTC and 16:00 UTC respectively). This pattern confirms that traffic emission prevails over the other potential sources of fossil fuel such as oil-fired boilers, industrial and shipping activities. The amplitude of the traffic-related diurnal cycle seemed to be affected by the boundary layer height since it varied within the year, with maximum min to max amplitude of 0.9 during winter and minimum min to max amplitude of 0.5 during summer.

The BC<sub>WB</sub> had a distinct diurnal cycle with a typical increase starting at 17:00 UTC and a maximum level of 1.1 µg m<sup>-3</sup> at nighttime. The mean to max amplitude increased steadily from spring, autumn to winter (0.1, 0.2 and 0.4, respectively), following the increased heating demand. Under specific meteorological conditions (no rain, low wind speed, low boundary layer height) this source is responsible for episodes of high PM<sub>1</sub> concentrations in Marseille. This is discussed in detail in Sect. 3.4.1. In winter and autumn, OA diurnal cycle mainly resulted from the superposition of both traffic-related and wood burning-related cycles with maxima of 4.9 µg m<sup>-3</sup> and 7.9 µg m<sup>-3</sup> for the morning and evening peak, respectively. This feature is highlighted by the seasonal diurnal profiles of the organic ion fractions f<sub>60</sub> and f<sub>57</sub>. While f<sub>60</sub> followed exactly the BC<sub>WB</sub> diurnal cycles, f<sub>57</sub> displayed the same bimodal pattern than BC<sub>FF</sub>. In spring and summer an additional local maximum appeared for OA during mid-day (3.8 µg m<sup>-3</sup>). This can be attributed to the enhanced photochemical activity and formation of secondary organic aerosol as suggested by the f<sub>44</sub> diurnal cycles. OA mid-day peaks may also be partly related to a distinct cooking source (Bozzetti et al., 2017). This is confirmed upon inspection of the f<sub>55</sub> vs f<sub>57</sub> plot (Figure S12), commonly used to diagnose the presence of this source (Mohr et al., 2012) as it shows a typical V-shape on daytime (05h-17h UTC), with data between 11h and 13h UTC (green points) and data from the morning (red and yellow points between 05h and 08h UTC) near the respective f<sub>55</sub>/f<sub>57</sub> fits previously reported for pure cooking organic aerosol and traffic emissions. During nighttime there is no clear separation of cooking and traffic-related organic aerosol as these sources are expected to be co-emitted at the same hours.

The NO<sub>3,Inorg</sub> diurnal cycles exhibit a morning peak that occurs in general 1-2 hours after the morning traffic-related peak, suggesting that formation of ammonium nitrate occurs locally in presence of the NO<sub>x</sub> and NH<sub>3</sub> possibly co-emitted emissions. Suarez-Bertoa et al. (2015) mentioned that urban traffic emissions of ammonia have increased in Europe (+378%) over the last decades leading to possible enhanced ammonium concentrations. In the late afternoon, concentrations increase

455 and remain high because of the boundary layer height decrease, together with the lower temperature and higher relative  
humidity that favour condensation to the particle phase. The diurnal variations of  $\text{NO}_{3,\text{Org}}$  are represented for each season in  
Figure 6. Concentrations increased after sunset and were higher at night, likely due to the oxidation of VOCs by the nitrate  
radical (Kiendler-Scharr et al., 2016). The minimum to maximum amplitude was more pronounced in summertime, possibly  
460 due to enhanced biogenic VOCs emissions. Still, these results might be partly influenced by the low level of total nitrate  
concentration encountered during this period. Slight daily enhancements of  $\text{NO}_{3,\text{Org}}$  were found in the morning (around 08:00  
UTC) and are attributed to photooxidation of VOCs in the presence of high nitrogen monoxide NO concentrations (the  
diurnal profiles are also reported in Figure 6 and show maxima at 07:00 UTC) as mentioned by Xu et al. (2015).  
Sulfate and ammonium exhibit very similar profiles, except for winter and early spring when ammonium is mainly  
associated to nitrate. The quite flat diurnal profiles of ammonium sulfate during autumn, winter, and spring might be due to  
465 the regional character of this component (regional transport) (Seinfeld and Pandis, 2016).  
In summer however, ammonium sulfate diurnal profile shows a clear increase during the daylight period with maxima  
reached at noon, possibly due to local photochemical production of sulfate from its precursor  $\text{SO}_2$  emitted by nearby  
shipping and industrial activities and advected to the city as the sea breeze sets in. Some studies suggest fast  $\text{SO}_2$  to sulfate  
conversion in the exhaust plumes (Healy et al., 2009; Lack et al., 2009). This local sulfate fraction will be discussed in detail  
470 in Section 3.4.2.  
Average daily profiles for  $\text{N}_1$  and  $\text{N}_2$  are represented in Figure 6 and show distinct daily pattern. Particle number  
concentration  $\text{N}_1$  exhibits maxima during morning and evening traffic rush hours similarly to NO concentration, when UFPs  
are mainly associated to vehicle exhaust emissions. In winter  $\text{N}_2$  follows the traffic bimodal profile with 1-2 hours shift  
(morning peak at starting at 06:00 UTC and evening at 17:00 UTC) which can highlight the fast homogeneous  
475 dilution/cooling (favoured by the low temperature and high relative humidity conditions) and mixing of the vehicle exhaust  
in the ambient air (Casati et al., 2007; Charron and Harrison, 2003). In summer,  $\text{N}_2$  exhibits a daily evolution with a broad  
maximum during daylight. This trend closely follows the daily evolution of temperature, ozone,  $\text{f}_{44}$  and  $\text{SO}_4^{2-}$  concentration  
suggesting a photo-oxidative process of gaseous precursors (Woo et al., 2001), as  $\text{SO}_2$ , combined with more dilution of  
pollutants when the boundary layer increases (Reche et al., 2011). For the transitional seasons (autumn and spring) the  
480 patterns reveal some mixing between the cars exhaust cooling and photochemistry states and  $\text{N}_2$  can be attributed to the two  
processes. Analysis of the secondary fraction  $\text{N}_2$  between 10 and 20 nm determined from SMPS summer data reveals that  
this fraction followed the  $\text{SO}_2$  diurnal evolution (Figure 6). Both  $\text{SO}_2$  and  $\text{N}_2$  ( $_{10-20 \text{ nm}}$ ) concentrations increased from the  
morning suggesting the nucleation of sulfuric acid particles (Burtcher, 2005; González et al., 2011). In this size range, the  
secondary ( $\text{N}_2$  ( $_{10-20 \text{ nm}}$ )) and fresh primary emissions ( $\text{N}_1$  ( $_{10-20 \text{ nm}}$ )) fractions corresponded to 90% and 10% of the total number  
485 concentration ( $\text{N}$  ( $_{10-20 \text{ nm}}$ )), respectively. Overall the UFPs investigation demonstrates that secondary particle formation is an  
important contributor to particle number in Marseille and besides road traffic, there is some high influence of  
industrial/shipping mixed sources.

## 3.2 Long-term trend of submicron aerosol

### 3.2.1 Seasonal patterns

490 Time series and seasonal contributions of ACSM components, Black Carbon and daily  $PM_{2.5}$  are shown in Figure 3. A  
summary of the seasonal statistics (average and standard deviation) is reported in table 1. The averaged concentration was  
9.9  $\mu\text{g m}^{-3}$  and 12.0  $\mu\text{g m}^{-3}$  for  $PM_{10}$  and  $PM_{2.5}$ , respectively. The mass concentrations measured by the BAM 1020 show a  
mass exceedance for this period at Marseille according to WHO recommendation (10  $\mu\text{g m}^{-3}$ ). The highest concentrations for  
 $PM_{10}$  were measured during winter with 11.9  $\mu\text{g m}^{-3}$  and the lowest in spring with 8.1  $\mu\text{g m}^{-3}$ . Several peaks reached 50  $\mu\text{g m}^{-3}$   
495 especially during cold periods in winter and autumn. The averaged  $PM_{10}$  chemical composition over the period is dominated  
by organics, (49.7%), and BC (17.1%) while sulfate accounts for 14.6%, nitrate for 10.2%, ammonium for 7.9% and chloride  
for 0.5% only. Past long-term studies on daily  $PM_{2.5}$  filters in MRS-LCP described similar yearly trend for those species  
(Bozzetti et al., 2017; Salameh et al., 2015): 44-46% for OM, 13% for BC (as EC measurements were performed during  
these studies, the value was multiplied by the BC/EC slope found in the present work to trace back to BC), 11% for sulfate,  
500 8% for nitrate, 7% for ammonium and less than 1% for chloride over the August 2011 to July 2012 period. This submicron  
aerosol composition is comparable to other Mediterranean coastal cities, where a noticeable proportion of sulfate is generally  
observed (Minguillón et al., 2015; Salameh et al., 2015; Stavroulas et al., 2019), whereas most urban sites in northern/central  
Europe show higher nitrate contribution (Lianou et al., 2011; Petit et al., 2015; Young et al., 2015). This is especially true in  
summer, where the highest contribution of sulfate to the total mass of  $PM_{10}$  is observed (24.1%). The present study confirms  
505 what had been previously reported during a short time summer measurement campaign with a C-ToF AMS (El Haddad et  
al., 2013). El Haddad et al. (2013) noticed that elevated sulfate periods corresponded to air masses transported from the  
Mediterranean Sea. The origin of sulfate aerosol is further examined in section 3.3.2.

The average carbonaceous fraction (OA+BC) contributes to 66.8% of the  $PM_{10}$  mass. By converting BC to EC with the  
510 previous slope of 1.52 (see section 3.1.) the carbonaceous fraction would be 64.8% which is high compared to the OM+EC  
contributions of  $PM_{2.5}$  from several urban sites in Europe (26 to 47%; Putaud et al., 2010). The OA dominance in every  
season is a common feature observed for European urban areas (Zhang et al., 2007b). Highest averaged values of 6.2  $\mu\text{g m}^{-3}$   
and 5.1  $\mu\text{g m}^{-3}$  are observed during winter and autumn months respectively (Figure S5). This trend was also observed in the  
2011-2012 period but higher concentrations were found, with 12.1  $\mu\text{g m}^{-3}$  in winter and 11.1  $\mu\text{g m}^{-3}$  in autumn (Bozzetti et  
515 al., 2017). The year 2011 showed particularly large amount of days with high level of  $PM_{2.5}$  in the autumn-winter period (43  
days exceeding WHO  $PM_{2.5}$  threshold value; table 2) which may explain this difference. BC seasonal cycle has a similar  
pattern with highest values of 2.1  $\mu\text{g m}^{-3}$  in winter and 1.9  $\mu\text{g m}^{-3}$  in autumn. These high carbonaceous concentrations during  
the cold months are expected considering i) a reduction of the planetary boundary layer (PBL) height resulting in the  
accumulation of pollutants at ground level compared to other seasons and ii) increasing emissions from residential heating  
520 and open combustion of green wastes (Bozzetti et al., 2017). The deconvolution of BC into two contributions, fossil fuel and

wood burning (respectively  $BC_{FF}$  and  $BC_{WB}$ ) was carried out using the aethalometer model (Sandradewi et al., 2008). As a first step the procedure recommended by Zotter et al. (2017) (i.e. to use the 470 and 950 nm wavelengths with an Angström exponent of 1.68 and 0.9 for pure wood burning and fossil fuel respectively) was applied. Using the suggested values led to unrealistic high  $BC_{WB}$  contributions in the summer (18%) when biomass burning is expected to be negligible during the hot period. It is hypothesised, as previously suggested by Titos et al. (2017), that a fraction of  $BC_{FF}$  was wrongly attributed to wood burning as a consequence of a failure of the model to reconstruct sources when the biomass burning fraction is very low. This potential bias was investigated on fossil fuel derived  $PM_{10}$  from a urban traffic site (station “Kaddouz”, location: 43°34'49.8" N; 5°37'49.3" E) during summer time. This kerbside site is located at the portal of a tunnel in the surrounding area of Marseille. In order to inspect the different combinations of Angström exponent for fossil fuel and wood burning ( $\alpha_{FF}$  and  $\alpha_{WB}$ , respectively) a sensitivity test was performed by scanning combination changes in a  $\alpha_{FF}$  range of 0.9–1.1 and a  $\alpha_{WB}$  range 1.6–2 with a step size of 0.01. The set of combinations was evaluated and optimized based on the  $BC_{WB}$  diurnal cycles, which were categorized according to a k means clustering analysis. Results are further described in the Supplement. From this analysis, a selected  $\alpha_{FF}$  of 1.02 would be more representative of fresh traffic emission in Marseille and Garg et al. (2016) suggested that  $\alpha_{FF} > 1$  could be more appropriate for older vehicles operating with poorly optimized engines. For  $\alpha_{WB}$ , the reference value of 1.68 from Zotter et al. (2017) has been used for this study.

Seasonal results of BC contributions in MRS LCP are shown in Figure 4 and statistic averages and standard deviations are reported in table 1.  $BC_{WB}$  shows a clear seasonal variability like OA with the highest contribution to the total BC in winter (28%). Despite the mild climate in South of France, wood heating is an important source of pollution which can be explained by the poor insulation in houses. Almost 15% of housing use wood for heating in Aix Marseille Metropolis (use of chimneys, wood stove or wood boiler) (ADEME, 2009) and around 50% of the identified equipment are still considered as non efficient in France (ADEME, 2020). Additionally, several wood fired heating plants located in Aubagne, Gardanne and Aix en Provence (15, 18 and 25 km from Marseille, respectively) might contribute to biomass burning emissions. Besides wood heating, the open burning is expected to contribute to the increasing OA+ $BC_{WB}$  concentrations, particularly in autumn. This includes the agricultural burning, since one third of the department surface area is dedicated to agricultural activities, but also the green waste burning. While this latter practice is prohibited, it is suspected to still be used nowadays. Summer  $BC_{WB}$  in MRS LCP represents the lowest contribution with 7%, which is in the same range than in Fos sur Mer (2%; Bonvalot et al., 2019) and another big Mediterranean coastal city like Athens (6%; Diapouli et al., 2017).

The  $BC_{FF}$  is still the main contributor to ambient black carbon (72–93% of total BC) with values ranging from 1.1 to 1.7  $\mu\text{g m}^{-3}$  throughout the seasons. The elevated BC concentrations could be explained by the proximity of the monitoring station to the city center and thus to local urban emissions. Vehicular emissions highly contribute to primary carbonaceous fraction in Marseille as demonstrated by El Haddad et al. (2011b) and can be a significant source for OA and  $BC_{FF}$ . Even if  $BC_{FF}$  is assumed to be an excellent marker of vehicular emissions (Herich et al., 2011), in Marseille other sources as oil fired boilers, industrial and shipping activities could contribute to total  $BC_{FF}$ .

Nitrate exhibits maximum contribution in winter and early spring (13.2% and 14.0%, with 1.58 and 1.13  $\mu\text{g m}^{-3}$  respectively) and minimum contribution during summer (2.6% with 0.24  $\mu\text{g m}^{-3}$ ). This feature has been already observed in other European cities (Minguillón et al., 2015; Petit et al., 2015; Reyes Villegas et al., 2016; Young et al., 2015). Bozzetti et al. (2017) observed lower fraction in spring possibly because of the volatilization of nitrate from the filters surface in warm conditions. Several episodes were reported mostly in late winter/early spring (described by elevated nitrate dispersion for February and March in Figure S5) and concentrations of other species also increased during these nitrate events conducting to highly polluted days. These episodes are investigated in section 3.3.1. Nitrate was further categorised into inorganic and organic fraction using the method described by Farmer et al. (2010). The detailed methodology is presented in SI.

Seasonal mass fraction of  $\text{NO}_{3,\text{Org}}$  and  $\text{NO}_{3,\text{Inorg}}$  are displayed in Figure 4.  $\text{NO}_{3,\text{Org}}$  average concentration ranges from 0.09  $\mu\text{g m}^{-3}$  in summer to 0.26  $\mu\text{g m}^{-3}$  in winter. The resulting average  $\text{NO}_{3,\text{Org}}$  fraction for the whole dataset is  $20 \pm 7\%$ . The error here is determined from error propagation calculations described by Farmer et al. (2010) and is detailed in SI. This fraction is in the range of reported values for European urban sites (28%, Mohr et al., 2012; 24%, Saarikoski et al., 2012). The highest  $\text{NO}_{3,\text{Org}}$  contribution happens to be in summer (38%) when the total nitrate concentration is at its lowest level.  $\text{NO}_{3,\text{Org}}$  is produced from volatile organic compounds (VOCs) oxidations by nitrate radicals and photochemical oxidation with  $\text{NO}_x$ . Biogenic VOCs emissions are high in summer in Mediterranean area (Parra et al., 2004; Steinbrecher et al., 2009) and provide an important potential source for organic nitrate formation.

$\text{NO}_{3,\text{Org}}$  takes into account only the nitrate functionality of organic nitrates. Assuming a molecular weight between 200 and 300  $\text{g mol}^{-1}$  for particle organic nitrates, contribution of organic nitrates to total OA can be estimated (Xu et al., 2015). Results presented in Table S4 give a contribution to total OA of about 6–10% in summer, 11–17% in autumn, 14–20% in winter and 18–28% in spring. Highest contributions in springtime can be due to increased level of biogenic VOCs coupled with favourable meteorological conditions for partitioning. These results suggest that despite the low contribution of  $\text{NO}_{3,\text{Org}}$  to total nitrate, organic nitrates can be an significant fraction of OA in Marseille.

The  $\text{NO}_{3,\text{Inorg}}$  average seasonal concentrations range from 0.15  $\mu\text{g m}^{-3}$  in summer to 1.31  $\mu\text{g m}^{-3}$  in winter. Here  $\text{NO}_{3,\text{Inorg}}$  was assumed to be mostly ammonium nitrate particles. Ammonium nitrate is semi volatile and its gas/particle partitioning is affected by temperature and relative humidity changes (Stelson and Seinfeld, 1982), which lead to enhanced particle partitioning during winter and higher evaporation during summer (Huffman et al., 2009). This is supported by Figure S5 where lowest temperature and highest relative humidity values are found in winter and early spring, while the inverse trend is illustrated for summer months.

Winter and springtime ammonium concentrations can be driven by the greater availability of ammonia from agricultural activity and waste management. Moreover Suarez Bertoa et al. (2015) mentioned that urban traffic emissions of ammonia have increased in Europe (+378%) over the last decades leading to possible enhanced ammonium concentrations. High concentrations of inorganic nitrate are related to elevated levels of  $\text{NO}_x$  in winter. This is described in Figure 1 where the hourly maximum concentrations of  $\text{NO}_x$  emissions mostly appear in winter seasons.

It is well known that ultrafine particles (UFPs; diameter <100nm) do not affect the mass concentrations but might be relevant for health related issues, and their long term variability is explored in this study. The total average UFPs number concentration (20–100 nm) measured with a TSI 3031 monitor over the full study was 7765 cm<sup>-3</sup>. These values are similar to those observed in Barcelona but are higher than those found in Prague, Madrid and Rome (Borsós et al., 2012; Brines et al., 2015). In Marseille, UFPs represented at 85% of total submicron particle number, in agreement with previous observations in urban environment (Rodríguez and Cuevas, 2007; Wehner and Wiedensohler, 2003). UFPs average concentration were slightly higher in winter and autumn with average values of 8600 cm<sup>-3</sup> and 8100 cm<sup>-3</sup>, respectively, while an average value of 7500 cm<sup>-3</sup> was found in spring and summer. The seasonal variation followed the general patterns observed for BC and OA concentrations over the year, suggesting that most particles in number arise from sources of combustion. However, when considering size distribution measurements down to 10 nm, SMPS data revealed the occurrence of sharp UFPs events more frequently in the summer than in winter, with 10 events exceeding 50 000 particles cm<sup>-3</sup> in summer against only 1 in winter (Figure 3). To get insights into the sources and processes contributing to ultrafine particles in urban ambient air, number concentrations and BC were investigated using the methodology developed by Rodríguez and Cuevas (2007). This methodology has been extensively applied in urban environment to apportion the number concentration of primary and secondary sources (del Águila et al., 2018; González et al., 2011; Hama et al., 2017a; Hama et al., 2017b; Reche et al., 2011; Rodríguez and Cuevas, 2007; Tobías et al., 2018). To refine the method, BC<sub>FE</sub> was used instead of total BC to better apportion primary traffic emissions. The total measured UFPs number concentration (N) can be splitted in two components:

605

$$N_1 = S_1 \cdot BC_{FE}, \quad (2)$$

$$N_2 = N - N_1, \quad (3)$$

where N<sub>1</sub> accounts for fresh primary emissions of vehicle exhaust, directly emitted in the particle phase or nucleating immediately after emission (Arnold et al., 2006; Burtscher, 2005; Kittelson, 1998) and N<sub>2</sub> accounts mostly for secondary particles formed in the atmosphere during the dilution and cooling of the exhaust emissions. S<sub>1</sub> is the slope estimated using best fit line to the points aligned in the lower edge of N vs BC<sub>FE</sub> scatter plot (see Figure S7 for details).

S<sub>1</sub> was calculated for each season by fitting data below the 10<sup>th</sup> percentile of N/BC<sub>FE</sub>. The N<sub>1</sub> and N<sub>2</sub> fractions were derived from the TSI 3031 measurements and average number concentrations during each season are reported in table 1 and Figure 4. The N<sub>2</sub> fraction was predominant with number concentrations 1.02 to 1.7 times higher than N<sub>1</sub>. The N<sub>1</sub> seasonal trend slightly varied through the measurement period with a contribution between 37 and 50%. These emissions appear to be dominant in winter and autumn, with average concentrations of ~4200 and 3800 cm<sup>-3</sup>. An explanation for these results could be either the higher traffic rate or the low temperature influencing the soot particle formation during combustion in these seasons. In contrast, the N<sub>2</sub> average particle numbers were higher in spring and summer as the concentrations reached its highest value (~4300 cm<sup>-3</sup> and 4800 cm<sup>-3</sup>). This behaviour will be further addressed in the following section.

620

### 3.2.2 Diurnal profiles

Figure 5 shows the average diurnal profiles of OA,  $\text{NH}_4^+$ ,  $\text{NO}_3^-$ ,  $\text{SO}_4^{2-}$ ,  $\text{BC}_{\text{FF}}$  and  $\text{BC}_{\text{WB}}$  across the different seasons. Distinctive diurnal patterns are found for carbonaceous aerosols. First, a clear traffic related diurnal profile is observed for  $\text{BC}_{\text{FF}}$  with a morning peak and an evening peak starting at the typical rush hours (04:00 UTC and 16:00 UTC respectively).  
625 The amplitude of the traffic related diurnal cycle seemed to be affected by meteorological conditions since it varied within the year, with maximum min to max amplitude of 0.9 during winter and minimum min to max amplitude of 0.5 during summer. The  $\text{BC}_{\text{WB}}$  had a significantly different diurnal cycle with a typical increase starting at 17:00 UTC and a maximum level of  $1.1 \mu\text{g m}^{-3}$  at night time.

The mean to max amplitude increased steadily from spring, autumn to winter (0.1, 0.2 and 0.4, respectively), following the  
630 increased heating demand. Under specific meteorological conditions (no rain, low wind speed, low boundary layer) this source led to the highest levels of  $\text{PM}_{10}$  episodes in Marseille. This is discussed in detail in Sect. 3.3.1. In winter and autumn, OA diurnal cycle mainly resulted from the superposition of both traffic related and wood burning related cycles with maxima of  $4.9 \mu\text{g m}^{-3}$  and  $7.9 \mu\text{g m}^{-3}$  for the morning and evening peak, respectively. In spring and summer an additional local maximum appeared during mid day ( $3.8 \mu\text{g m}^{-3}$ ). While this peak may partly be related to a distinct local source like  
635 cooking emissions (Bozzetti et al., 2017), formation of secondary organic aerosol is also expected, as observed by El Haddad et al. (2013).

The diurnal variations of  $\text{NO}_{3,\text{Org}}$  are represented for each season in Figure 5. Concentrations increased after sunset and were higher at night, likely due to the oxidation of VOCs by the nitrate radical (Kiendler Scharr et al., 2016). This trend was more pronounced in summertime with enhanced biogenic VOCs emissions. Summer  $\text{NO}_{3,\text{Org}}$  profile was investigated for June  
640 2017 when concentrations were above the detection limits. Slight daily enhancements of  $\text{NO}_{3,\text{Org}}$  were found in the morning (around 08:00 UTC) and are attributed to photooxidation of VOCs in the presence of high nitrogen monoxide  $\text{NO}$  concentrations (the diurnal profiles are also reported in Figure 5 and show maxima at 07:00 UTC) as mentioned by Xu et al. (2015). Similarly,  $\text{NO}_{3,\text{Inorg}}$  diurnal pattern suggests fast formation mechanism from local  $\text{NO}_x$  emissions. Concentrations are higher during night time when the condensation to the particle phase is favoured by meteorological conditions (low  
645 temperature and high relative humidity).

Sulfate and ammonium exhibit very similar profiles, except for winter and early spring when ammonium is mainly associated to nitrate. The quite flat diurnal profiles of ammonium sulfate during autumn, winter, and spring might be due to the regional character of this component (regional transport) (Seinfeld and Pandis, 2016).  
650 In summer however, ammonium sulfate diurnal profile shows a clear increase during the daylight period with maxima reached at noon, possibly due to local photochemical production of sulfate from its precursor  $\text{SO}_2$  emitted by nearby shipping and industrial activities and advected to the city as the sea breeze sets in. Some studies suggest fast  $\text{SO}_2$  to sulfate

conversion in the exhaust plumes (Healy et al., 2009; Lack et al., 2009). This local sulfate fraction will be discussed in detail in Section 3.3.2.

655 Average daily profiles for  $N_1$  and  $N_2$  are represented in Figure 5 and show some discrepancies. Particle number  $N_1$  exhibits maxima during morning and evening traffic rush hours similarly to  $NO$  concentrations, when UFPs are mainly associated to vehicle exhaust emissions. The  $N_2$  daily profiles display different diurnal patterns: in winter  $N_2$  follows the traffic bimodal profile with 1-2 hours shift (morning peak at starting at 06:00 UTC and evening at 17:00 UTC) which can highlight the fast homogeneous dilution/cooling (favoured by the low temperature and high relative humidity conditions) and mixing of the  
660 vehicle exhaust in the ambient air (Casati et al., 2007; Charron and Harrison, 2003). In summer,  $N_2$  exhibits a daily evolution with a broad maximum during daylight. This trend closely follows the daily evolution of temperature, ozone and  $SO_4^{2-}$  concentration suggesting a photo-oxidative process of gaseous precursors (Woo et al., 2001), as  $SO_2$ , combined with more dilution of pollutants when the boundary layer increases (Reche et al., 2011). For the transitional seasons (autumn and spring) the patterns reveal some mixing between the cars exhaust cooling and photochemistry states and  $N_2$  can be attributed  
665 to the two processes.

In order to investigate the UFPs apportionment below 20 nm the methodology was applied to SMPS data during the available summer period for a range between 10 and 20 nm. The  $N_{2,(10-20\text{ nm})}$  number concentration, corresponding to 90% of the total number in this range, showed the same trend of  $SO_2$  diurnal evolution (Figure 5). The  $SO_2$  is considered a gas tracer for industrial and shipping activity and it was advected to the monitoring station from the morning. Furthermore, both  $SO_2$   
670 and  $N_{2,(10-20\text{ nm})}$  concentrations increased suggesting the nucleation of sulfuric acid particles (Burtcher, 2005; González et al., 2011). Overall the UFPs investigation demonstrates that secondary particle formation is an important contributor to particle number in Marseille and besides road traffic, there is some high influence of industrial/shipping mixed sources.

### 3.4 Case Study of $PM_{10}$ polluted periods

#### 675 3.4.1 PM episodes with exceedance days: local vs long-range transport

Table 2 summarizes the number of  $PM_{2.5}$  exceedance days throughout the last decade in MRS-LCP, using as reference value  $25 \mu g m^{-3}$  24-hours mean from the WHO guideline for particulate matter. Overall, the number of exceedance days has strongly declined over the years (it is 3-4 times lower in 2017 than in the 2009-2011 period). In the present study, 15 exceedance days were observed over the 14 month-period (from 1 February 2017 to 13 April 2018). These exceedance  
680 periods occurred in spring, late autumn, and winter, in good agreement with seasonal frequency distribution in the last decade, and they could last from 1 to 4 consecutive days as shown in Figure 3. Among the 15 exceedance days, two pollution episodes have been selected as case studies, as they represent two contrasting pollution regimes: a local event in Christmas period (23-24 December 2017) and a regional persistent pollution episode (22-25 February 2018).

685 The average  $PM_{2.5}$  concentrations were  $31.2 \mu\text{g m}^{-3}$  and  $36.7 \mu\text{g m}^{-3}$  respectively for the local and regional pollution episodes, with average  $PM_1$  concentrations of  $28.7 \mu\text{g m}^{-3}$  and  $31.1 \mu\text{g m}^{-3}$ , respectively. This indicates that  $PM_{2.5}$  pollution episodes were driven by  $PM_1$  concentrations in both cases. Figure 7 shows the time series of the meteorological parameters (i.e. temperature, relative humidity, wind speed and direction, PBL height and precipitations), with the  $PM_1$  components as well as the  $BC/SO_4^{2-}$  ratio during these 2 events. The sulfate fraction ( $SO_4^{2-}$ ) is considered a good tracer for long-range transport, whereas BC refers to local influence from the city and the surrounding area (Petit et al., 2015). The use of this  
690 local/long-range proxy requires the assumption of minor local source of  $SO_2$  and no direct  $SO_4^{2-}$  formation in plumes at a local scale during the 2 episodes. Therefore the industrial and shipping contributions to global pollution have to be low for these periods. This is true except for a short period on the 23 December around 12:00 UTC when a temporary increase of  $SO_4^{2-}$  decreases the  $BC/SO_4^{2-}$  ratio. This short event possibly originated from industrial and/or shipping emissions as  $SO_2$  and UFPs concentrations also increased. Additionally, aged air masses might contain BC particles (Laborde et al., 2013) and this  
695 interference must be considered during the  $BC/SO_4^{2-}$  ratio analysis.

The Christmas local episode lasted two consecutive days: the 23 and 24 December 2017 (Figure 7a).  $PM_1$  (ACSM+BC) concentration was dominated by OA (63%) and BC (21%). Carbonaceous concentrations increased mostly in the evening by a factor of 4 to 5 in the space of a few minutes with the onset of the land breeze and remained high overnight. The temporal  
700 evolution of BC contributions (Figure 7a) clearly indicates a predominance of biomass burning with a maximum contribution of  $BC_{WB}$  to BC between 80-100% at night. At night  $PM$  size distribution ranged between 40 and 200 nm (Figure S13), typical of wood burning emissions (Coudray et al., 2009). High  $BC/SO_4^{2-}$  ratio (average of 6.12 with values up to 20) and low wind speed conditions suggests a strong local influence. This is supported by the NWR analysis plots for OA and the biomass markers ( $BC_{WB}$ ,  $f_{60}$ ) shown in Figure 8, indicating that high concentrations are associated to North-East land  
705 breeze.

This configuration is very frequent in Marseille, as land breeze regime prevailed 25% of the time, as shown by the wind roses, Figure S14. Under such meteorological conditions, the average annual  $PM_1$  concentration was  $14.3 \mu\text{g m}^{-3}$  instead of  $8.49 \mu\text{g m}^{-3}$  for the remaining period. These winds transport to the city anthropogenic emissions from the surrounding suburban residential areas of Marseille, in the north-easterly direction. In winter, these areas are a few degrees colder than  
710 the city of Marseille, resulting in an increased use of firewood as an auxiliary heating source. After the 25 December, the  $PM_1$  levels dropped down as the wind direction shifted from North-East to East/South-East. The  $PM_1$  decrease was also favoured by the vertical dilution that occurred with increased PBL height combined with precipitations.

The February long-range event took place during a period of four consecutive  $PM_{2.5}$  exceedance days from 22 to 25 February  
715 2017 (Figure 7b) and was ended as a higher PBL height led to the dilution of atmospheric pollutants. The aerosol chemical composition was relatively stable with OA contribution of 41%, followed by  $NO_3^-$  (25%), BC (12%),  $NH_4^+$  (11%), and  $SO_4^{2-}$  (10%). While this measurement period was not complemented by a SMPS, the comparison between the  $PM_1$  mass

concentrations found in both periods ( $31.1 \mu\text{g}\cdot\text{m}^{-3}$  for the February event and  $28.7 \mu\text{g}\cdot\text{m}^{-3}$  for the Christmas event) with their respective total number concentration as determined with the TSI 3031 ( $12800$  and  $22800 \text{ cm}^{-3}$ ) indicates that the mass-weighted particle size distributions was shifted to larger size during this episode (Figure 7c). This event is characterised by a low  $\text{BC}/\text{SO}_4^{2-}$  ratio (average of 1.13), suggesting advection of aged and processed air masses. The  $\text{BC}/\text{SO}_4^{2-}$  ratio can reach values of 4-5 though, when regional background concentrations are enriched by local BC emissions, contributing to enhanced particle level. The secondary origin of the aerosol is confirmed by the high content of ammonium nitrate. Figure 8 shows SWIM-2 analysis plot for  $\text{NO}_{3,\text{Inorg}}$  indicating that the main dominant wind sector for this species is North to South-West, with the highest concentration from North/North-West at high wind speed ( $\approx 1.8 \text{ m s}^{-1}$ ) and South/South-West at low wind speed ( $\approx 1.1 \text{ m s}^{-1}$ ). This result likely shows a combined local pollution with medium/long-range transport of secondary species during this time. In order to avoid local influences, wind regression analysis were conducted on  $\text{NO}_{3,\text{Inorg}}$  normalized by BC. The resulting plot shown in figure 8 reveals the North/North-West sector origin, corresponding to Mistral wind (wind speed between  $1.8$  and  $2.2 \text{ m s}^{-1}$ ) conditions. A similar result is obtained with  $f_{44}$  which suggests that a high fraction of secondary organic aerosol is also associated to this event.

Analysis of the 72h-backtrajectories ( $n=32$ ; displayed every 3 hours) displayed in Figure S15 shows that the air masses came essentially from Eastern and central Europe, passed over Switzerland and the northern Italy and were then channelled along the Rhone Valley corridor toward the Mediterranean Sea under Mistral regime. The CWT analysis for the nitrate supports this hypothesis since it shows a potential source region in the North-East part of the Pô Valley (Figure S15). The Pô Valley is well known for its high levels of inorganic (Diémoz et al., 2019; Schaap et al., 2004b; Squizzato et al., 2013) and secondary organic aerosol (Saarikoski et al., 2012). The plain is enclosed by the Alpine chain and the Apennines limiting the dispersion of pollutants and thus leading to frequent pollution events. During the winter/spring period low temperature and high humidity may favour ammonium nitrate particles formation (Schaap et al., 2004b). The hot spot along the Rhône valley can be connected to the intense nitrogen fertilization in this period causing high level of  $\text{NH}_3$  emissions in the area (Ramanantenasoa et al., 2018), and leading to enhanced ammonium nitrate formation. Additionally, industrial emissions from areas along the valley, such as the “Vallée de la Chimie” in the south of Lyon, can contribute to this episode.

The backtrajectories of a similar event occurring from the 14<sup>th</sup> to the 17<sup>th</sup> 14 to 17 of March are represented in Figure S9. The chemical composition was similar to that reported in the previous event ( $\text{OA} = 44\%$ ,  $\text{NO}_3^- = 26\%$ ,  $\text{NH}_4^+ = 11\%$ ,  $\text{BC} = 9\%$ ,  $\text{SO}_4^{2-} = 9\%$ ). Air masses were transported from the North direction through North Eastern part of France, Switzerland and North-Western part of Italy. Polluted air masses crossed continental regions known to be hotspots of ammonia emissions (the French Champagne-Ardennes region, the Swiss plateau, the Pô valley, as documented by Viatte et al., 2019), explaining partly the enhanced ammonium nitrate contribution during the winter/spring long range events.

As similarities can be found within the 15 exceedance days, it was possible to gather them in one of the two categories previously described (local event and regional/long-range event) according to some key criteria listed in Table S5. The local events were characterised by high  $\text{BC}/\text{SO}_4^{2-}$  ratio and an enrichment of  $\text{PM}_{2.5}$  concentration under land breeze. Local pollution is expected to be advected by land breeze, therefore  $\Delta\text{PM}_{2.5}$  (Land breeze/Other winds) should significantly increase

during these days. Local events were also heavily impacted by biomass burning particles as revealed by the high  $BC_{WB}$  contribution to  $PM_{2.5}$  ( $f_{BC_{FF} PM_{2.5}}$  in Table S5). Investigation of the ratio of  $f_{44}$  to  $f_{60}$  indicates that these are mostly fresh biomass emissions as evidenced by the high  $f_{60}$  ( $>0.01$ ) and low  $f_{44}$  ( $<0.01$ ) when particles concentrations are at their highest (30  $\mu g \cdot m^{-3}$ ) (Figure 9). For regional/long range episodes, the variability of  $f_{44}$  and  $f_{60}$  is larger as the aging degree of particles is expected to vary from one air mass to another and as the air masses may be affected by local biomass burning emissions. It is noteworthy that some observed values within the  $f_{60}$  background ( $\approx 0.3 \% \pm 0.06$ ; Cubison et al., 2011) denote no evidence of biomass burning emissions during these episodes.

The regional/long-range events were associated with an enhanced mass fraction of nitrate ( $f_{NO_3^- PM_{10}}$  in Table S5) and higher wind speeds occurring during these days. The probability density distributions of these criteria are presented in Figure 10. As expected the graphs show larger BC concentrations and  $f_{60}$  contributions during the local events, with a wind frequency dominated by land breeze ( $5^\circ$ - $90^\circ$ ) driving the pollution and to a lesser extent sea breeze and Mistral winds ( $210^\circ$ - $360^\circ$ ). Regional/long-range events were affected by higher  $NO_3^-$  concentrations and higher wind speeds. Even if  $f_{44}$  was slightly larger during these events, the distribution is in the same range than the one for local events. As mentioned previously the local pollution is combined to the long-range transport during these events, reducing the  $f_{44}$  values with the increasing hydrocarbon fragments contribution. This is supported by the wind frequency which, despite the Mistral dominance, is still affected by a low land breeze influence. In term of frequency of occurrence, 40% of exceedance days account for local origin (6 days) and 60% for long-range transport influence (9 days).

Globally, the combined observations of phenomenology, chemical composition and meteorology allow to accurately analyse events with exceedance mass concentrations for fine particles at MRS-LCP supersite, highlighting variable situations in an urban area affected by different air mass origins.

### 3.4.2 Sulfate origin and Shipping/industrial plumes in summer

The summertime aerosol contributes little to the exceedance of  $PM_{2.5}$  air quality thresholds (Figure 1). This season accounts for only 10% of the exceedance days since 2008 and none of these occurred in 2017-2018. Still, the high solar radiation and temperature combined to the dry condition are expected to enhance the formation of secondary pollutants and their accumulation. High ozone levels often exceeding the WHO threshold are indeed recorded in Marseille (section 3.1). These conditions also affect the aerosol composition as it results in an enhanced secondary sulfate fraction (see section 3.3.2). NWR plots of sulfate and its precursor  $SO_2$ , shown in Figure 8, indicate that their occurrence is preferentially associated the South-West sector, and covers a broad range of wind speeds. This wind sector is representative of the sea breeze conditions that prevail in summer and that blow inland coastal emission sources. Known local potential emissions sources include the large petrochemical and industrial area of Fos-Berre, located 40 km northwest, the shipping traffic in the gulf of Fos related to these activities and the Marseille harbour, located 3 km away from the site. During summertime, the ships traffic described as the sum of ship movements (arrivals and departures) increases by 25% (4319 movements against 3262

785 movements for the 2017-2018 period) partly because of the enhanced numbers of passenger ferries and travel cruises during the holiday season.

As shown by the NWR plot in Figure 7, high concentrations of sulfate are associated to a rather broad range of wind sectors and speeds, as expected for potentially aged and processes aerosol. While the geographic area where high sulfate concentrations are observed extend between the South West and the North East sectors, there is still a predominance from the South West sector. In this sector, prevalence of high concentrations of  $\text{SO}_2$ , the major precursor of sulfate aerosol, is also clearly observed. These  $\text{SO}_2$  concentrations are associated with high UFPs plumes. Figure 8 shows the averaged UFPs number concentrations and the seasonal frequency occurrence of peaks concentration according to  $\text{SO}_2$  concentrations classes. UFPs number increases with the enhanced  $\text{SO}_2$  levels, especially in the summer which involves more than 55% of the highest  $\text{SO}_2$  concentrations ( $>20\mu\text{g}/\text{m}^3$ ). Local sources of  $\text{SO}_2$  and UFPs include not only the large petrochemical and industrial area of Fos Berre, located 40 km northwest, but also the shipping traffic related to these activities in the gulf of Fos. Fresher emission of  $\text{SO}_2$  can originate from the port of Marseille, located 3 km away from the site. During summertime, the ships traffic increases by 25% (4319 against 3262 for the 2017-2018 period) partly because of the enhanced numbers of passenger ferries and travel cruises during the holiday season.

Figure 11 shows the diurnal trend of cumulative number of ship movements for the summer 2017. This number was differentiated according to the type of movement and the basin location (the exact geographic positions are reported in the Supplement in Figure S1). As can be seen by the diurnal profile of the ship movements in the harbour, two maxima were observed: the first at 05:00 UTC due to ship arrivals and the second at 17:00 UTC due to ship departures. Once the sea breeze sets in (06h00 UTC), the highest  $\text{SO}_2$  peak might be related to the ship arrivals increase; however, El Haddad et al. (2011a, 2013) assigned similar morning  $\text{SO}_2$  plumes to industrial activity from Fos-sur-mer in summer. Thus, the first  $\text{SO}_2$  increase could arise from a combination of contribution from ships arrival and industrial air masses, whereas the second peak could be mostly linked to the late afternoon boats departure. It should be noted that  $\text{SO}_2$  concentrations slightly increase earlier during the night (00h00-04h00 UTC) and can be linked to scarce wind advectons from the sea, also related to the ship traffic and not caught by the average wind diurnal cycle in Figure 11.  $\text{SO}_4^{2-}$  concentrations increased during the day and could be also partly affiliated to the direct influence of shipping/industrial activity to the monitoring site. In addition to these local sources, long range transport from the Mediterranean basin of sulfate and its precursor can also contribute to the levels of sulfate observed.

The variability of the summer daily patterns of sulfate was investigated using a k-means clustering algorithm run on the hourly concentrations. The method is further described in the Supplement. From this analysis, 3 distinct clusters were assessed, accounting for 20, 16 and 27 days for cluster 1, cluster 2 and cluster 3, respectively. The resulting average diurnal patterns of sulfate,  $\text{SO}_2$  and  $\text{N}_2$  (10-20nm) (whose diurnal profiles were found to be closely linked to  $\text{SO}_2$ , see section 3.3.3) and wind profiles are shown in Figure 12 for each cluster. The three clusters are confirmed to be mainly driven by the diurnal sea breeze cycle, that blows towards the city from 06h00-08h00 UTC to 20h00-21h00 UTC. Cluster 1 seems to be related to the

regional background of sulfate as it is associated with the lowest concentration ( $\approx 2\mu\text{g.m}^{-3}$ ) and a flat diurnal profile. Meanwhile,  $\text{SO}_2$  and  $\text{N}_{(10-20\text{ nm})}$  increase simultaneously as the breeze sets in to peak at  $4\mu\text{g m}^{-3}$  and  $8000\text{ cm}^{-3}$  respectively at 10h00-12h00. The comparison of the daily profiles indicates that sulfate is fully decoupled from its precursors in this cluster and that no significant conversion of  $\text{SO}_2$  to sulfate occurs by the time the air mass reaches the site.

On the contrary, cluster 2 gathers days when the sulfate concentrations are well correlated with the  $\text{N}_{2(10-20\text{ nm})}$  and  $\text{SO}_2$  daily profiles, that show maximum concentrations of  $6\mu\text{g m}^{-3}$  and  $6000\text{ cm}^{-3}$  at 12h00. Sulfate concentration peaks at the same time ( $\approx 3.5\mu\text{g.m}^{-3}$ ). The cycle may reflect the transport of rather fresh to moderately processed plumes that regularly reach the site. The molar ratio of sulfate to total sulfur, indicative of  $\text{SO}_2$ -to-sulfate conversion grows when photochemical activity is expected to be at its highest, from 0.3 (10h00) to 0.5 (16h00) (Figure S18). Based on this observation, it is hypothesized that this cluster is also representative of days when  $\text{SO}_2$  to sulfate conversion occurs.

In cluster 3, the sulfate concentration is found to progressively increase during the day and reaches a concentration of  $3\mu\text{g.m}^{-3}$  at 20h00.  $\text{SO}_2$  and  $\text{N}_{(10-20\text{ nm})}$  exhibit similar variations with 2 peaks at 08h00 ( $4\mu\text{g m}^{-3}$  ;  $3800\text{ cm}^{-3}$ ) and 17h00 ( $3\mu\text{g m}^{-3}$  ;  $3800\text{ cm}^{-3}$ ). It is presumed that cluster 3 is related to the most processed air masses as it exhibit the highest  $\text{SO}_4^{2-}$  to  $\text{SO}_2$  mean ratio (mean 06h00-19h00 value ; 0.58 against 0.45 and 0.39 for cluster 2 and 1, respectively).

NWR analyses were carried out to locate potential sources of sulfates nearby the site. In addition, CWT analyses were used to identify potential distant sources. Results from NWR and CWT for the three clusters are shown in Figure 13.

Cluster 1 is preferentially associated to the North-West sector (corresponding to the Mistral wind) and the area of the sea breeze having the highest speed as, indicated by the joint probability polar plot. The wind average wind speed was  $0.9\text{ m s}^{-1}$  against  $\approx 0.7\text{ m s}^{-1}$  for cluster 2 and 3, respectively. The NWR plots confirm the hypothesis on the potential origin of sulfate and  $\text{SO}_2$  in the 3 clusters: in the case of cluster 1, sulfate and  $\text{SO}_2$  are disconnected to each other, while they have the same south-westerly origin in cluster 2, as indicated by the similar hotspots in the plots (also displayed in Figure S19b). Cluster 3 exhibits moderate sulfate concentrations in a broader range of wind speed and in a larger South-West direction, consistent with a significant regional feature. The increasing sulfate concentrations from the South-West direction reach its maximum during early evening, as shown in Figure S19c. A South-East winds circulation can be more pronounced for some days of cluster 3, also contributing to the  $\text{SO}_4^{2-}$  enhancement (Figure S20). It should be emphasized that some rare land breeze from the North-East bring further background sulfate concentrations back to the city for the three clusters (Figure 13a).

On a larger scale, the CWT analysis of cluster 1 corresponds to a background level without a distinct origin. A clear hotspot in the South-West (also shown in Figure S19a) is connected to the night of 23 July corresponding to the end of a sulfate advection from cluster 3. The combination of the k-means clustering and the CWT analysis can suffer from this bias, as the times series that arise from the k-mean clustering are essentially segmented 24-hours periods. The CWT of sulfate for cluster 2 clearly shows a hotspot along the southern coast of France (“Golfe du Lion”) that encompasses the industrial area of Fos-sur-mer, while sulfate of cluster 3 is associated to air masses that expands over a larger area in the Mediterranean basin. The highest sulfate concentration are located on the main shipping routes in the Mediterranean, from the north of Spain, along the

French coast and the west coast of Italy (Nunes et al., 2020) This is not unexpected as the maritime shipping emissions have been estimated to account for more than 50% of the sulfate in the western Mediterranean (Aksoyoglu et al., 2016). These hotspots are also observed on the  $\text{SO}_2$  and  $\text{SO}_4^{2-}$  surface mass concentrations in summer 2017 from the MERRA2 model (Figure S21a and b), which is based on the Goddard Earth Observing System (GEOS) atmospheric data assimilation system (ADAS) (Gelaro et al., 2017).

The chemical composition and size distribution tend to support the distinct features identified between the 3 clusters: cluster 1 has the lowest concentration level, with  $7.7 \mu\text{g m}^{-3}$  against  $10.3 \mu\text{g m}^{-3}$  and  $9.9 \mu\text{g m}^{-3}$  for cluster 2 and 3, respectively. The greater influence of the local emission on cluster 2 than on cluster 3 is reflected by the higher black carbon content and the lowest sulfate content (Table S6 and Figure S22). It is also reflected by the higher total number concentration and a more pronounced Aitken mode observed on cluster 2 (Figure S23). Both Clusters 2 and 3 have an additional accumulation mode that has been already observed for aged aerosol passing over the Mediterranean Sea (Mallet et al., 2019).

To further investigate the large  $\text{SO}_4^{2-}$  concentrations in summer and their origin at a broader scale, a cluster analysis was carried out on the air masses reaching the site. From the analysis performed on the 72h backtrajectories, 3 distinct clusters were assessed from the total spatial variance (TSV) variation. Cluster 1 (Mediterranean origin) is related to air masses that circulate through western Mediterranean basin before arriving at MRS LCP site. Cluster 2 (sea breeze) corresponds to an initial low mistral blowing along the Rhone Valley seaward that returns to land the next day. Cluster 3, similarly to cluster 2, is representative of Mistral wind from the Rhone Valley but with higher speeds, as recorded at MRS LCP (average of  $1.01 \text{ m s}^{-1}$  against  $0.60$  and  $0.72 \text{ m s}^{-1}$  for cluster 1 and 2, respectively). Mean calculated trajectories are displayed in Figure S10. Cluster 3 associated to low pollutant levels won't be investigated in this study as its frequency is low (19%). In comparison, Mediterranean and sea breezes air masses account for 43% and 38%, respectively. While the clustering analysis clearly identifies the Mediterranean long range trajectories, Figure S11 shows that they still get mixed with the sea breeze when they approach the shore (as indicated by the wind sector  $190^\circ$ – $270^\circ$  characteristic of the sea breeze, and the by the sharp  $\text{SO}_2$  peaks included in the Mediterranean regime periods in pink). Still, discernible differences in the particle distribution and in the chemical composition are observed, as shown by Figure 10a and Figure 10b. Sea breeze cluster had a pronounced nucleation mode and Aitken mode ( $>10.25 \text{ nm}$  according to SMPS measurements) (Figure 10a). Mediterranean origin cluster has a broaden size distribution with combined Aitken and accumulation modes. Mallet et al. (2019) found similar results at Lampedusa site for air masses passing over the western Mediterranean. Particles from the sea breeze cluster might be smaller than Mediterranean origin cluster with the likelihood of fresher emission from the nearby shipping/industrial sources. Moreover the Box plots of  $\text{SO}_4^{2-}$ ,  $\text{SO}_2$  and  $\text{N}_{2(10-20 \text{ nm})}$  concentrations related to cluster 1 and 2 reveal that slightly higher  $\text{SO}_2$  ( $3.1$  vs  $2.6 \mu\text{g m}^{-3}$ ) and  $\text{N}_{2(10-20 \text{ nm})}$  ( $7855$  vs  $5740 \text{ cm}^{-3}$ ) concentrations are encountered with cluster 2, while higher  $\text{SO}_4^{2-}$  concentrations are observed with cluster 1 ( $3.2 \mu\text{g m}^{-3}$  against  $1.9 \mu\text{g m}^{-3}$  for sea breeze).

In an effort to further investigate the characteristics of the sulfate constituents, the total  $\text{SO}_4^{2-}$  was first tentatively deconvolved into ammonium sulfate, organosulfate and MSA (methanesulfonic acid) following the methodology developed by Chen et al. (2019) and based on  $\text{HSO}_3^+$  (f81) and  $\text{H}_2\text{SO}_4^+$  (f98) ion fractions from AMS measurements. The resulting

$\text{H}_2\text{SO}_4^+$  vs  $\text{fHSO}_3^+$  data points are displayed in Figure 12 and are color coded according to the different air masses (Sea breeze and Mediterranean origin). The results show that ammonium sulfate was the dominant source for ToF ACSM sulfate signals during this period. This was confirmed by the  $\text{NH}_4^+_{\text{measured}}/\text{NH}_4^+_{\text{predicted}}$  ratio close to 1 (Figure S4), showing that  $\text{SO}_4^{2-}$  was always fully neutralized by  $\text{NH}_4^+$  at MRS LCP site. It is hypothesised that even local emissions have enough time to mix with ammonia from urban environment to fully neutralize before reaching the station: considering a minimum distance between the harbour and MRS LCP of 3 km and an average sea breeze wind speed between  $1.05 \text{ m s}^{-1}$  and  $2.7 \text{ m s}^{-1}$  (measured from a harbour meteo station under the same sea breeze blowing direction) it takes at least around 20-45 minutes for a plume to reach the station. This agrees with Celik et al. (2020) who observed that shipping plumes older than 40 min were mostly neutralized with the ambient  $\text{NH}_3$  from a cleaner environment.

In order to trace the geographical origin of  $\text{SO}_4^{2-}$  from MRS LCP at a regional scale, CWT analysis were performed and the results are shown in Figure 11. A weighting function has been implemented to avoid artefacts linked to high concentrations with low number of trajectories passing through a particular cell. The aim is to avoid local sulfate influence from the transport model. Following Waked et al. (2014) recommendations a discrete function based on back trajectory density ( $\log_{10}(n+1)$ ) was applied (using the ZeFir tool on Igor). CWT on  $\text{SO}_4^{2-}$  from cluster 1 (Figure 11a) pointed out the combined influence of low Mistral advection from the Rhone Valley and the switch into South Westerly thermic breeze, in agreement with the expectations. CWT for cluster 2 (Figure 11b) exhibited long range transport, with  $\text{SO}_4^{2-}$  concentrations associated to the south and western Mediterranean air mass circulation. In the basis of this, several sources can be related to sulfate emissions in the Mediterranean Sea such as shipping activity, marine biogenic or crustal origin (Becagli et al., 2012).

#### 905 4 Summary and conclusions

The chemical composition of submicron aerosols was monitored in real time between 1 February 2017 and 13 April 2018 at an urban background site of the Mediterranean city of Marseille. Measurements were carried out with a ToF-ACSM associated with a suite of collocated instruments including an aethalometer, an ultrafine particle monitor, a SMPS and monitors for regulated pollutants (PM,  $\text{NO}_x$ ,  $\text{O}_3$ ,  $\text{SO}_2$ ).

910 The reconstituted  $\text{PM}_1$  mass (ACSM measurements + BC) was cross validated through several comparisons with external parameters. ACSM+BC concentrations were found to be in good agreement with estimated mass concentrations from SMPS ( $R^2=0.81$  and slope=1.02) and  $\text{PM}_1$  concentrations from FIDAS ( $R^2=0.89$  and slope=0.9).

OA was the most abundant specie of submicron aerosol, with an annual average of 49.7% and the carbonaceous fraction was dominant for every season (66.8%) and especially during cold months. BC contributes largely to this fraction (17.1% of total submicron aerosol) and is mainly dominated by fossil fuel emissions as determined with the AE-33 aethalometer model. BC from wood burning emissions showed higher contribution during winter and very low contribution in summer, as expected.

915

The organic nitrate contribution was evaluated using the  $\text{NO}_2^+/\text{NO}^+$  ratio method and gave reasonable results in separating  $\text{NO}_{3,\text{Org}}$  and  $\text{NO}_{3,\text{Inorg}}$  concentrations. Some uncertainties still remain as  $R_{\text{ON}}$  was set to a fixed value and could slightly vary according to the VOC precursors which lead to particle organic nitrate formation. Also, low nitrate signal provide instable  
920  $R_{\text{obs}}$  and could enhance the uncertainty of the estimation. The  $\text{NO}_{3,\text{Org}}$  fraction was  $20 \pm 7\%$  for the total nitrate (representing 10.2% on average for the  $\text{PM}_{10}$  concentrations) during the entire period and did not significantly contribute to enhanced polluted events with high  $\text{PM}_{10}$  concentrations. However organic nitrate contribution to total OA could be estimated to significant values with maximum during springtime (18-28%).

Particle number concentration was successfully segregated into two components ( $N_1$  and  $N_2$ ) by using the minimum slope  
925 found in the  $N$  vs  $\text{BC}_{\text{FF}}$  plot, with  $\text{BC}_{\text{FF}}$  accounting for primary particles.  $N_1$  was attributed to fresh primary traffic emissions and  $N_2$  to secondary particles. The secondary  $N_2$  fraction was predominant with number concentrations 1.02 to 1.7 times higher than  $N_1$ . While  $N_1$  showed clear maxima during morning and evening traffic rush hours,  $N_2$  was either attributed to dilution/cooling and mixing of vehicular exhausts in the atmosphere during cold seasons or to photooxidation products of gaseous precursors during hot seasons. These results revealed the importance of secondary particle formation and contrasted  
930 seasonal sources of UFPs number.

$\text{PM}_{10}$  pollution events were determined according to the daily concentrations exceeded WHO recommendations. To illustrate their differences in chemical composition, meteorological dynamic and geographical origins two events (23-24 December 2017 and 22-25 February 2018) were carefully examined.  $\text{BC}/\text{SO}_4^{2-}$  ratio, non-parametric wind regressions and backtrajectories provided important information to discriminate local and long-range transport contributions. The local  
935 contribution during exceedance days is attributed to an increase of biomass burning emissions with domestic heating and green wastes burning, cumulated with intense traffic. In those situations, the OA and BC concentrations strongly increase at night in the space of few minutes when the nocturnal land breeze set up and the boundary layer height decreases. The long-range pollution case, led to high increase of secondary aerosol, more precisely ammonium nitrate and oxygenated OA, transported from the central Europe and notably Pô Valley to the city. [The investigation of the total  \$\text{PM}\_{2.5}\$  exceedance days \(based on  \$f\_{44}/f\_{60}\$  ratio, BC contribution to  \$\text{PM}\_{2.5}\$ , nitrate contribution to  \$\text{PM}\_{10}\$ , wind speed and  \$\Delta\text{PM}\_{2.5}\$  \(Land breeze/Other winds\)\)](#)  
940 highlighted that local influences are mainly responsible of continuous background pollution and its mix with long-range transport events can trigger to situation with high exceedance levels of fine particles. This elevated pollution occurred mostly in winter and early spring with favourable wind conditions. Even if no exceedance day was found during the summer season, the chemical composition is slightly different, with higher sulfate contributions and intense UFPs plumes (mostly between  
945 10 and 20 nm) associated with  $\text{SO}_2$  are advected on site. ~~Air mass clustering has been performed to explain the observed differences in aerosol composition and highlighted the presence of local and regional emissions of shipping activity, mixed with industrial plumes in Marseille. This configuration is expected in a coastal city with a consequent harbour and in the vicinity of an industrial area. First sea breeze blowing results in a local advection of  $\text{SO}_2$ , UFPs and  $\text{SO}_4^{2-}$  from the industrial/shipping plumes. Then regional Mediterranean air masses can bring higher sulfate concentrations and larger  
950 particles from aged shipping plumes, probably mixed with other sources such as marine biogenic or crustal. For both cases it~~

has been shown that sulfate was completely and rapidly neutralized suggesting that ammonium sulfate predominates in the Mediterranean Sea. A k-means clustering analysis has been performed to inspect sulfate variability from summer days which can be driven by several origins. Over the 63 days including in the analysis, 20 days were attributed to background sulfate concentrations, and 16 days to enhanced concentrations under the direct influence of the harbour and industrial areas. The remaining days (27) were attributed to mixed sulfate sources with a regional influence. In addition to local industrial and shipping activity, regional Mediterranean air masses can bring higher sulfate concentrations from aged shipping plumes, probably mixed with other sources such as marine biogenic or crustal.

In conclusion, the supersite MRS-LCP successfully recorded up to 1 year observations and seasonality of fine particles. The long-term real-time monitoring in MRS-LCP showed a great potential and will supply direct information to public authorities and citizens. It may provide better understanding of pollution episodes and more effective control of local mitigation within the context of French Atmosphere Protection Plan.

**Data availability.** Data are available upon request to the contact author Benjamin Chazeau (benjamin.chazeau@univ-amu.fr).

**Author contributions.** NM designed the research. BC, GG and BM contributed to the measurements. BC performed the analysis and wrote the paper. NM, BD, BT and HW reviewed and all authors commented on the paper.

**Competing interests.** The authors declare they have no conflict of interest.

**Acknowledgements.** This work is supported by AtmoSud, ANRT, the PACA Region and the French ministry of Environment. BC also acknowledges V Crenn and ADDAIR for the ToF-ACSM support, D Piga and J Poulidor for the supply of shipping and road traffic data and J-E Petit for developing Zefir tool. Some visualization used in this paper were produced with the Giovanni online data system, developed and maintained by the NASA GES DISC.

## References

- ADEME: La maîtrise de l'énergie dans les logements en Paca., 2009.
- ADEME: Le bois énergie et la qualité de l'air, ademe.fr <https://www.ademe.fr/expertises/energies-renouvelables-en-production-reseaux-stockage/passer-a-l'action/produire-chaaleur/dossier/bois-biomasse/bois-energie-qualite-lair>, last access: 31 March 2020, 2020.
- del Águila, A., Sorribas, M., Lyamani, H., Titos, G., Olmo, F. J., Arruda-Moreira, G., Yela, M. and Alados-Arboledas, L.: Sources and physicochemical characteristics of submicron aerosols during three intensive campaigns in Granada (Spain), Atmospheric Research, 213, 398–410, <https://doi.org/10.1016/j.atmosres.2018.06.004>, 2018.

- Aiken, A. C., DeCarlo, P. F., Kroll, J. H., Worsnop, D. R., Huffman, J. A., Docherty, K. S., Ulbrich, I. M., Mohr, C., Kimmel, J. R., Sueper, D., Sun, Y., Zhang, Q., Trimborn, A., Northway, M., Ziemann, P. J., Canagaratna, M. R., Onasch, T. B., Alfarra, M. R., Prevot, A. S. H., Dommen, J., Duplissy, J., Metzger, A., Baltensperger, U. and Jimenez, J. L.: O/C and OM/OC Ratios of Primary, Secondary, and Ambient Organic Aerosols with High-Resolution Time-of-Flight Aerosol Mass Spectrometry, *Environmental Science & Technology*, 42(12), 4478–4485, <https://doi.org/10.1021/es703009q>, 2008.
- 985 Aksoyoglu, S., Baltensperger, U. and Prévôt, A. S. H.: Contribution of ship emissions to the concentration and deposition of air pollutants in Europe, *Atmos. Chem. Phys.*, 16(4), 1895–1906, <https://doi.org/10.5194/acp-16-1895-2016>, 2016.
- 990 Alfarra, M. R., Prevot, A. S. H., Szidat, S., Sandradewi, J., Weimer, S., Lanz, V. A., Schreiber, D., Mohr, M. and Baltensperger, U.: Identification of the Mass Spectral Signature of Organic Aerosols from Wood Burning Emissions, *Environmental Science & Technology*, 41(16), 5770–5777, <https://doi.org/10.1021/es062289b>, 2007.
- Arnold, F., Pirjola, L., Aufmhoff, H., Schuck, T., Lahde, T. and Hameri, K.: First gaseous sulfuric acid measurements in automobile exhaust: Implications for volatile nanoparticle formation, *Atmospheric Environment*, 40(37), 7097–7105, <https://doi.org/10.1016/j.atmosenv.2006.06.038>, 2006.
- 995 Ashbaugh, L. L., Malm, W. C. and Sadeh, W. Z.: A residence time probability analysis of sulfur concentrations at Grand Canyon National Park, *Atmospheric Environment* (1967), 19(8), 1263–1270, [https://doi.org/10.1016/0004-6981\(85\)90256-2](https://doi.org/10.1016/0004-6981(85)90256-2), 1985.
- Aurela, M., Saarikoski, S., Niemi, J. V., Canonaco, F., Prevot, A. S. H., Frey, A., Carbone, S., Kousa, A. and Hillamo, R.: Chemical and Source Characterization of Submicron Particles at Residential and Traffic Sites in the Helsinki Metropolitan Area, Finland, *Aerosol and Air Quality Research*, 15(4), 1213–1226, <https://doi.org/10.4209/aaqr.2014.11.0279>, 2015.
- 1000 Bahreini, R., Ervens, B., Middlebrook, A. M., Warneke, C., de Gouw, J. A., DeCarlo, P. F., Jimenez, J. L., Brock, C. A., Neuman, J. A., Ryerson, T. B., Stark, H., Atlas, E., Brioude, J., Fried, A., Holloway, J. S., Peischl, J., Richter, D., Walega, J., Weibring, P., Wollny, A. G. and Fehsenfeld, F. C.: Organic aerosol formation in urban and industrial plumes near Houston and Dallas, Texas, *Journal of Geophysical Research*, 114, <https://doi.org/10.1029/2008JD011493>, 2009.
- 1005 Bozzetti, C., El Haddad, I., Salameh, D., Daellenbach, K. R., Fermo, P., Gonzalez, R., Minguillón, M. C., Iinuma, Y., Poulain, L., Elser, M., Müller, E., Slowik, J. G., Jaffrezo, J.-L., Baltensperger, U., Marchand, N. and Prévôt, A. S. H.: Organic aerosol source apportionment by offline-AMS over a full year in Marseille, *Atmospheric Chemistry and Physics*, 17(13), 8247–8268, <https://doi.org/10.5194/acp-17-8247-2017>, 2017.
- 1010 Bressi, M., Cavalli, F., Belis, C. A., Putaud, J.-P., Fröhlich, R., Martins dos Santos, S., Petralia, E., Prévôt, A. S. H., Berico, M., Malaguti, A. and Canonaco, F.: Variations in the chemical composition of the submicron aerosol and in the sources of the organic fraction at a regional background site of the Po Valley (Italy), *Atmospheric Chemistry and Physics*, 16(20), 12875–12896, <https://doi.org/10.5194/acp-16-12875-2016>, 2016.
- Brines, M., Dall&apos;Osto, M., Beddows, D. C. S., Harrison, R. M., Gómez-Moreno, F., Núñez, L., Artíñano, B., 1015 Costabile, F., Gobbi, G. P., Salimi, F., Morawska, L., Sioutas, C. and Querol, X.: Traffic and nucleation events as main

- sources of ultrafine particles in high-insolation developed world cities, *Atmospheric Chemistry and Physics*, 15(10), 5929–5945, <https://doi.org/10.5194/acp-15-5929-2015>, 2015.
- Burtscher, H.: Physical characterization of particulate emissions from diesel engines: a review, *Journal of Aerosol Science*, 36(7), 896–932, <https://doi.org/10.1016/j.jaerosci.2004.12.001>, 2005.
- 1020 Cachier, H., Aulagnier, F., Sarda, R., Gautier, F., Masclet, P., Besombes, J.-L., Marchand, N., Despiiau, S., Croci, D., Mallet, M., Laj, P., Marinoni, A., Deveau, P.-A., Roger, J.-C., Putaud, J.-P., Van Dingenen, R., Dell’Acqua, A., Viidanoja, J., Martins-Dos Santos, S., Liousse, C., Cousin, F., Rosset, R., Gardrat, E. and Galy-Lacaux, C.: Aerosol studies during the ESCOMPTE experiment: an overview, *Atmospheric Research*, 74(1–4), 547–563, <https://doi.org/10.1016/j.atmosres.2004.06.013>, 2005.
- 1025 Canagaratna, M. R., Jayne, J. T., Jimenez, J. L., Allan, J. D., Alfarra, M. R., Zhang, Q., Onasch, T. B., Drewnick, F., Coe, H., Middlebrook, A., Delia, A., Williams, L. R., Trimborn, A. M., Northway, M. J., DeCarlo, P. F., Kolb, C. E., Davidovits, P. and Worsnop, D. R.: Chemical and microphysical characterization of ambient aerosols with the aerodyne aerosol mass spectrometer, *Mass Spectrometry Reviews*, 26(2), 185–222, <https://doi.org/10.1002/mas.20115>, 2007.
- Canagaratna, M. R., Jimenez, J. L., Kroll, J. H., Chen, Q., Kessler, S. H., Massoli, P., Hildebrandt Ruiz, L., Fortner, E.,
- 1030 Williams, L. R., Wilson, K. R., Surratt, J. D., Donahue, N. M., Jayne, J. T. and Worsnop, D. R.: Elemental ratio measurements of organic compounds using aerosol mass spectrometry: characterization, improved calibration, and implications, *Atmospheric Chemistry and Physics*, 15(1), 253–272, <https://doi.org/10.5194/acp-15-253-2015>, 2015.
- Canonaco, F., Slowik, J. G., Baltensperger, U. and Prévôt, A. S. H.: Seasonal differences in oxygenated organic aerosol composition: implications for emissions sources and factor analysis, *Atmospheric Chemistry and Physics*, 15(12), 6993–
- 1035 7002, <https://doi.org/10.5194/acp-15-6993-2015>, 2015.
- Casati, R., Scheer, V., Vogt, R. and Benter, T.: Measurement of nucleation and soot mode particle emission from a diesel passenger car in real world and laboratory in situ dilution, *Atmospheric Environment*, 41(10), 2125–2135, <https://doi.org/10.1016/j.atmosenv.2006.10.078>, 2007.
- Cavalli, F., Viana, M., Yttri, K. E. and Genberg, J.: Toward a standardised thermal-optical protocol for measuring
- 1040 atmospheric organic and elemental carbon: the EUSAAR protocol, *Atmos. Meas. Tech.*, 11, 2010.
- Charron, A. and Harrison, R. M.: Primary particle formation from vehicle emissions during exhaust dilution in the roadside atmosphere, *Atmospheric Environment*, 37(29), 4109–4119, [https://doi.org/10.1016/S1352-2310\(03\)00510-7](https://doi.org/10.1016/S1352-2310(03)00510-7), 2003.
- Coudray, N., Dieterlen, A., Roth, E. and Trouvé, G.: Density measurement of fine aerosol fractions from wood combustion sources using ELPI distributions and image processing techniques, *Fuel*, 88(5), 947–954, <https://doi.org/10.1016/j.fuel.2008.12.013>, 2009.
- 1045 Cross, E. S., Slowik, J. G., Davidovits, P., Allan, J. D., Worsnop, D. R., Jayne, J. T., Lewis, D. K., Canagaratna, M. and Onasch, T. B.: Laboratory and Ambient Particle Density Determinations using Light Scattering in Conjunction with Aerosol Mass Spectrometry, *Aerosol Science and Technology*, 41(4), 343–359, <https://doi.org/10.1080/02786820701199736>, 2007.

- Cubison, M. J., Ortega, A. M., Hayes, P. L., Farmer, D. K., Day, D., Lechner, M. J., Brune, W. H., Apel, E., Diskin, G. S.,  
1050 Fisher, J. A., Fuelberg, H. E., Hecobian, A., Knapp, D. J., Mikoviny, T., Riemer, D., Sachse, G. W., Sessions, W., Weber, R.  
J., Weinheimer, A. J., Wisthaler, A. and Jimenez, J. L.: Effects of aging on organic aerosol from open biomass burning  
smoke in aircraft and laboratory studies, *Atmospheric Chemistry and Physics*, 11(23), 12049–12064,  
<https://doi.org/10.5194/acp-11-12049-2011>, 2011.
- Department for Transport: Road traffic statistics, <https://roadtraffic.dft.gov.uk/regions/6>, 2020.
- 1055 Diapouli, E., Kalogridis, A.-C., Markantonaki, C., Vratolis, S., Fetfatzis, P., Colombi, C. and Eleftheriadis, K.: Annual  
Variability of Black Carbon Concentrations Originating from Biomass and Fossil Fuel Combustion for the Suburban Aerosol  
in Athens, Greece, *Atmosphere*, 8(12), 234, <https://doi.org/10.3390/atmos8120234>, 2017.
- Diémoz, H., Barnaba, F., Magri, T., Pession, G., Dionisi, D., Pittavino, S., Tombolato, I. K. F., Campanelli, M., Della Ceca,  
L. S., Hervo, M., Di Liberto, L., Ferrero, L. and Gobbi, G. P.: Transport of Po Valley aerosol pollution to the northwestern  
1060 Alps – Part 1: Phenomenology, *Atmospheric Chemistry and Physics*, 19(5), 3065–3095, <https://doi.org/10.5194/acp-19-3065-2019>, 2019.
- Draxler, R., Stunder, B., Rolph, G., Stein, A. and Taylor, A.: HYSPLIT4 User’s Guide, , 254, n.d.
- Drinovec, L., Močnik, G., Zotter, P., Prévôt, A. S. H., Ruckstuhl, C., Coz, E., Rupakheti, M., Sciare, J., Müller, T.,  
Wiedensohler, A. and Hansen, A. D. A.: The “dual-spot” Aethalometer: an improved measurement of aerosol black carbon  
1065 with real-time loading compensation, *Atmospheric Measurement Techniques*, 8(5), 1965–1979, <https://doi.org/10.5194/amt-8-1965-2015>, 2015.
- Drobinski, P., Saïd, F., Ancellet, G., Arteta, J., Augustin, P., Bastin, S., Brut, A., Caccia, J. L., Campistron, B., Cautenet, S.,  
Colette, A., Coll, I., Corsmeier, U., Cros, B., Dabas, A., Delbarre, H., Dufour, A., Durand, P., Guénard, V., Hasel, M.,  
Kalthoff, N., Kottmeier, C., Lasry, F., Lemonsu, A., Lohou, F., Masson, V., Menut, L., Moppert, C., Peuch, V. H.,  
1070 Puygrenier, V., Reitebuch, O. and Vautard, R.: Regional transport and dilution during high-pollution episodes in southern  
France: Summary of findings from the Field Experiment to Constraint Models of Atmospheric Pollution and Emissions  
Transport (ESCOMPTE): POLLUTION TRANSPORT AND DILUTION IN SOUTHERN FRANCE, *Journal of  
Geophysical Research: Atmospheres*, 112(D13), n/a-n/a, <https://doi.org/10.1029/2006JD007494>, 2007.
- El Haddad, I., Marchand, N., Temime-Roussel, B., Wortham, H., Piot, C., Besombes, J.-L., Baduel, C., Voisin, D.,  
1075 Armengaud, A. and Jaffrezo, J.-L.: Insights into the secondary fraction of the organic aerosol in a Mediterranean urban area:  
Marseille, *Atmospheric Chemistry and Physics*, 11(5), 2059–2079, <https://doi.org/10.5194/acp-11-2059-2011>, 2011a.
- El Haddad, I., Marchand, N., Wortham, H., Piot, C., Besombes, J.-L., Cozic, J., Chauvel, C., Armengaud, A., Robin, D. and  
Jaffrezo, J.-L.: Primary sources of PM<sub>2.5</sub> organic aerosol in an industrial Mediterranean city, Marseille, *Atmospheric  
Chemistry and Physics*, 11(5), 2039–2058, <https://doi.org/10.5194/acp-11-2039-2011>, 2011b.
- 1080 El Haddad, I., D’Anna, B., Temime-Roussel, B., Nicolas, M., Boreave, A., Favez, O., Voisin, D., Sciare, J., George, C.,  
Jaffrezo, J.-L., Wortham, H. and Marchand, N.: Towards a better understanding of the origins, chemical composition and

- aging of oxygenated organic aerosols: case study of a Mediterranean industrialized environment, Marseille, *Atmospheric Chemistry and Physics*, 13(15), 7875–7894, <https://doi.org/10.5194/acp-13-7875-2013>, 2013.
- Escudero, M., Lozano, A., Hierro, J., Valle, J. del and Mantilla, E.: Urban influence on increasing ozone concentrations in a characteristic Mediterranean agglomeration, *Atmospheric Environment*, 99, 322–332, <https://doi.org/10.1016/j.atmosenv.2014.09.061>, 2014.
- European Environment Agency: Air quality in Europe: 2019 report. [https://op.europa.eu/publication/manifestation\\_identifier/PUB\\_THAL19012ENN](https://op.europa.eu/publication/manifestation_identifier/PUB_THAL19012ENN), last access: 27 May 2020, 2019.
- European Environment Agency.: Air quality in Europe: 2020 report., Publications Office, LU. <https://data.europa.eu/doi/10.2800/786656>, last access: 16 February 2021, 2020.
- Farmer, D. K., Matsunaga, A., Docherty, K. S., Surratt, J. D., Seinfeld, J. H., Ziemann, P. J. and Jimenez, J. L.: Response of an aerosol mass spectrometer to organonitrates and organosulfates and implications for atmospheric chemistry, *Proceedings of the National Academy of Sciences*, 107(15), 6670–6675, <https://doi.org/10.1073/pnas.0912340107>, 2010.
- Flaounas, E., Coll, I., Armengaud, A. and Schmechtig, C.: The representation of dust transport and missing urban sources as major issues for the simulation of PM episodes in a Mediterranean area, *Atmos. Chem. Phys.*, 11, 2009.
- Frenay, E. J., Sellegri, K., Canonaco, F., Boulon, J., Hervo, M., Weigel, R., Pichon, J. M., Colomb, A., Prévôt, A. S. H. and Laj, P.: Seasonal variations in aerosol particle composition at the puy-de-Dôme research station in France, *Atmospheric Chemistry and Physics*, 11(24), 13047–13059, <https://doi.org/10.5194/acp-11-13047-2011>, 2011.
- Fröhlich, R., Cubison, M. J., Slowik, J. G., Bukowiecki, N., Prévôt, A. S. H., Baltensperger, U., Schneider, J., Kimmel, J. R., Gonin, M., Rohner, U., Worsnop, D. R. and Jayne, J. T.: The ToF-ACSM: a portable aerosol chemical speciation monitor with TOFMS detection, *Atmospheric Measurement Techniques*, 6(11), 3225–3241, <https://doi.org/10.5194/amt-6-3225-2013>, 2013.
- Fröhlich, R., Cubison, M. J., Slowik, J. G., Bukowiecki, N., Canonaco, F., Croteau, P. L., Gysel, M., Henne, S., Herrmann, E., Jayne, J. T., Steinbacher, M., Worsnop, D. R., Baltensperger, U. and Prévôt, A. S. H.: Fourteen months of on-line measurements of the non-refractory submicron aerosol at the Jungfraujoch (3580 m a.s.l.) – chemical composition, origins and organic aerosol sources, *Atmospheric Chemistry and Physics*, 15(19), 11373–11398, <https://doi.org/10.5194/acp-15-11373-2015>, 2015.
- Fry, J. L., Brown, S. S., Middlebrook, A. M., Edwards, P. M., Campuzano-Jost, P., Day, D. A., Jimenez, J. L., Allen, H. M., Ryerson, T. B., Pollack, I., Graus, M., Warneke, C., de Gouw, J. A., Brock, C. A., Gilman, J., Lerner, B. M., Dubé, W. P., Liao, J. and Welti, A.: Secondary organic aerosol (SOA) yields from NO<sub>3</sub> radical + isoprene based on nighttime aircraft power plant plume transects, *Atmospheric Chemistry and Physics*, 18(16), 11663–11682, <https://doi.org/10.5194/acp-18-11663-2018>, 2018.
- Gelaro, R., McCarty, W., Suárez, M. J., Todling, R., Molod, A., Takacs, L., Randles, C. A., Darmenov, A., Bosilovich, M. G., Reichle, R., Wargan, K., Coy, L., Cullather, R., Draper, C., Akella, S., Buchard, V., Conaty, A., da Silva, A. M., Gu, W., Kim, G.-K., Koster, R., Lucchesi, R., Merkova, D., Nielsen, J. E., Partyka, G., Pawson, S., Putman, W., Rienecker, M.,

- Schubert, S. D., Sienkiewicz, M. and Zhao, B.: The Modern-Era Retrospective Analysis for Research and Applications, Version 2 (MERRA-2), *J. Climate*, 30(14), 5419–5454, <https://doi.org/10.1175/JCLI-D-16-0758.1>, 2017.
- González, Y., Rodríguez, S., Guerra García, J. C., Trujillo, J. L. and García, R.: Ultrafine particles pollution in urban coastal air due to ship emissions, *Atmospheric Environment*, 45(28), 4907–4914, <https://doi.org/10.1016/j.atmosenv.2011.06.002>,  
1120 2011.
- Hama, S. M. L., Cordell, R. L. and Monks, P. S.: Quantifying primary and secondary source contributions to ultrafine particles in the UK urban background, *Atmospheric Environment*, 166, 62–78, <https://doi.org/10.1016/j.atmosenv.2017.07.013>, 2017a.
- Hama, S. M. L., Cordell, R. L., Kos, G. P. A., Weijers, E. P. and Monks, P. S.: Sub-micron particle number size distribution characteristics at two urban locations in Leicester, *Atmospheric Research*, 194, 1–16, <https://doi.org/10.1016/j.atmosres.2017.04.021>, 2017b.  
1125
- Healy, R. M., O'Connor, I. P., Hellebust, S., Allanic, A., Sodeau, J. R. and Wenger, J. C.: Characterisation of single particles from in-port ship emissions, *Atmospheric Environment*, 43(40), 6408–6414, <https://doi.org/10.1016/j.atmosenv.2009.07.039>, 2009.
- Henry, R., Norris, G. A., Vedantham, R. and Turner, J. R.: Source Region Identification Using Kernel Smoothing, *Environmental Science & Technology*, 43(11), 4090–4097, <https://doi.org/10.1021/es8011723>, 2009.  
1130
- Huffman, J. A., Docherty, K. S., Aiken, A. C., Cubison, M. J., Ulbrich, I. M., DeCarlo, P. F., Sueper, D., Jayne, J. T., Worsnop, D. R., Ziemann, P. J. and Jimenez, J. L.: Chemically-resolved aerosol volatility measurements from two megacity field studies, *Atmos. Chem. Phys.*, 22, 2009.
- Jayne, J. T., Leard, D. C., Zhang, X., Davidovits, P., Smith, K. A., Kolb, C. E. and Worsnop, D. R.: Development of an Aerosol Mass Spectrometer for Size and Composition Analysis of Submicron Particles, *Aerosol Science and Technology*, 33(1–2), 49–70, <https://doi.org/10.1080/027868200410840>, 2000.  
1135
- Kerminen, V.-M., Chen, X., Vakkari, V., Petäjä, T., Kulmala, M. and Bianchi, F.: Atmospheric new particle formation and growth: review of field observations, *Environmental Research Letters*, 13(10), 103003, <https://doi.org/10.1088/1748-9326/aadf3c>, 2018.  
1140
- Kiendler-Scharr, A., Mensah, A. A., Friese, E., Topping, D., Nemitz, E., Prevot, A. S. H., Äijälä, M., Allan, J., Canonaco, F., Canagaratna, M., Carbone, S., Crippa, M., Dall'Osto, M., Day, D. A., De Carlo, P., Di Marco, C. F., Elbern, H., Eriksson, A., Freney, E., Hao, L., Herrmann, H., Hildebrandt, L., Hillamo, R., Jimenez, J. L., Laaksonen, A., McFiggans, G., Mohr, C., O'Dowd, C., Otjes, R., Ovadnevaite, J., Pandis, S. N., Poulain, L., Schlag, P., Sellegri, K., Swietlicki, E., Tiitta, P., Vermeulen, A., Wahner, A., Worsnop, D. and Wu, H.-C.: Ubiquity of organic nitrates from nighttime chemistry in the European submicron aerosol: Organic Nitrates in European PM<sub>1</sub>, *Geophysical Research Letters*, 43(14), 7735–7744, <https://doi.org/10.1002/2016GL069239>, 2016.  
1145
- Kittelson, D. B.: ENGINES AND NANOPARTICLES: A REVIEW, , 14, 1998.

- 1150 Kreyling, W. G., Semmler-Behnke, M. and Möller, W.: Ultrafine Particle–Lung Interactions: Does Size Matter?, *Journal of Aerosol Medicine*, 19(1), 74–83, <https://doi.org/10.1089/jam.2006.19.74>, 2006.
- Kulmala, M., Luoma, K., Virkkula, A., Petäjä, T., Paasonen, P., Kerminen, V.-M., Nie, W., Qi, X., Shen, Y., Chi, X. and Ding, A.: On the mode-segregated aerosol particle number concentration load: contributions of primary and secondary particles in Hyytiälä and Nanjing, , 21, 13, 2016.
- 1155 Laborde, M., Crippa, M., Tritscher, T., Jurányi, Z., Decarlo, P. F., Temime-Roussel, B., Marchand, N., Eckhardt, S., Stohl, A., Baltensperger, U., Prévôt, A. S. H., Weingartner, E. and Gysel, M.: Black carbon physical properties and mixing state in the European megacity Paris, *Atmospheric Chemistry and Physics*, 13(11), 5831–5856, <https://doi.org/10.5194/acp-13-5831-2013>, 2013.
- Lack, D. A., Corbett, J. J., Onasch, T., Lerner, B., Massoli, P., Quinn, P. K., Bates, T. S., Covert, D. S., Coffman, D., Sierau, B., Herndon, S., Allan, J., Baynard, T., Lovejoy, E., Ravishankara, A. R. and Williams, E.: Particulate emissions from commercial shipping: Chemical, physical, and optical properties, *Journal of Geophysical Research*, 114, <https://doi.org/10.1029/2008JD011300>, 2009.
- 1160 Larssen, S., Sluyter, R. and Helmis, C.: Criteria for EUROAIRNET - The EEA Air Quality Monitoring and Information Network, , 56, 1999.
- Lelieveld, J., Evans, J. S., Fnais, M., Giannadaki, D. and Pozzer, A.: The contribution of outdoor air pollution sources to premature mortality on a global scale, *Nature*, 525(7569), 367–371, <https://doi.org/10.1038/nature15371>, 2015.
- 1165 Liakakou, E., Stavroulas, I., Kaskaoutis, D. G., Grivas, G., Paraskevopoulou, D., Dumka, U. C., Tsagkaraki, M., Bougiatioti, A., Oikonomou, K., Sciare, J., Gerasopoulos, E. and Mihalopoulos, N.: Long-term variability, source apportionment and spectral properties of black carbon at an urban background site in Athens, Greece, *Atmospheric Environment*, 222, 117137, <https://doi.org/10.1016/j.atmosenv.2019.117137>, 2020.
- 1170 Lianou, M., Chalbot, M.-C., Kavouras, I. G., Kotronarou, A., Karakatsani, A., Analytis, A., Katsouyanni, K., Puustinen, A., Hameri, K., Vallius, M., Pekkanen, J., Meddings, C., Harrison, R. M., Ayres, J. G., ten Brick, H., Kos, G., Meliefste, K., de Hartog, J. and Hoek, G.: Temporal variations of atmospheric aerosol in four European urban areas, *Environmental Science and Pollution Research*, 18(7), 1202–1212, <https://doi.org/10.1007/s11356-011-0471-y>, 2011.
- 1175 Mallet, M. D., D’Anna, B., Mème, A., Bove, M. C., Cassola, F., Pace, G., Desboeufs, K., Di Biagio, C., Doussin, J.-F., Maille, M., Massabò, D., Sciare, J., Zapf, P., di Sarra, A. G. and Formenti, P.: Summertime surface PM1 aerosol composition and size by source region at the Lampedusa island in the central Mediterranean Sea, *Atmospheric Chemistry and Physics*, 19(17), 11123–11142, <https://doi.org/10.5194/acp-19-11123-2019>, 2019.
- MedCruise: Statistics Cruise Activities in MedCruise Ports, statistics report, MedCruise Association, Puerto de Santa Cruz de Tenerife., 2018.
- 1180 Meng, W., Zhong, Q., Yun, X., Zhu, X., Huang, T., Shen, H., Chen, Y., Chen, H., Zhou, F., Liu, J., Wang, X., Zeng, E. Y. and Tao, S.: Improvement of a Global High-Resolution Ammonia Emission Inventory for Combustion and Industrial

- Sources with New Data from the Residential and Transportation Sectors, *Environ. Sci. Technol.*, 51(5), 2821–2829, <https://doi.org/10.1021/acs.est.6b03694>, 2017.
- Merico, E., Cesari, D., Dinoi, A., Gambaro, A., Barbaro, E., Guascito, M. R., Giannossa, L. C., Mangone, A. and Contini, D.: Inter-comparison of carbon content in PM10 and PM2.5 measured with two thermo-optical protocols on samples collected in a Mediterranean site, *Environmental Science and Pollution Research*, 26(28), 29334–29350, <https://doi.org/10.1007/s11356-019-06117-7>, 2019.
- Mestayer, P. G., Durand, P., Augustin, P., Bastin, S., Bonnefond, J.-M., Bénéch, B., Campistron, B., Coppalle, A., Delbarre, H., Dousset, B., Drobinski, P., Druilhet, A., Fréjafon, E., Grimmond, C. S. B., Groleau, D., Irvine, M., Kergomard, C., Kermadi, S., Lagouarde, J.-P., Lemonsu, A., Lohou, F., Long, N., Masson, V., Moppert, C., Noilhan, J., Offerle, B., Oke, T. R., Pigeon, G., Puygrenier, V., Roberts, S., Rosant, J.-M., Saïd, F., Salmond, J., Talbaut, M. and Voogt, J.: The urban boundary-layer field campaign in marseille (ubl/clu-escompte): set-up and first results, *Boundary-Layer Meteorology*, 114(2), 315–365, <https://doi.org/10.1007/s10546-004-9241-4>, 2005.
- Middlebrook, A. M., Bahreini, R., Jimenez, J. L. and Canagaratna, M. R.: Evaluation of Composition-Dependent Collection Efficiencies for the Aerodyne Aerosol Mass Spectrometer using Field Data, *Aerosol Science and Technology*, 46(3), 258–271, <https://doi.org/10.1080/02786826.2011.620041>, 2012.
- Minguillón, M. C., Perron, N., Querol, X., Szidat, S., Fahrni, S. M., Alastuey, A., Jimenez, J. L., Mohr, C., Ortega, A. M., Day, D. A., Lanz, V. A., Wacker, L., Reche, C., Cusack, M., Amato, F., Kiss, G., Hoffer, A., Decesari, S., Moretti, F., Hillamo, R., Teinilä, K., Seco, R., Peñuelas, J., Metzger, A., Schallhart, S., Müller, M., Hansel, A., Burkhardt, J. F., Baltensperger, U. and Prévôt, A. S. H.: Fossil versus contemporary sources of fine elemental and organic carbonaceous particulate matter during the DAURE campaign in Northeast Spain, *Atmospheric Chemistry and Physics*, 11(23), 12067–12084, <https://doi.org/10.5194/acp-11-12067-2011>, 2011.
- Minguillón, M. C., Ripoll, A., Pérez, N., Prévôt, A. S. H., Canonaco, F., Querol, X. and Alastuey, A.: Chemical characterization of submicron regional background aerosols in the western Mediterranean using an Aerosol Chemical Speciation Monitor, *Atmospheric Chemistry and Physics*, 15(11), 6379–6391, <https://doi.org/10.5194/acp-15-6379-2015>, 2015.
- Mohr, C., DeCarlo, P. F., Heringa, M. F., Chirico, R., Slowik, J. G., Richter, R., Reche, C., Alastuey, A., Querol, X., Seco, R., Peñuelas, J., Jiménez, J. L., Crippa, M., Zimmermann, R., Baltensperger, U. and Prévôt, A. S. H.: Identification and quantification of organic aerosol from cooking and other sources in Barcelona using aerosol mass spectrometer data, *Atmospheric Chemistry and Physics*, 12(4), 1649–1665, <https://doi.org/10.5194/acp-12-1649-2012>, 2012.
- Mousavi, A., Sowlat, M. H., Lovett, C., Rauber, M., Szidat, S., Boffi, R., Borgini, A., De Marco, C., Ruprecht, A. A. and Sioutas, C.: Source apportionment of black carbon (BC) from fossil fuel and biomass burning in metropolitan Milan, Italy, *Atmospheric Environment*, 203, 252–261, <https://doi.org/10.1016/j.atmosenv.2019.02.009>, 2019.
- Ng, N. L., Herndon, S. C., Trimborn, A., Canagaratna, M. R., Croteau, P. L., Onasch, T. B., Sueper, D., Worsnop, D. R., Zhang, Q., Sun, Y. L. and Jayne, J. T.: An Aerosol Chemical Speciation Monitor (ACSM) for Routine Monitoring of the

- Composition and Mass Concentrations of Ambient Aerosol, *Aerosol Science and Technology*, 45(7), 780–794, <https://doi.org/10.1080/02786826.2011.560211>, 2011.
- 1220 Nunes, R. A. O., Alvim-Ferraz, M. C. M., Martins, F. G., Calderay-Cayetano, F., Durán-Grados, V., Moreno-Gutiérrez, J., Jalkanen, J.-P., Hannuniemi, H. and Sousa, S. I. V.: Shipping emissions in the Iberian Peninsula and the impacts on air quality, *Atmos. Chem. Phys.*, 20(15), 9473–9489, <https://doi.org/10.5194/acp-20-9473-2020>, 2020.
- Olson, D. A., Vedantham, R., Norris, G. A., Brown, S. G. and Roberts, P.: Determining source impacts near roadways using wind regression and organic source markers, *Atmospheric Environment*, 47, 261–268, <https://doi.org/10.1016/j.atmosenv.2011.11.003>, 2012.
- 1225 Pandolfi, M., Mooibroek, D., Hopke, P., van Pinxteren, D., Querol, X., Herrmann, H., Alastuey, A., Favez, O., Hüglin, C., Perdrix, E., Riffault, V., Sauvage, S., van der Swaluw, E., Tarasova, O. and Colette, A.: Long-range and local air pollution: what can we learn from chemical speciation of particulate matter at paired sites?, *Atmospheric Chemistry and Physics*, 20(1), 409–429, <https://doi.org/10.5194/acp-20-409-2020>, 2020.
- 1230 Park, K., Chow, J. C., Watson, J. G., Trimble, D. L., Doraiswamy, P., Park, K., Arnott, W. P., Stroud, K. R., Bowers, K., Bode, R., Petzold, A. and Hansen, A. D. A.: Comparison of Continuous and Filter-Based Carbon Measurements at the Fresno Supersite, *Journal of the Air & Waste Management Association*, 56(4), 474–491, <https://doi.org/10.1080/10473289.2006.10464521>, 2006.
- Pascal, M., Corso, M., Chanel, O., Declercq, C., Badaloni, C., Cesaroni, G., Henschel, S., Meister, K., Haluza, D., Martin-Olmedo, P. and Medina, S.: Assessing the public health impacts of urban air pollution in 25 European cities: Results of the Aphekom project, *Science of The Total Environment*, 449, 390–400, <https://doi.org/10.1016/j.scitotenv.2013.01.077>, 2013.
- 1235 Pascal, M., Chanel, P. de C., Corso, M., Medina, S., Wagner, V., Gorla, S., Beaudeau, P., Bentayeb, M., Tertre, A. L., Ung, A., Chatignoux, E. and Quénel, P.: Impacts de l'exposition chronique aux particules fines sur la mortalité en France continentale et analyse des gains en santé de plusieurs scénarios de réduction de la pollution atmosphérique, , 162, 2016.
- 1240 Pauraitė, J., Pivoras, A., Plauškaitė, K., Byčėnkienė, S., Mordas, G., Augustaitis, A., Marozas, V., Mozgeris, G., Baumgarten, M., Matyssek, R. and Ulevicius, V.: Characterization of aerosol mass spectra responses to temperature over a forest site in Lithuania, *Journal of Aerosol Science*, 133, 56–65, <https://doi.org/10.1016/j.jaerosci.2019.03.010>, 2019.
- Petit, J.-E., Favez, O., Sciare, J., Crenn, V., Sarda-Estève, R., Bonnaire, N., Močnik, G., Dupont, J.-C., Haeffelin, M. and Leoz-Garziandia, E.: Two years of near real-time chemical composition of submicron aerosols in the region of Paris using an Aerosol Chemical Speciation Monitor (ACSM) and a multi-wavelength Aethalometer, *Atmospheric Chemistry and Physics*, 15(6), 2985–3005, <https://doi.org/10.5194/acp-15-2985-2015>, 2015.
- 1245 Petit, J.-E., Favez, O., Albinet, A. and Canonaco, F.: A user-friendly tool for comprehensive evaluation of the geographical origins of atmospheric pollution: Wind and trajectory analyses, *Environmental Modelling & Software*, 88, 183–187, <https://doi.org/10.1016/j.envsoft.2016.11.022>, 2017a.
- Petit, J.-E., Amodeo, T., Meleux, F., Bessagnet, B., Menut, L., Grenier, D., Pellan, Y., Ockler, A., Rocq, B., Gros, V., Sciare, J. and Favez, O.: Characterising an intense PM pollution episode in March 2015 in France from multi-site approach and near

- 1250 real time data: Climatology, variabilities, geographical origins and model evaluation, *Atmospheric Environment*, 155, 68–84, <https://doi.org/10.1016/j.atmosenv.2017.02.012>, 2017b.
- Pieber, S. M., El Haddad, I., Slowik, J. G., Canagaratna, M. R., Jayne, J. T., Platt, S. M., Bozzetti, C., Daellenbach, K. R., Fröhlich, R., Vlachou, A., Klein, F., Dommen, J., Miljevic, B., Jiménez, J. L., Worsnop, D. R., Baltensperger, U. and Prévôt, A. S. H.: Inorganic Salt Interference on CO<sub>2</sub>+ in Aerodyne AMS and ACSM Organic Aerosol Composition Studies, *Environmental Science & Technology*, 50(19), 10494–10503, <https://doi.org/10.1021/acs.est.6b01035>, 2016.
- 1255 Poulain, L., Spindler, G., Birmili, W., Plass-Dülmer, C., Wiedensohler, A. and Herrmann, H.: Seasonal and diurnal variations of particulate nitrate and organic matter at the IFT research station Melpitz, *Atmospheric Chemistry and Physics*, 11(24), 12579–12599, <https://doi.org/10.5194/acp-11-12579-2011>, 2011.
- Poulain, L., Birmili, W., Canonaco, F., Crippa, M., Wu, Z. J., Nordmann, S., Spindler, G., Prévôt, A. S. H., Wiedensohler, A. and Herrmann, H.: Chemical mass balance of 300 °C non-volatile particles at the tropospheric research site Melpitz, Germany, *Atmospheric Chemistry and Physics*, 14(18), 10145–10162, <https://doi.org/10.5194/acp-14-10145-2014>, 2014.
- 1260 Puygrenier, V., Lohou, F., Campistron, B., Saïd, F., Pigeon, G., Bénéch, B. and Serça, D.: Investigation on the fine structure of sea-breeze during ESCOMPTE experiment, *Atmospheric Research*, 74(1–4), 329–353, <https://doi.org/10.1016/j.atmosres.2004.06.011>, 2005.
- 1265 Ramanantenasoa, M. M. J., Gilliot, J.-M., Mignolet, C., Bedos, C., Mathias, E., Eglin, T., Makowski, D. and Générumont, S.: A new framework to estimate spatio-temporal ammonia emissions due to nitrogen fertilization in France, *Science of The Total Environment*, 645, 205–219, <https://doi.org/10.1016/j.scitotenv.2018.06.202>, 2018.
- Reche, C., Querol, X., Alastuey, A., Viana, M., Pey, J., Moreno, T., Rodríguez, S., González, Y., Fernández-Camacho, R., de la Rosa, J., Dall&apos;Osto, M., Prévôt, A. S. H., Hueglin, C., Harrison, R. M. and Quincey, P.: New considerations for PM, Black Carbon and particle number concentration for air quality monitoring across different European cities, *Atmospheric Chemistry and Physics*, 11(13), 6207–6227, <https://doi.org/10.5194/acp-11-6207-2011>, 2011.
- 1270 Reyes-Villegas, E., Green, D. C., Priestman, M., Canonaco, F., Coe, H., Prévôt, A. S. H. and Allan, J. D.: Organic aerosol source apportionment in London 2013 with ME-2: exploring the solution space with annual and seasonal analysis, *Atmospheric Chemistry and Physics*, 16(24), 15545–15559, <https://doi.org/10.5194/acp-16-15545-2016>, 2016.
- 1275 Ripoll, A., Minguillón, M. C., Pey, J., Jimenez, J. L., Day, D. A., Sosedova, Y., Canonaco, F., Prévôt, A. S. H., Querol, X. and Alastuey, A.: Long-term real-time chemical characterization of submicron aerosols at Montsec (southern Pyrenees, 1570 m a.s.l.), *Atmospheric Chemistry and Physics*, 15(6), 2935–2951, <https://doi.org/10.5194/acp-15-2935-2015>, 2015.
- Rodríguez, S. and Cuevas, E.: The contributions of “minimum primary emissions” and “new particle formation enhancements” to the particle number concentration in urban air, *Journal of Aerosol Science*, 38(12), 1207–1219, <https://doi.org/10.1016/j.jaerosci.2007.09.001>, 2007.
- 1280 Rouaud, P. and Channac, Y.: Pollution de l’air par les PM10 En 2017, le seuil de l’OMS dépassé pour la moitié des résidents de la région, INSEE Analyses, INSEE, Marseille. <https://www.insee.fr/fr/statistiques/4250618?sommaire=4251028>, 2019.

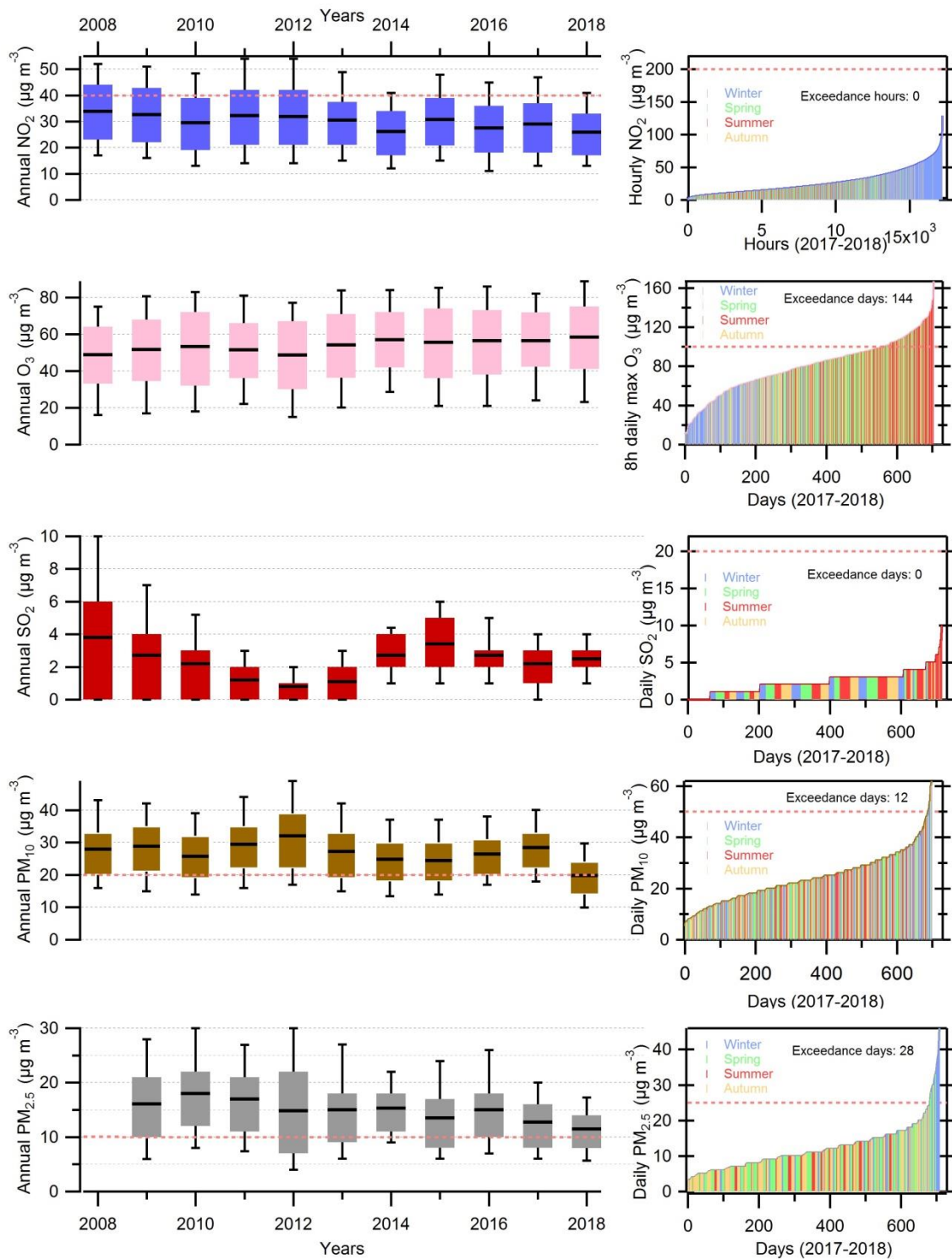
- Saarikoski, S., Carbone, S., Decesari, S., Giulianelli, L., Angelini, F., Canagaratna, M., Ng, N. L., Trimborn, A., Facchini, M. C., Fuzzi, S., Hillamo, R. and Worsnop, D.: Chemical characterization of springtime submicrometer aerosol in Po Valley, Italy, *Atmospheric Chemistry and Physics*, 12(18), 8401–8421, <https://doi.org/10.5194/acp-12-8401-2012>, 2012.
- 1285 Salameh, D., Detournay, A., Pey, J., Pérez, N., Liguori, F., Saraga, D., Bove, M. C., Brotto, P., Cassola, F., Massabò, D., Latella, A., Pillon, S., Formenton, G., Patti, S., Armengaud, A., Piga, D., Jaffrezo, J. L., Bartzis, J., Tolis, E., Prati, P., Querol, X., Wortham, H. and Marchand, N.: PM<sub>2.5</sub> chemical composition in five European Mediterranean cities: A 1-year study, *Atmospheric Research*, 155, 102–117, <https://doi.org/10.1016/j.atmosres.2014.12.001>, 2015.
- 1290 Salameh, D., Pey, J., Bozzetti, C., El Haddad, I., Detournay, A., Sylvestre, A., Canonaco, F., Armengaud, A., Piga, D., Robin, D., Prevot, A. S. H., Jaffrezo, J.-L., Wortham, H. and Marchand, N.: Sources of PM<sub>2.5</sub> at an urban-industrial Mediterranean city, Marseille (France): Application of the ME-2 solver to inorganic and organic markers, *Atmospheric Research*, 214, 263–274, <https://doi.org/10.1016/j.atmosres.2018.08.005>, 2018.
- Salcedo, D., Onasch, T. B., Dzepina, K., Canagaratna, M. R., Zhang, Q., Huffman, J. A., DeCarlo, P. F., Jayne, J. T., Mortimer, P., Worsnop, D. R., Kolb, C. E., Johnson, K. S., Zuberi, B., Marr, L. C., Volkamer, R., Molina, L. T., Molina, M. J., Cardenas, B., Bernabé, R. M., Márquez, C., Gaffney, J. S., Marley, N. A., Laskin, A., Shutthanandan, V., Xie, Y., Brune, W., Leshner, R., Shirley, T. and Jimenez, J. L.: Characterization of ambient aerosols in Mexico City during the MCMA-2003 campaign with Aerosol Mass Spectrometry: results from the CENICA Supersite, *Atmospheric Chemistry and Physics*, 6(4), 925–946, <https://doi.org/10.5194/acp-6-925-2006>, 2006.
- 1295 Sandradewi, J., Prévôt, A. S. H., Szidat, S., Perron, N., Alfarra, M. R., Lanz, V. A., Weingartner, E. and Baltensperger, U.: Using Aerosol Light Absorption Measurements for the Quantitative Determination of Wood Burning and Traffic Emission Contributions to Particulate Matter, *Environmental Science & Technology*, 42(9), 3316–3323, <https://doi.org/10.1021/es702253m>, 2008.
- 1305 Schaap, M., Spindler, G., Schulz, M., Acker, K., Maenhaut, W., Berner, A., Wieprecht, W., Streit, N., Müller, K., Brüggemann, E., Chi, X., Putaud, J.-P., Hitzenberger, R., Puxbaum, H., Baltensperger, U. and ten Brink, H.: Artefacts in the sampling of nitrate studied in the “INTERCOMP” campaigns of EUROTRAC-AEROSOL, *Atmospheric Environment*, 38(38), 6487–6496, <https://doi.org/10.1016/j.atmosenv.2004.08.026>, 2004a.
- Schaap, M., van Loon, M., ten Brink, H. M., Dentener, F. J. and Builtjes, P. J. H.: Secondary inorganic aerosol simulations for Europe with special attention to nitrate, *Atmospheric Chemistry and Physics*, 4(3), 857–874, [https://doi.org/10.5194/acp-](https://doi.org/10.5194/acp-4-857-2004)
- 1310 4-857-2004, 2004b.
- Sciare, J., Sarda-Estève, R., Favez, O., Cachier, H., Aymoz, G. and Laj, P.: Nighttime residential wood burning evidenced from an indirect method for estimating real-time concentration of particulate organic matter (POM), *Atmospheric Environment*, 42(9), 2158–2172, <https://doi.org/10.1016/j.atmosenv.2007.11.053>, 2008.
- Seinfeld and Pandis, J. H., Spyros N.: *Atmospheric Chemistry and Physics*, 2016.

- 1315 Squizzato, S., Masiol, M., Brunelli, A., Pistollato, S., Tarabotti, E., Rampazzo, G. and Pavoni, B.: Factors determining the formation of secondary inorganic aerosol: a case study in the Po Valley (Italy), *Atmospheric Chemistry and Physics*, 13(4), 1927–1939, <https://doi.org/10.5194/acp-13-1927-2013>, 2013.
- Stavroulas, I., Bougiatioti, A., Grivas, G., Paraskevopoulou, D., Tsagkaraki, M., Zampas, P., Liakakou, E., Gerasopoulos, E. and Mihalopoulos, N.: Sources and processes that control the submicron organic aerosol composition in an urban  
1320 Mediterranean environment (Athens): a high temporal-resolution chemical composition measurement study, *Atmospheric Chemistry and Physics*, 19(2), 901–919, <https://doi.org/10.5194/acp-19-901-2019>, 2019.
- Stelson, A. W. and Seinfeld, J. H.: Relative humidity and temperature dependence of the ammonium nitrate dissociation constant, , 16(Issue 5), 983–992, 1982.
- Suarez-Bertoa, R., Zardini, A. A., Lilova, V., Meyer, D., Nakatani, S., Hibel, F., Ewers, J., Clairotte, M., Hill, L. and  
1325 Astorga, C.: Intercomparison of real-time tailpipe ammonia measurements from vehicles tested over the new world-harmonized light-duty vehicle test cycle (WLTC), *Environmental Science and Pollution Research*, 22(10), 7450–7460, <https://doi.org/10.1007/s11356-015-4267-3>, 2015.
- Sun, K., Tao, L., Miller, D. J., Pan, D., Golston, L. M., Zondlo, M. A., Griffin, R. J., Wallace, H. W., Leong, Y. J., Yang, M. M., Zhang, Y., Mauzerall, D. L. and Zhu, T.: Vehicle Emissions as an Important Urban Ammonia Source in the United  
1330 States and China, *Environ. Sci. Technol.*, 51(4), 2472–2481, <https://doi.org/10.1021/acs.est.6b02805>, 2017.
- Sutton, M. A., Reis, S., Riddick, S. N., Dragosits, U., Nemitz, E., Theobald, M. R., Tang, Y. S., Braban, C. F., Vieno, M., Dore, A. J., Mitchell, R. F., Wanless, S., Daunt, F., Fowler, D., Blackall, T. D., Milford, C., Flechard, C. R., Loubet, B., Massad, R., Cellier, P., Personne, E., Coheur, P. F., Clarisse, L., Van Damme, M., Ngadi, Y., Clerbaux, C., Skjøth, C. A., Geels, C., Hertel, O., Wichink Kruit, R. J., Pinder, R. W., Bash, J. O., Walker, J. T., Simpson, D., Horváth, L., Misselbrook,  
1335 T. H., Bleeker, A., Dentener, F. and de Vries, W.: Towards a climate-dependent paradigm of ammonia emission and deposition, *Phil. Trans. R. Soc. B*, 368(1621), 20130166, <https://doi.org/10.1098/rstb.2013.0166>, 2013.
- Timonen, H., Cubison, M., Aurela, M., Brus, D., Lihavainen, H., Hillamo, R., Canagaratna, M., Nekat, B., Weller, R., Worsnop, D. and Saarikoski, S.: Applications and limitations of constrained high-resolution peak fitting on low resolving power mass spectra from the ToF-ACSM, *Atmospheric Measurement Techniques*, 9(7), 3263–3281,  
1340 <https://doi.org/10.5194/amt-9-3263-2016>, 2016.
- Tobías, A., Rivas, I., Reche, C., Alastuey, A., Rodríguez, S., Fernández-Camacho, R., Sánchez de la Campa, A. M., de la Rosa, J., Sunyer, J. and Querol, X.: Short-term effects of ultrafine particles on daily mortality by primary vehicle exhaust versus secondary origin in three Spanish cities, *Environment International*, 111, 144–151, <https://doi.org/10.1016/j.envint.2017.11.015>, 2018.
- 1345 TOMTOM: Traffic Index for urban congestion worldwide, [https://www.tomtom.com/en\\_gb/traffic-index/ranking/](https://www.tomtom.com/en_gb/traffic-index/ranking/), 2020.
- Turpin, B. J. and Lim, H.-J.: Species Contributions to PM<sub>2.5</sub> Mass Concentrations: Revisiting Common Assumptions for Estimating Organic Mass, *Aerosol Science and Technology*, 35(1), 602–610, <https://doi.org/10.1080/02786820119445>, 2001.

- Via, M., Minguillón, M. C., Reche, C., Querol, X. and Alastuey, A.: Increase of secondary organic aerosol over four years in an urban environment, preprint, *Aerosols/Field Measurements/Troposphere/Chemistry (chemical composition and reactions)*, 2020.
- Waked, A., Favez, O., Alleman, L. Y., Piot, C., Petit, J.-E., Delaunay, T., Verlinden, E., Golly, B., Besombes, J.-L., Jaffrezo, J.-L. and Leoz-Garziandia, E.: Source apportionment of PM<sub>10</sub> in a north-western Europe regional urban background site (Lens, France) using positive matrix factorization and including primary biogenic emissions, *Atmospheric Chemistry and Physics*, 14(7), 3325–3346, <https://doi.org/10.5194/acp-14-3325-2014>, 2014.
- Wehner, B. and Wiedensohler, A.: Long term measurements of submicrometer urban aerosols: statistical analysis for correlations with meteorological conditions and trace gases, *Atmos. Chem. Phys.*, 14, 2003.
- WHO: WHO Air quality guidelines for particulate matter, ozone, nitrogen dioxide and sulfur dioxide, Summary of risk assessment., 2006.
- Woo, K. S., Chen, D. R., Pui, D. Y. H. and McMurry, P. H.: Measurement of Atlanta Aerosol Size Distributions: Observations of Ultrafine Particle Events, *Aerosol Science and Technology*, 34(1), 75–87, <https://doi.org/10.1080/02786820120056>, 2001.
- Xu, L., Suresh, S., Guo, H., Weber, R. J. and Ng, N. L.: Aerosol characterization over the southeastern United States using high-resolution aerosol mass spectrometry: spatial and seasonal variation of aerosol composition and sources with a focus on organic nitrates, *Atmospheric Chemistry and Physics*, 15(13), 7307–7336, <https://doi.org/10.5194/acp-15-7307-2015>, 2015.
- Xu, W., Lambe, A., Silva, P., Hu, W., Onasch, T., Williams, L., Croteau, P., Zhang, X., Renbaum-Wolff, L., Fortner, E., Jimenez, J. L., Jayne, J., Worsnop, D. and Canagaratna, M.: Laboratory evaluation of species-dependent relative ionization efficiencies in the Aerodyne Aerosol Mass Spectrometer, *Aerosol Science and Technology*, 52(6), 626–641, <https://doi.org/10.1080/02786826.2018.1439570>, 2018.
- Young, D. E., Allan, J. D., Williams, P. I., Green, D. C., Flynn, M. J., Harrison, R. M., Yin, J., Gallagher, M. W. and Coe, H.: Investigating the annual behaviour of submicron secondary inorganic and organic aerosols in London, *Atmospheric Chemistry and Physics*, 15(11), 6351–6366, <https://doi.org/10.5194/acp-15-6351-2015>, 2015.
- Zhang, Q., Alfarra, M. R., Worsnop, D. R., Allan, J. D., Coe, H., Canagaratna, M. R. and Jimenez, J. L.: Deconvolution and Quantification of Hydrocarbon-like and Oxygenated Organic Aerosols Based on Aerosol Mass Spectrometry, *Environmental Science & Technology*, 39(13), 4938–4952, <https://doi.org/10.1021/es048568l>, 2005.
- Zhang, Q., Jimenez, J. L., Worsnop, D. R. and Canagaratna, M.: A Case Study of Urban Particle Acidity and Its Influence on Secondary Organic Aerosol, *Environmental Science & Technology*, 41(9), 3213–3219, <https://doi.org/10.1021/es061812j>, 2007.

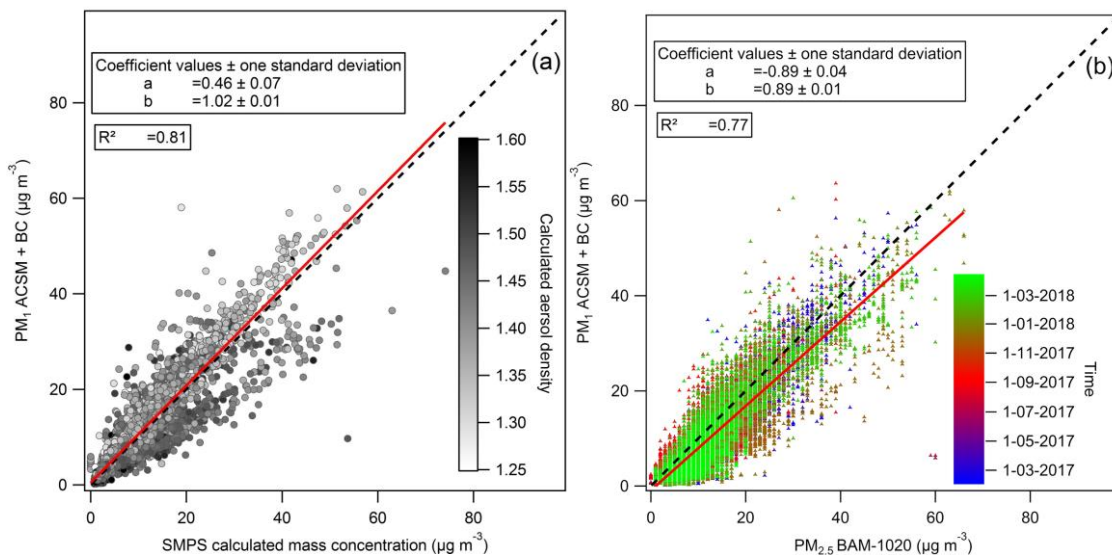
1380



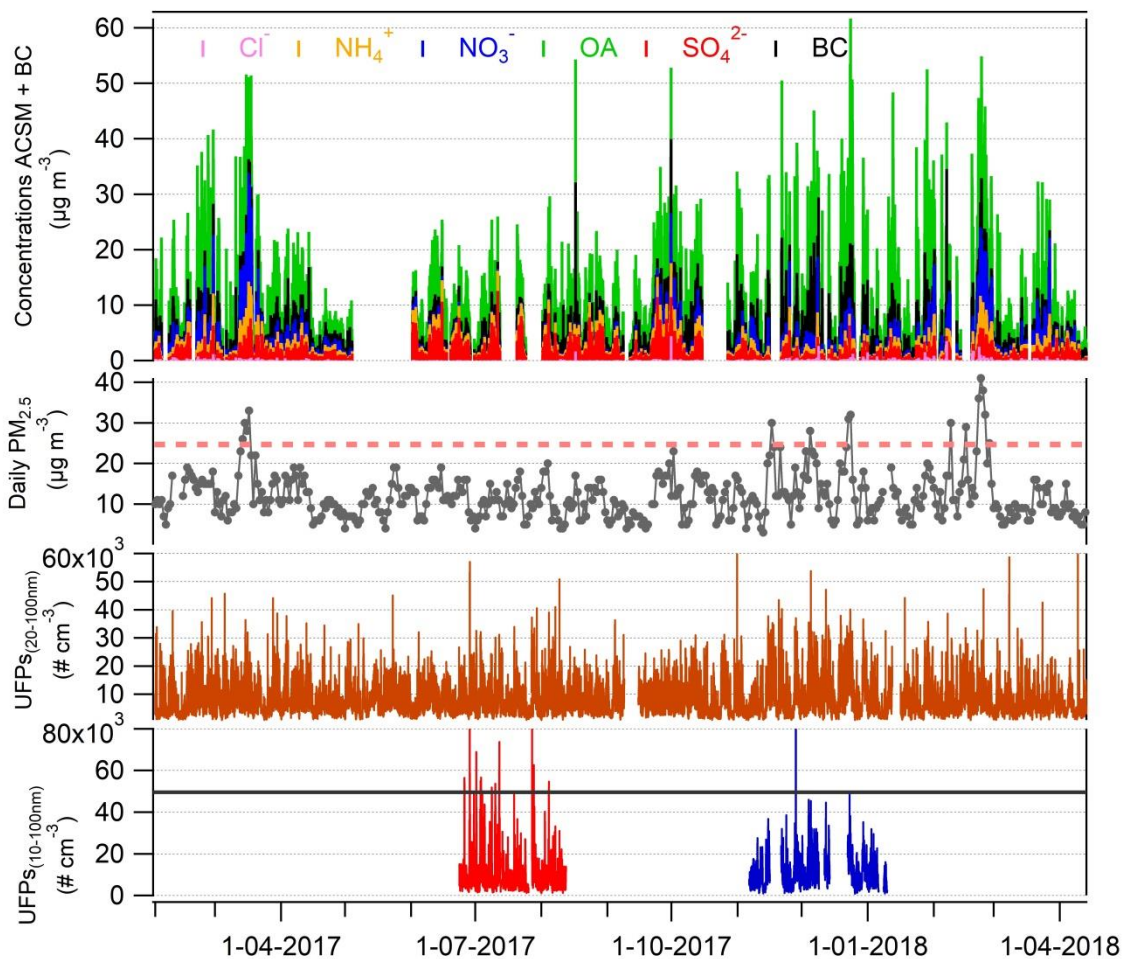
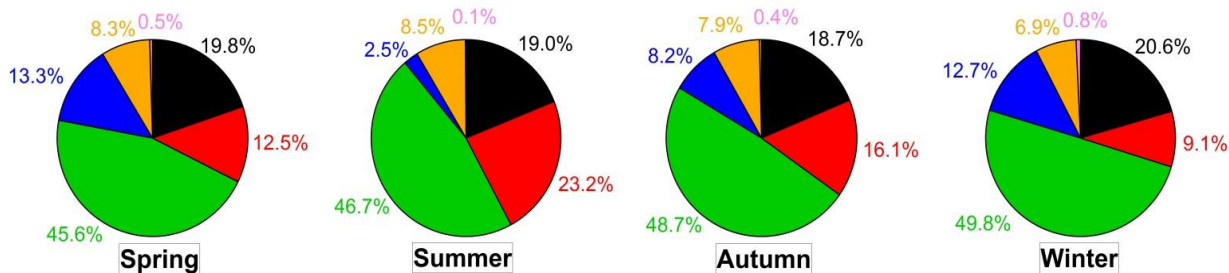


1390 **Figure 1: Graphs at left show annual average concentrations of the following pollutants during the last 11 years in Marseille-Longchamp: Nitrogen dioxide (Blue), Ozone (pink), sulphur dioxide (red), PM<sub>10</sub> (brown) and PM<sub>2.5</sub> (grey). The slopes of NO<sub>x</sub>, O<sub>3</sub>, PM<sub>10</sub> and PM<sub>2.5</sub> trends were estimated by the Sen-Theil method and their significance was evaluated through the non-parametric Mann-Kendall test. The red dotted thresholds correspond to the annual concentrations recommended by WHO (World Health Organisation) for Nitrogen dioxide, PM<sub>10</sub> and PM<sub>2.5</sub>. Graphs at right show data sorted by increasing daily values together with the number of days in excess according to the WHO recommendations (again the red dotted lines) for the years 2017 and 2018. For ozone, it corresponds to the daily maximum 8h average. Sticks for daily values are color-coded depending on the seasons (winter = blue; spring = green; summer = red; autumn = orange).**

1395



1400 **Figure 2: Reconstructed PM<sub>1</sub> (ACSM + BC) vs PM<sub>1</sub> calculated from SMPS measurements, with the color-coded density evaluated from the PM<sub>1</sub> chemical composition (a) and reconstructed PM<sub>1</sub> vs PM<sub>2.5</sub> measurements by BAM-1020, coloured according to the sampling time (d-mm-yyyy) (b). Red lines correspond to orthogonal distance fits and black dashed lines to 1:1 lines. R<sup>2</sup> are determined with least square fits.**



1405

Figure 3: Time series of 1h-PM<sub>1</sub> chemical species (Cl<sup>-</sup>, OA, NH<sub>4</sub><sup>+</sup>, NO<sub>3</sub><sup>-</sup>, SO<sub>4</sub><sup>2-</sup> and BC), daily-PM<sub>2.5</sub>, total UFPs (20-100nm) measured with 3031 and total UFPs (10-100nm) measured with SMPS GRIMM (summer period in red and winter period in blue) from 1 February 2017 to 13 April 2018. The average particle number concentrations were higher in winter however sharp events exceeding 50 000 cm<sup>-3</sup> (black line) were more abundant in summer period. This feature is traceable for the 10-100 nm size range measured with the SMPS GRIMM. The pink dotted thresholds correspond to the daily PM<sub>2.5</sub> concentrations recommended by WHO. Pie charts of average PM<sub>1</sub> components contribution for each season are showed on the upper panel.

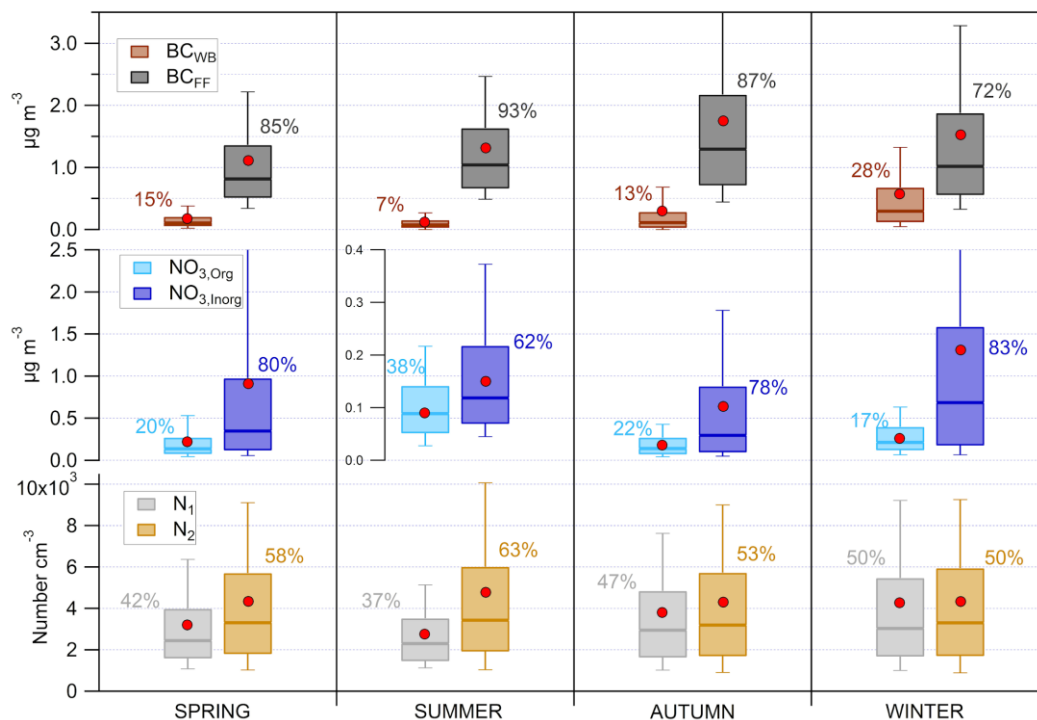
1410

	Unit	SPRING (March-April-May)		SUMMER (June-July-August)		AUTUMN (September-October-November)		WINTER (December-January-February)	
		Average	SD	Average	SD	Average	SD	Average	SD
OA	$\mu\text{g m}^{-3}$	3.86	3.37	4.55	2.66	5.07	3.78	6.17	5.69
BC	$\mu\text{g m}^{-3}$	1.30	1.17	1.49	1.16	1.90	1.74	2.12	2.27
SO <sub>4</sub> <sup>2-</sup>	$\mu\text{g m}^{-3}$	1.06	0.84	2.26	1.66	1.57	1.50	1.12	0.99
NO <sub>3</sub> <sup>-</sup>	$\mu\text{g m}^{-3}$	1.13	2.08	0.24	0.23	0.83	1.09	1.58	2.13
NH <sub>4</sub> <sup>+</sup>	$\mu\text{g m}^{-3}$	0.70	0.85	0.83	0.59	0.77	0.77	0.86	0.93
Cl <sup>-</sup>	$\mu\text{g m}^{-3}$	0.04	0.08	0.01	0.04	0.04	0.11	0.09	0.18
PM <sub>1</sub>	$\mu\text{g m}^{-3}$	8.09	6.99	9.39	4.77	10.2	7.26	11.9	9.79
f60	%	0.5	0.8	0.3	0.2	0.4	0.6	0.8	1.4
f44	%	10.1	11.9	13.0	10.5	14.2	14.2	10.5	13.0
f57	%	2.3	3.5	1.8	1.9	2.0	2.5	2.4	3.4
BC <sub>WB</sub>	$\mu\text{g m}^{-3}$	0.19	0.25	0.11	0.14	0.24	0.46	0.59	0.89
BC <sub>FF</sub>	$\mu\text{g m}^{-3}$	1.10	1.04	1.38	1.10	1.66	1.53	1.52	1.78
NO <sub>3,Org</sub>	$\mu\text{g m}^{-3}$	0.22	0.32	0.09	0.08	0.18	0.17	0.26	0.26
NO <sub>3,Inorg</sub>	$\mu\text{g m}^{-3}$	0.91	1.80	0.15	0.18	0.64	0.94	1.31	1.95
N <sub>1 (20-100nm)</sub>	N cm <sup>-3</sup>	3200	2531	2756	1736	3804	3212	4268	3916
N <sub>2 (20-100nm)</sub>	N cm <sup>-3</sup>	4339	3755	4777	4552	4301	3958	4332	3641

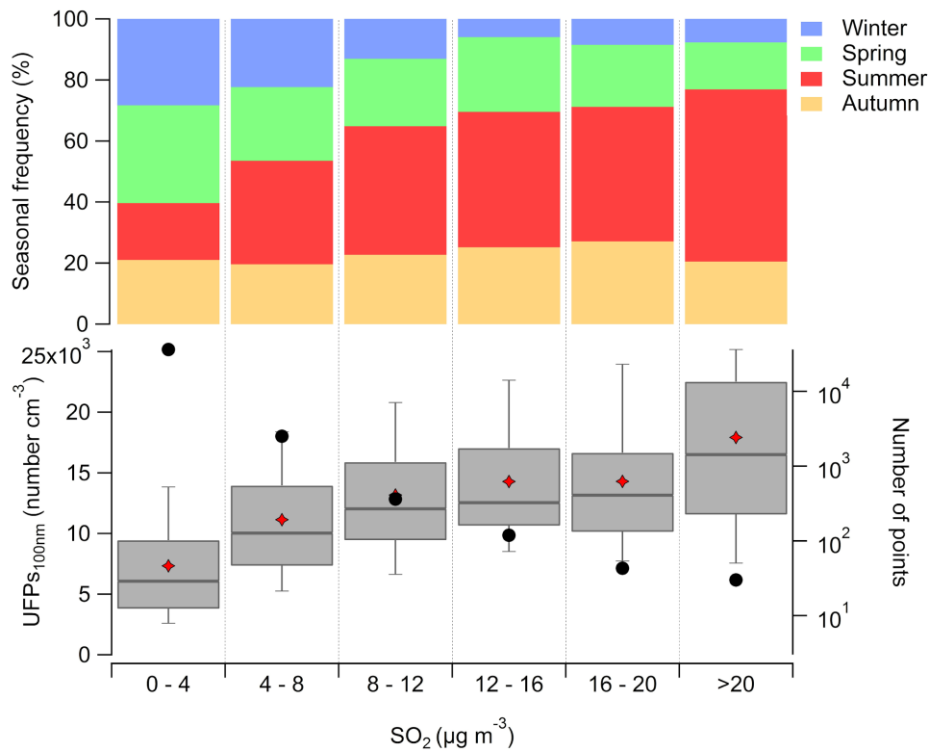
1415

**Table 1: Seasonal average concentrations and associated standard deviation (SD) of main chemical species of submicron aerosol and specific organic fragments for the study period. Average concentrations and SD of BC, nitrate, and particles number (20-100 nm) components are also represented.**

1420



1425 **Figure 4:** Seasonal concentrations for the different fractions of BC ( $BC_{WB}$  and  $BC_{FF}$ ),  $NO_3^-$  ( $NO_{3,Org}$ ,  $NO_{3,Inorg}$ ), and UFPs number between 20 and 100nm ( $N_1$ ,  $N_2$ ) represented as box plots. The band inside the box is the median (50<sup>th</sup> percentile), the bottom and top of the box represent the lower and upper quartiles respectively (the 25<sup>th</sup> and the 75<sup>th</sup> percentile). The ends of the whiskers denote here the 10<sup>th</sup> and 90<sup>th</sup> percentile. The red dots refer to the mean of each component.



1430

**Figure 5: Box plots of UFPs<sub><100nm</sub> number for different SO<sub>2</sub> concentrations bins (bottom) and seasonal occurrence frequency for each bin (top). The red diamonds are the mean, the bands inside the box are the median, the bottom and top of the box represent the lower and upper quartiles respectively and the ends of the whiskers show the 10<sup>th</sup> and 90<sup>th</sup> percentile. The black circles denote the number of data points (15-min resolution) encountered in each bin.**

1435

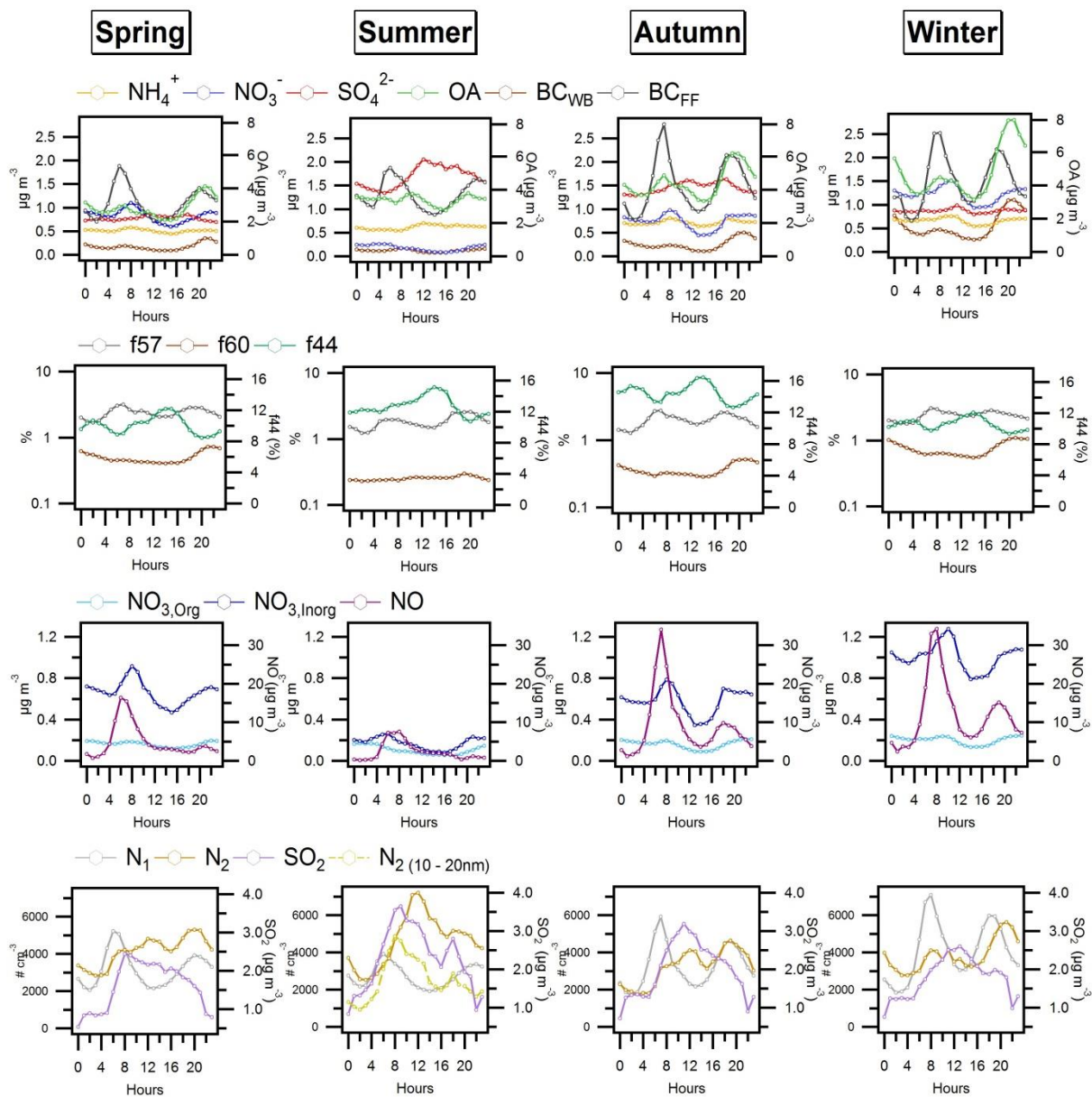


Figure 6: Seasonal diurnal profiles of PM<sub>1</sub> species, specific fractions of organic fragments (f60, f44 and f57), nitrate components (NO<sub>3,Org</sub>, NO<sub>3,Inorg</sub>) and NO, and UFPs components (N<sub>1</sub>, N<sub>2</sub>) and SO<sub>2</sub>. Note that left axis for f60 and f57 values is on logarithm scale for clarity reasons. For summer, secondary number of particles N<sub>2</sub> was also calculated for N between 10 and 20 nm from SMPS GRIMM measurements during the 23 June-12 August 2017 period (yellow dashed-line).

1440

	2008	2009	2010	2011	2012	2013	2014	2015	2016	2017	2018
<b>Winter</b>	-	12	19	29	31	35	4	17	18	11	12
<b>Spring</b>	-	10	16	11	16	5	11	8	3	4	0
<b>Summer</b>	0	13	19	3	1	4	1	0	2	0	0
<b>Autumn</b>	-	15	7	14	3	3	4	6	5	1	0
<b>Year</b>	-	50	61	57	51	47	20	31	28	16	12

1445

**Table 2: Number of days exceeding 25  $\mu\text{g m}^{-3}$  for  $\text{PM}_{2.5}$  concentrations (WHO recommendation) since they are measured in MRS-LCP. Results are presented by season and for the total years.**

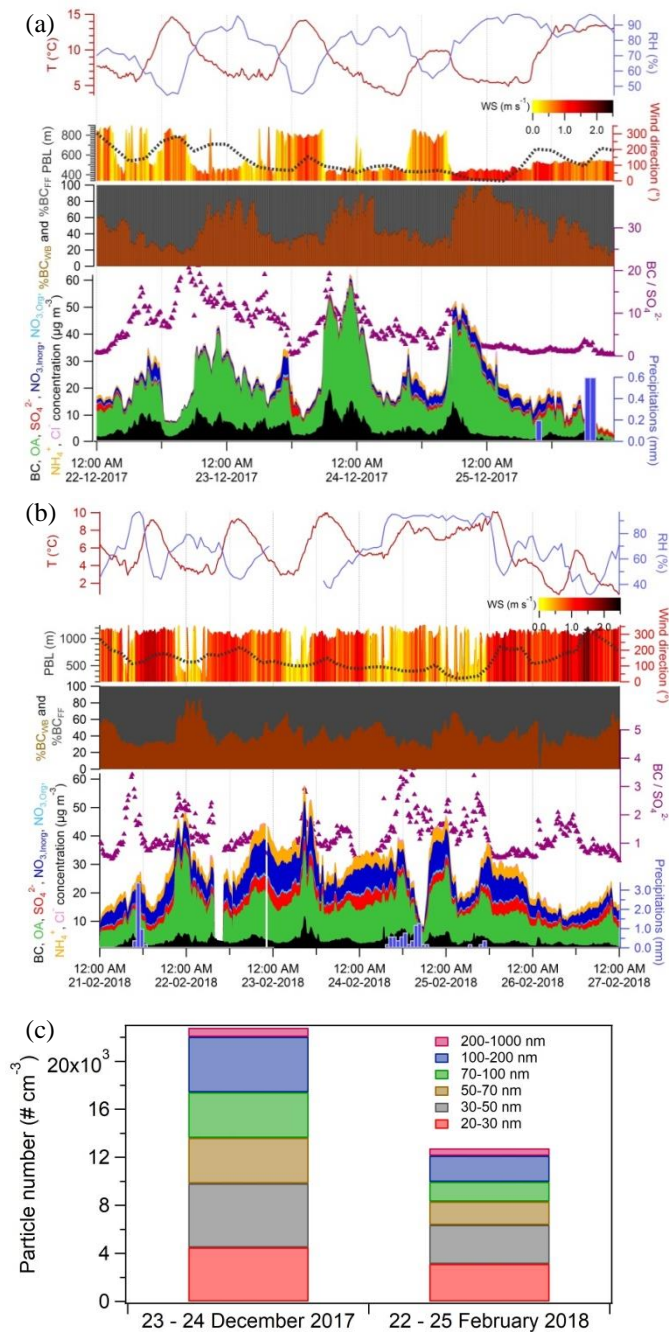
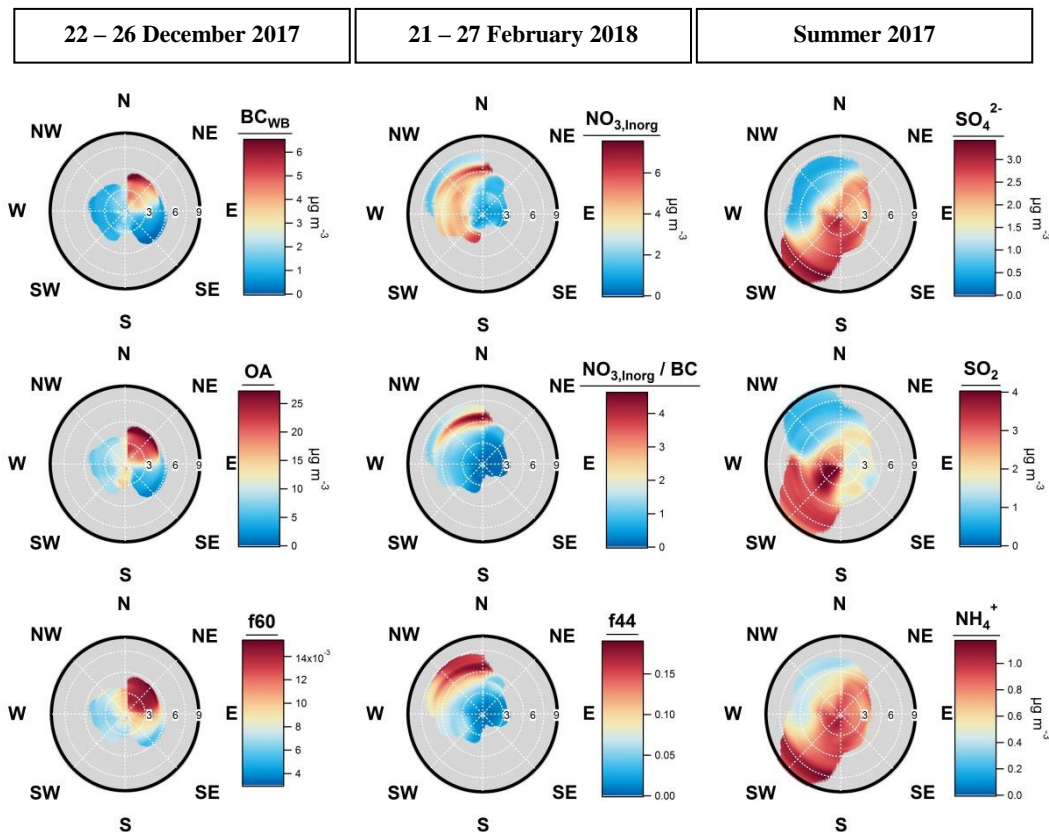


**Figure 7: Time series of meteorological conditions and chemical composition during the two polluted episodes: the local Christmas event (23-24 December 2017) (a) and the long-range event (22-25 February 2018) (b). The chemical composition of submicron particles (Cl<sup>-</sup>, NH<sub>4</sub><sup>+</sup>, NO<sub>3</sub>, SO<sub>4</sub><sup>2-</sup>, OA and BC); the relative contribution of BC<sub>FF</sub> and BC<sub>WB</sub>; the BC/SO<sub>4</sub><sup>2-</sup> ratio; and the meteorological data (temperature, relative humidity, wind direction and speed, planetary boundary layer and precipitations) are**

represented. The size contributions of total particle number during the two events (measured with the TSI 3031) are also shown (c).

1455



1460

Figure 8: NWR plots for the local Christmas event, SWIM-2 plots for the long-range episode and NWR plots for the summer period.  $BC_{WB}$  concentrations, OA concentrations and fraction of the m/z 60 ACSM organic signal are represented for the local Christmas event from 22 to 26 December 2017.  $NO_{3,Inorg}$  concentrations,  $NO_{3,Inorg}$  normalized by BC and fraction of the m/z 44 ACSM organic signal are displayed for the long-range influence from 21 to 27 February 2018. The SWIM-2 analysis was performed using a rolling standard deviation over 2 hours of wind measurements. The time periods for the events is extended to better catch the variability.  $SO_4^{2-}$ ,  $SO_2$  and  $NH_4^+$  concentrations are represented for the summer 2017. Radial and tangential axes show respectively the wind speed ( $km \cdot h^{-1}$ ) and the wind direction ( $^\circ$ ).

1465

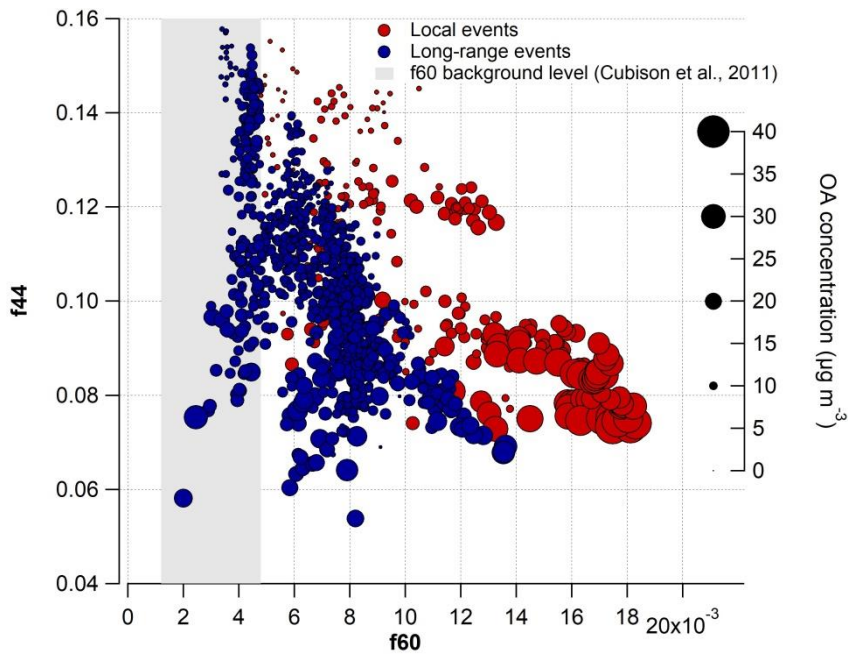


Figure 9: f44 vs f60 ratios during the local events (dark red circles) and the long-range events (dark blue circles). The size of markers is proportional to the OA concentration. The grey area represents the f60 background level defined by Cubison et al. (2011) ( $0.003 \pm 3$  times the standard deviation).

1470

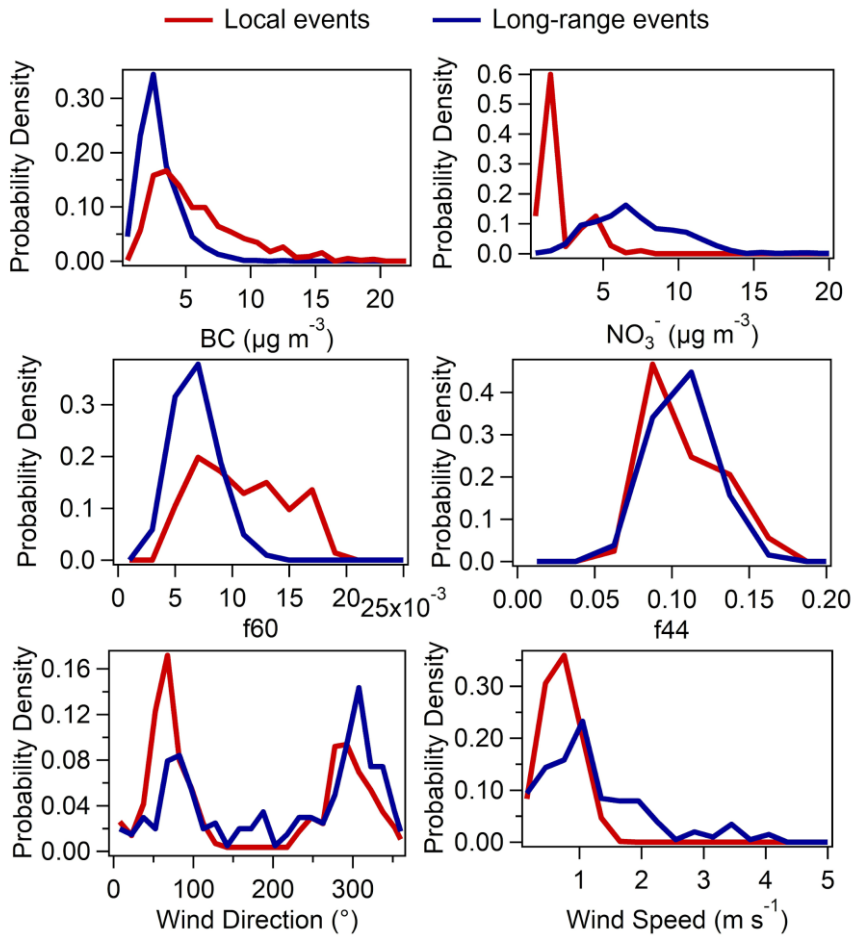
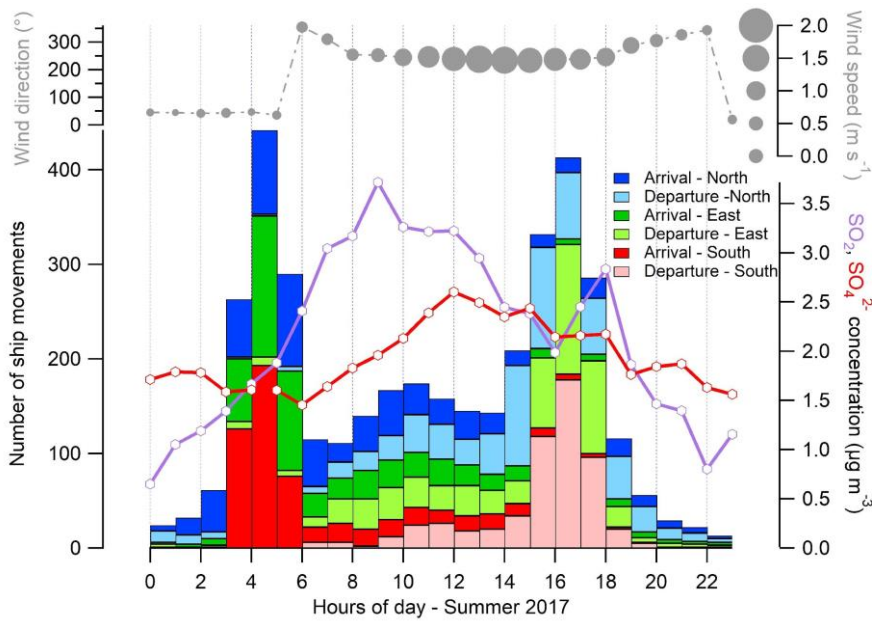
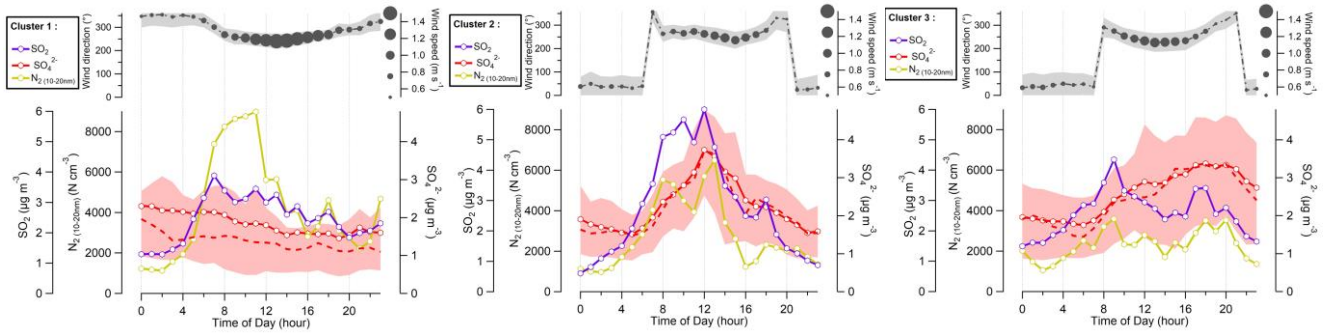


Figure 10: Probability density distributions of BC,  $\text{NO}_3^-$ , f60, f44, wind direction and speed during  $\text{PM}_{2.5}$  exceedance days belonging to local (dark red) and long-range (dark blue) categories.



1480

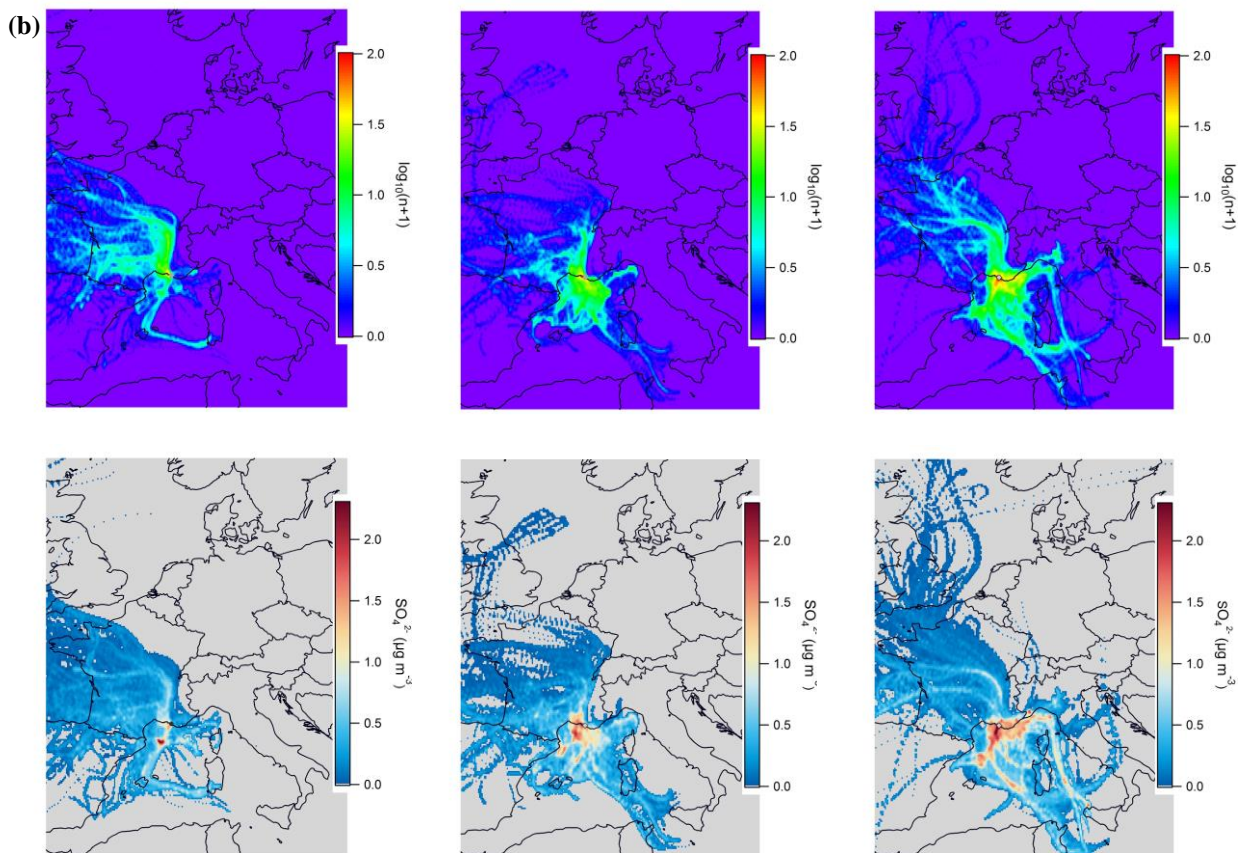
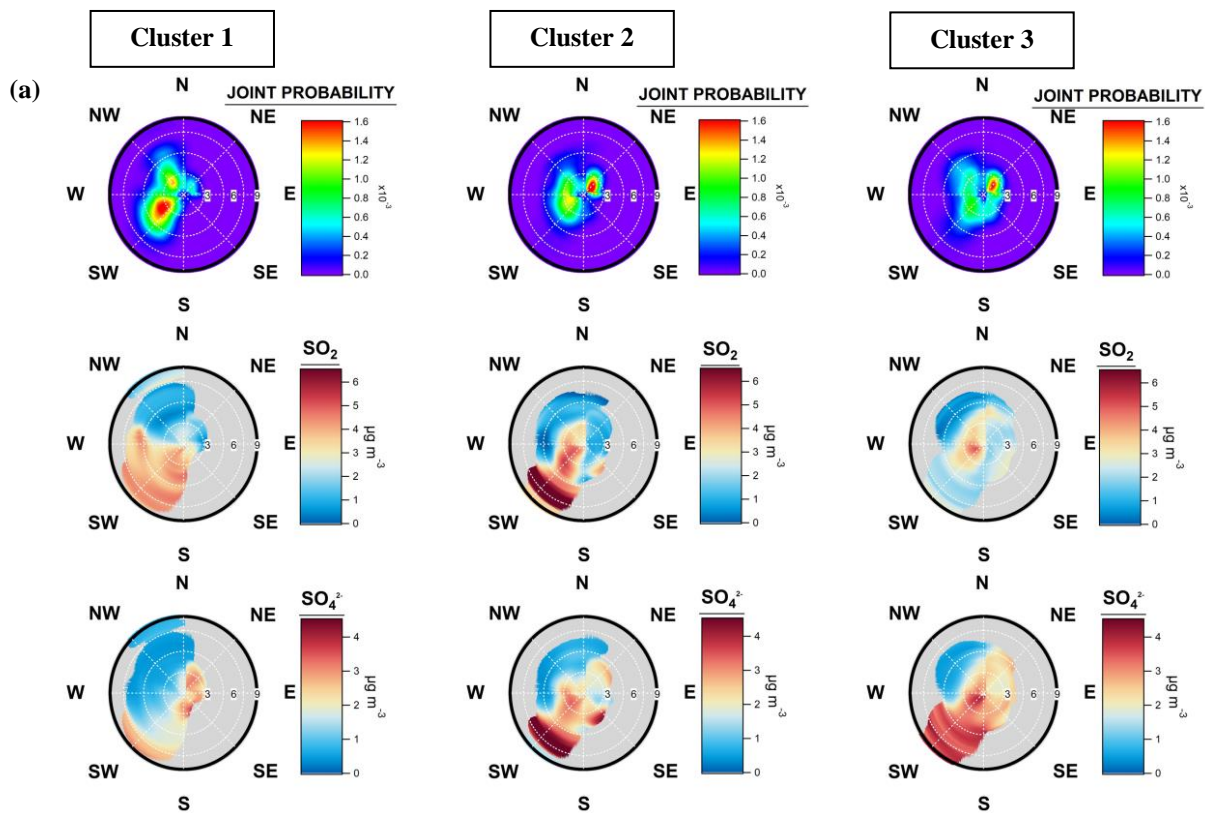
Figure 11: Diurnal profile of cumulative number of ship movements for the summer 2017 period, coloured according to the basin location (blue for north, green for east, red for south) and the type of movement (dark-coloured for arrival, light-coloured for departure). Diurnal profiles of  $\text{SO}_2$  in purple,  $\text{SO}_4^{2-}$  in red and wind direction in grey (the size of dots is proportional to the wind speed intensity) are also represented. The data points linked to low speed conditions ( $<0.5 \text{ m s}^{-1}$ ) were filtered out from the analysis.



1485

Figure 12: Diurnal cycles of  $\text{SO}_4^{2-}$ ,  $\text{SO}_2$ ,  $\text{N}_2 (10-20\text{nm})$  for the three clusters in summer 2017. Solid lines denote mean profiles, red dashed line is the median and red shaded area is the 25<sup>th</sup>-75<sup>th</sup> percentiles range for  $\text{SO}_4^{2-}$ . The average diurnal cycles for wind direction are also shown in the upper panels with the size of dots depending on wind speed and the grey shaded area representing  $\pm$  the standard deviation of wind.

1490



1495 **Figure 13: Joint probability distributions of winds (upper panel) and NWR plots (lower panel) of  $\text{SO}_2$  and  $\text{SO}_4^{2-}$  for the three clusters (a). ZeFir trajectory density for 72h-backtrajectories (generated every hour at MRS-LCP station) and CWT maps for  $\text{SO}_4^{2-}$  (in  $\mu\text{g m}^{-3}$ ) are also displayed for the three clusters (b). The  $\log_{10}(n+1)$  colour scale corresponds to the occurrence of backtrajectory endpoints which drop into a particular cell. A discrete function based on  $\log_{10}(n+1)$  was applied to down-weight data with high concentrations but low number of trajectories passing through a particular cell, as recommended by (Waked et al., 2014). The aim was to avoid local sulfate influence from the transport model.**

1500